ANALYSIS, DESIGN, AND MODELING OF IMAGE-GUIDED ROBOTIC SYSTEMS FOR OTOLOGIC SURGERY

By

Neal P. Dillon

Dissertation

Submitted to the Faculty of the

Graduate School of Vanderbilt University

in partial fullfillment of the requirements

for the degree of

DOCTOR OF PHILOSOPHY

in

Mechanical Engineering

May, 2017

Nashville, Tennessee

Approved:

Robert J. Webster III, Ph.D.

Thomas J. Withrow, Ph.D.

Robert F. Labadie, M.D., Ph.D.

Nabil Simaan, Ph.D.

Michael I. Miga, Ph.D.

To Caitlin and Ronan

Acknowledgments

The work described in this dissertation was a collaborative effort and I certainly could not have completed it on my own. I have been fortunate in my time at Vanderbilt to work with many incredibly talented people who have inspired and challenged me in my research. First, I would like to thank my advisor, Bob Webster, for his support and enthusiasm for research throughout my graduate career. In addition to being an amazing researcher, Bob is a genuine and caring person who is always looking out for the best interests of his students and everyone he works with. His advice and encouragement helped me through the most challenging times of graduate school and I am sincerely grateful for all of his support.

I would also like to thank Tom Withrow. Tom welcomed me to Vanderbilt, got me started with my research, and provided invaluable guidance over the years. He is a gifted teacher and is always eager to spend time helping others to learn new skills, especially in design and fabrication. Much of the knowledge that I needed to design and build the devices described in this dissertation came from Tom.

I am honored to have worked for Robert Labadie in the Computer-Assisted Otologic Surgery (CAOS) lab and to have been a small part of his incredible research program. Rob's passion for research and his excitement for pushing the envelope of medical technology is contagious. He motivates everyone around him and makes working on difficult problems a pleasure. I was lucky to work with so many great people over the years in the CAOS lab, including Louis Kratchman, Ramya Balachandran, Mike Fitzpatrick, Loris Fichera, Jason Mitchell, Michael Siebold, Trevor Bruns, Greg

Blachon, George Wanna, Jack Noble, Patrick Wellborn, Kate VonWahlde, Wendy Lipscomb, Kyle Kesler, and Gigi Zuniga. I am especially grateful for my research collaboration with Loris Fichera. Loris helped immensely with multiple components of this work, was very generous with his time editing this dissertation, and has become a great research partner and friend.

I would also like to thank Nabil Simaan and Michael Miga for serving on my committee. They both provided excellent feedback and helped to greatly improve my work. Finally, I thank all the past and present members of the MEDLab for helping to make graduate school a great experience.

Outside of the lab, I have been supported by my amazing wife, Caitlin, our wonderful son, Ronan, my parents, and the rest of our family. They always put the most stressful times of research into perspective and gave me the encouragement necessary to complete this dissertation.

Abstract

Otology and neurotology are surgical specialties focusing on the treatment of ear diseases. A key component of many otologic and neurotologic surgical procedures is the removal of a portion of the skull behind the ear to gain access to subsurface anatomy. This process, called a mastoidectomy, is performed manually with a high speed surgical drill. Many vital structures, including nerves and blood vessels, are embedded within the temporal bone near the region of bone that must be removed, which makes the procedure difficult, time consuming, and in some cases, overly invasive.

Image-guided and robotic systems have the potential to improve otologic procedures using medical imaging to guide their interventions, enabling patient-specific treatments that reduce invasiveness and save valuable operating room time. However, since damage to the complex vital structures within the surgical field could result in severe consequences to the patient, any image-guided or robotic surgical system must be extremely safe and accurate. These requirements, along with the small surgical workspace and difficulty integrating systems into the current clinical workflow, have limited the adoption of such systems in otologic surgery to date.

This dissertation presents the design, experimentation, and analyses of image-guided, robotic systems under development for otologic surgery in an effort to bring these systems closer to clinical realization. The specific goals of the work are to better understand the technical requirements of various otologic surgical procedures, to improve the safety and efficiency of image-guided and robotic surgery by incorporating system modeling and medical image data into the surgical planning process, and to show feasibility and provide insights into practical issues through experimentation.

Two image-guided otologic procedures are explored in this work: (1) robotic mastoidectomy and (2) minimally invasive cochlear implantation. The technical requirements of robotic mastoidectomy are first explored to determine the necessary robot workspace and the required milling forces. Using these design requirements, a bone-attached robotic system is developed and tested in temporal bone specimens and fresh human cadaver heads. Next, planning algorithms to improve the safety and efficiency of robotic mastoidectomy are described. A method for building patient-specific safety margins around vital anatomy based on probabilistic error models of the robotic system, required safety rates, and simulations of the surgery is provided. A second planning algorithm is presented, which improves robot trajectory generation for milling porous bone in close proximity to vital anatomy by using CT image-based force modeling to optimize tool orientation and velocity.

The focus then shifts to minimally invasive, image-guided cochlear implantation. Two key safety issues are investigated: the positional accuracy of drilling a narrow tunnel towards the cochlea for electrode insertion and the heat rise near vital nerves during drilling. A method for pre-operative, patient-specific risk assessment utilizing the CT scan, modeling of the bone drilling process, and anatomical conditions is presented, followed by an improved surgical drilling approach. Finally, an experimental setup enabling direct temperature measurement of the bone near the facial nerve in cadavers is developed and used to validate the modeling and surgical approach.

Contents

List of Figures

List of Tables

Chapter 1

Introduction

Otology and neurotology are surgical sub-specialties within the field of otolaryngology that focus on the treatment of middle and inner ear diseases. These diseases, and other abnormalities of the ear, affect the hearing and balance systems and often require surgical intervention. Surgery is performed to remove abnormal tissue, treat infection, or implant prostheses in an effort to improve (or mitigate the loss of) hearing and balance function or relieve discomfort. The work in this dissertation focuses on improving otologic and neurotologic surgical approaches through the use of image-guided systems and robotics.

During the normal hearing process, sound waves enter the external ear canal and cause the tympanic membrane (ear drum) to vibrate with the frequency of the waves. This vibration is conducted from the tympanic membrane through a chain of bones called the ossicles (malleus, incus, and stapes). The stapes, which is the last bone in the ossicular chain, pushes against a membranous window of the inner ear (called the oval window), inducing motion of the fluid within the cochlea. The fluid movement stimulates the cochlear nerve, which carries the sensory information to the brain. If there is any disruption to the conduction of sound or conversion to electrical stimulation of the nerve, a person experiences some level of hearing loss. Depending on the specific type and level of hearing loss, surgical intervention may be necessary.

Inner ear diseases can also affect a person's vestibular system, which provides the sense of balance and spatial orientation. Each side of the head contains three semicircular canals that are oriented orthogonally to one another and are filled with fluid. As the head moves, the fluid moves and stimulates the vestibular nerve accordingly. Patients with diseases of the vestibular system experience a feeling of instability, loss of balance, and sometimes nausea. Some vestibular conditions, such as Meniere's disease, may require surgical intervention. Additionally, tumors that grow on the nerves that carry signals from the inner ear to the brain can affect both the hearing and balance systems, and may require surgical removal if the symptoms progress and less invasive therapies are not effective.

1.1 Surgical Overview and Challenges

The anatomy of the middle ear (tympanic membrane, ossicles) and inner ear (cochlea, semicircular canals, vestibule, internal auditory canal) is located several centimeters below the skull surface within the mastoid portion of the temporal bone (see Figure 1.1). As a result, a key component of otologic and neurotologic procedures is the removal of bone to gain access to the underlying anatomy on which the surgeon must operate. This bone removal, called mastoidectomy, is performed by manually milling away the necessary bone using a high-speed surgical drill. Mastoidectomy is a challenging procedure since there are many vital anatomical structures embedded in the temporal bone within the surgical field (see Figure 1.2). These vital structures include the facial nerve, which controls motion of the face, the chorda tympani nerve, which

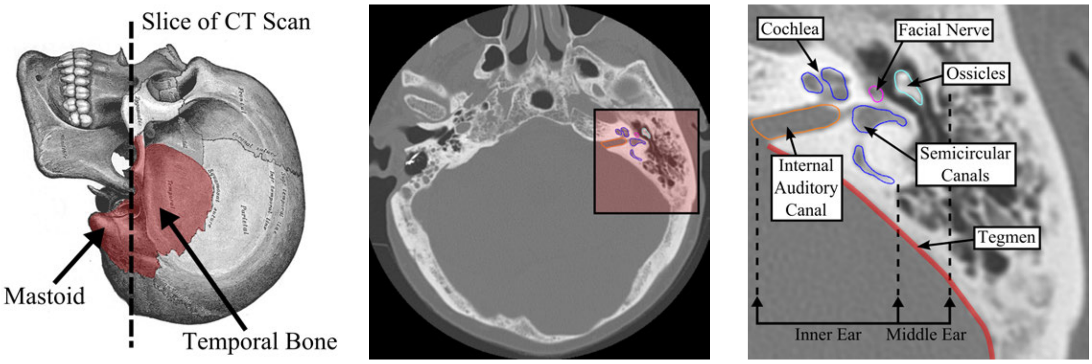

(a) (b) (c)

Figure 1.1: (a) Skull with temporal bone, mastoid, and computed tomography (CT) slice shown in parts b and c labeled, (b) axial view of a patient CT scan showing the area of the skull relevant to otologic surgery, and (c) mastoid region of temporal bone with several vital anatomic structures of the middle and inner ear labeled.

carries taste signals to the brain, large blood vessels such as the carotid artery and intra-cranial continuation of the jugular vein, and the tegmen, which is the boundary between the mastoid and the brain (see Figures 1.1 and 1.2). Because injury to these vital structures can lead to morbidity or other severe complications, surgeons manually identify these structures using visual, tactile, and auditory feedback and then remove bone as needed around them [14]. Consequently, the surgery can be difficult and time consuming, can result in wider dissection than is necessary for the surgery, and requires years of specialized training.

Approximately 120,000 mastoidectomies are performed each year in the United States [49] (extrapolating to the present time and accounting for both in- and outpatient procedures). Mastoidectomy is performed to treat various infections and diseases (e.g. cholesteatoma, mastoiditis) and is also a component of more complex

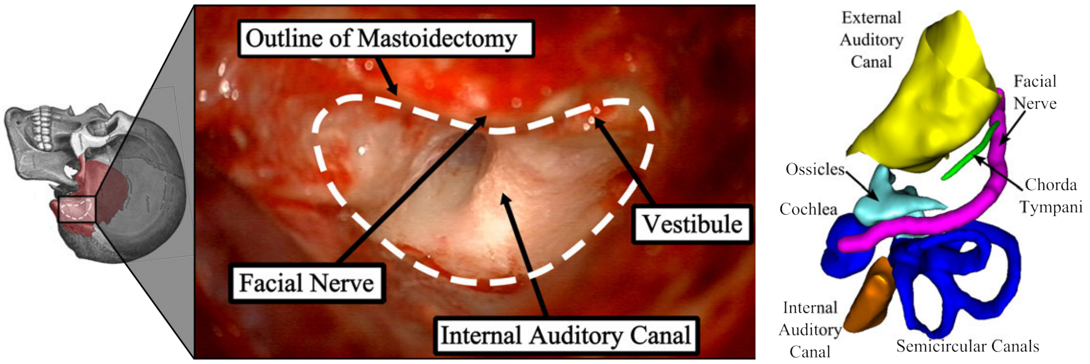

(a) **(b)**

Figure 1.2: (a) Photograph of mastoidectomy from surgery at Vanderbilt University Medical Center with labels indicating location of several anatomical structures. (b) 3D rendering of anatomical structures in the temporal bone.

surgical procedures. Two examples of otologic procedures that require a mastoidectomy are cochlear implantation and the translabyrinthine approach for vestibular schwannoma. These procedures, which are described in detail below, present unique challenges that can be addressed through the use of image-guidance and robotics.

1.1.1 Cochlear Implantation

Cochlear Implantation (CI) is the current state of the art for restoring the sense of sound to individuals with severe to profound sensorineural hearing loss (i.e. hearing loss caused by damage to the cochlea or nerve pathways to the brain). The implanted component of the CI system is an electrode array that is inserted into the cochlea to directly stimulate the auditory nerve (see Figure 1.3). Sound is picked up from the environment by an external microphone, filtered, processed, and then converted to electrical signals which are sent to the electrode array. During normally functioning

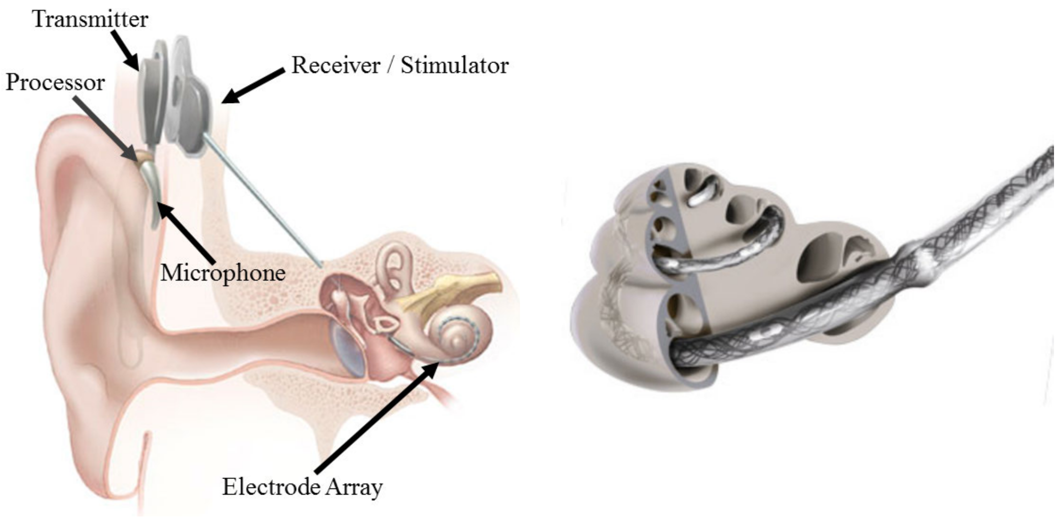

(a) **(b)**

Figure 1.3: (a) Cochlear implant system (image source: www.nih.gov) and (b) rendering of electrode array inside cochlea (image source: www.medel.com).

hearing, different regions of the cochlear nerve are stimulated according to sound frequency (high frequencies toward the base and low frequencies toward the apex). Similarly, individual electrodes within the array correspond to different frequency ranges and are positioned within the cochlea near the nerve associated with that range.

As of December 2012, approximately 324,200 devices have been implanted worldwide [97], including nearly 100,000 devices in the United States, and this number is expected to continue to grow. According to MED-EL (Innsbruck, Austria), one of the pioneering CI manufacturers and the second largest producer of CIs in the world, approximately 50,000 cochlear implants were sold in 2013. Around 30,000 of these implants were received by children in 2013; furthermore, it is estimated that 130,000 or more children are born each year with hearing loss that could be treated with a

CI [55]. Additionally, the World Health Organization predicts that hearing loss will be among the 10 most burdensome diseases worldwide by 2030 (projected to rank 9th in terms of causes of "disability-adjusted life years") [89].

During conventional CI surgery, the surgeon performs a mastoidectomy to gain access to the cochlea for electrode insertion. Accessing the cochlea through the facial recess, the region of the middle ear cavity bounded by the facial nerve and chorda tympani, enables insertion of the electrode array along a vector tangential to the basal turn of scala tympani. Insertion of the electrode array such that it is fully within the scala tympani is desired since it yields better audiological outcomes [5,48]. After the facial recess is reached, an opening into the cochlea is made either through the round window (natural opening from middle ear to inner ear sealed by a membrane) or by making a cochleostomy (a small opening into the cochlea). The electrode array is then carefully inserted into the cochlea and connected to the subcutaneous electronics prior to closing the incision and finishing the surgery.

1.1.2 Vestibular Schwannoma

Vestibular schwannomas (VS), also known as acoustic neuromas, are benign tumors of the vestibular nerve located in the internal auditory canal (IAC) and extending into the brain (see Figure 1.4). VS can cause partial or complete unilateral hearing loss, dizziness and loss of balance, facial weakness, tinnitus, and headaches, among other symptoms. In recent years, the incidence of VS has increased due to general medical awareness of the disease and improved imaging and screening protocols [40,

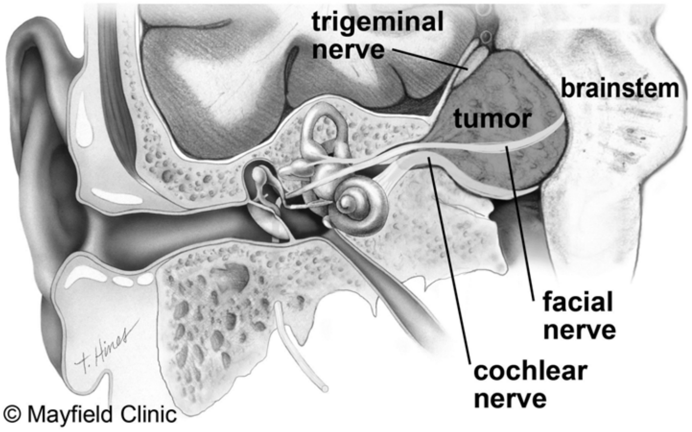

Figure 1.4: (a) Vestibular schwannoma growing within the internal auditory canal (image source: www.mayfieldclinic.com)

115]. Management of VS consists of three modalities: observation, radiotherapy, and surgery. Due to the benign and slow growing nature of VS, there is a trend in the United States and worldwide toward less invasive treatment [17]. However, many patients require some form of surgical intervention, especially in cases where the tumor is large, radiotherapy is not effective, or the tumor is causing substantial discomfort for the patient. The translabyrinthine approach is a common procedure for VS removal and is generally preferred (compared to other approaches such as the retrosigmoid and middle fossa) in cases when the the tumor is large, it extends towards the brain stem, or the patient has little remaining hearing [14].

Extensive bone removal is required in order to reach the IAC for tumor removal using the translabyrinthine approach (Figure 1.5), which was originally described in 1904 by Panse but not popularized until the 1960s [56]. The mastoid and the labyrinth are milled away and the bone covering the IAC and posterior fossa (region of cranial cavity containing the brain stem and cerebellum) is thinned to the thickness of an egg

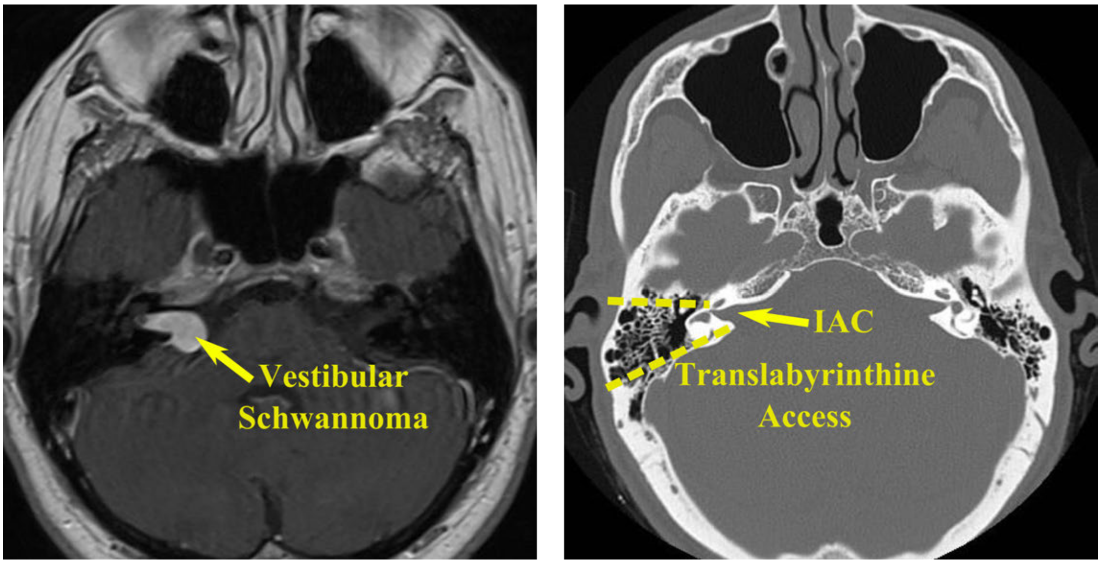

Figure 1.5: MRI showing vestibular schwannoma in the internal auditory canal (left) and extending into the cerebellopontine angle. Tumors of this size are typically removed using the translabyrinthine surgical approach, which requires extensive bone removal in the mastoid and labyrinth to access the internal auditory canal, as shown in the CT scan on the right. Note that these two scans are from different patients.

shell, allowing this small amount of remaining bone to be carefully removed manually to access the IAC [14]. Following the opening of the IAC, the tumor is carefully separated from the nerves and removed. Obliterating the mastoid and labyrinth using a hand-held drill can take several hours because vital anatomy (e.g. the facial nerve) is embedded within the bone and must be identified and avoided.

1.1.3 Technical Challenges and Motivation for Computer-Assisted Surgery

Given the current state of the art in CI and translabyrinthine VS surgery, as described above, it is hypothesized that these procedures can be improved through the use of image-guidance and/or robotic assistance. This improvement could come in many forms, including decreased invasiveness, shorter operating time, or reduced complications. In CI surgery, the mastoidectomy is performed solely to provide the surgeon access to the cochlea for electrode array insertion. However, the size of the cochlea and electrode array is small enough that the insertion could be completed with a narrow tunnel instead of the comparatively large mastoidectomy. Currently the level of invasiveness is necessary since surgeons must manually mill away bone to identify vital anatomy between the external skull surface and the cochlea. If the procedure is made less invasive through the use of an image-guided system, operating time and costs could potentially be decreased. Furthermore, less specialized surgeons could perform the surgery, enabling additional CI candidates to receive the implant, which may help to bridge the gap between the number of individuals who could benefit from a CI and those who actually receive one.

In translabyrinthine VS surgery, the bulk removal of bone required for access to the IAC is very time consuming and challenging. If this portion of the procedure was automated based on plans made in the pre-operative image, the surgeon could be preserved for the crucial work of opening the IAC and resecting the tumor. This could potentially reduce the amount of bone that must be removed as well as the operating time and costs associated with the surgery.

Despite the potential benefits outlined above, otology and neurotology have lagged behind other surgical fields such as orthopedics and neurosurgery in the incorporation of image-guidance systems and robotics into the operating room (OR) to date. This is likely due to the high accuracy requirements necessitated by the presence

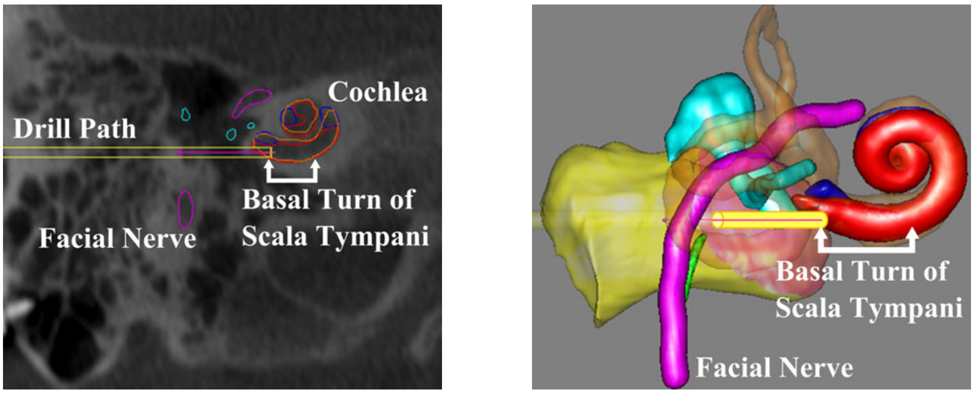

(a) (b)

Figure 1.6: (a) CT scan showing segmented temporal bone anatomy and safe drill path from skull surface to cochlea, and (b) 3D rendering of anatomy and path. Images acquired using custom software developed at Vanderbilt [93, 95]

of complex and delicate anatomy in close proximity to the surgical work space and the potential for severe consequences if errors are made. Thus, more work must be done to increase the safety of image-guided, robotic systems for otologic and neurotologic surgery, determine the feasibility in more clinically-realistic scenarios, and identify and demonstrate benefits over the current standard of care. This need for additional work is the motivation for the analyses and experimentation presented in this dissertation.

1.2 Image-Guided and Robotic Surgical Systems

1.2.1 Minimally Invasive Cochlear Implantation

The development of less invasive surgical approaches for CI surgery (i.e. passing the electrode array through a narrow tunnel instead of performing a mastoidectomy) has been a focus of several research groups for over a decade. One such approach, which has been performed on hundreds of patients, is called the "suprameatal approach" and was initially proposed by Kronenberg et al. [71, 72] to provide access to the middle ear through a narrow hole. The hole is drilled blindly from the external surface of the mastoid to the attic (superior region of the middle ear cavity). The electrode array is then passed through this hole and into the cochlea after making a cochleostomy by lifting the tympanomeatal flap (incision through the external canal). Another approach, described by Hausler et al. enables insertion of the electrode array through the external canal [52], therefore obviating the need for mastoidectomy. The advantage of these techniques is that the access to the middle ear can safely be performed manually, without image guidance. However, a major disadvantage is the non-optimal implant insertion vector into the cochlea as a result of the access to the middle ear through the attic or external canal. To obtain an optimal insertion vector, i.e. tangential to the basal turn of the scala tympani, the electrode array must be inserted through the facial recess, passing between the facial nerve and chorda tympani (see Figure 1.6). This requires the removal of bone in close proximity to the facial nerve and chorda tympani, which cannot be reliably done manually in a minimally invasive manner since the structures are not easily visible without performing a mastoidectomy (see Figure 1.7). Therefore, image-guidance is necessary to accurately align the surgical drill with a safe path through the mastoid and into the middle ear at the facial recess without contacting vital anatomy.

The research group led by Robert Labadie at Vanderbilt University has been investigating minimally invasive cochlear implantation surgery to enable electrode

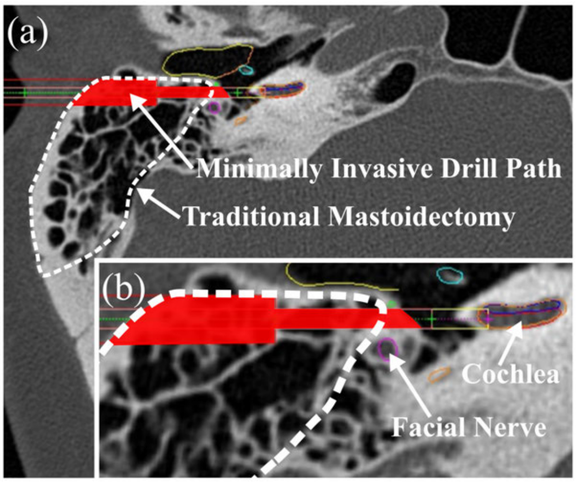

Figure 1.7: (a) Slice of CT scan showing amount of bone to be removed in traditional (dotted white outline) vs. minimally invasive cochlear implantation surgery (shaded drill path). (b) Close-up of minimally invasive drill trajectory and surrounding anatomical structures.

insertion through the facial recess for over a decade. The first attempt at this approach used a custom-designed rigid frame that was fixed to a dental bite block for registration of a CT scan to the patient in the operating room [77, 81]. An optical tracking system was then used to guide the surgeon holding a surgical drill along a pre-operative plan for creating a minimally invasive tunnel to the facial recess [76].

A simpler approach using bone-mounted drill guides, which reduced some of the practical implementation errors (e.g. manually aligning the drill with the tracking system, potential for movement of the tracking frame with respect to the patient) of the prior approach was then developed [80, 126]. This approach utilized existing clinically approved technology for image-guided stereotactic neurosurgery, in which patient-specific frames are 3D printed based on the patient anatomy and positions of bone-implanted fiducial markers (StarFix^{TM} MicroTargeting Platform, FHC Inc.,

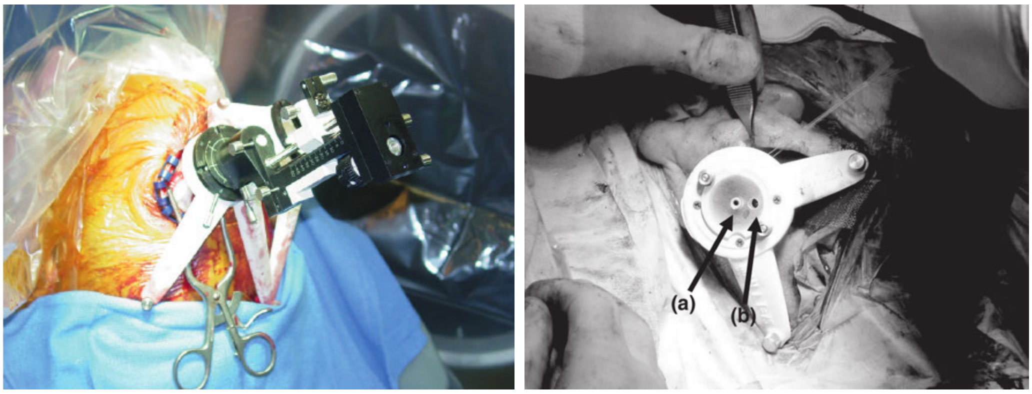

(a) (b)

Figure 1.8: (a) Commercially available patient-customized stereotactic positioning platform (StarFix$^{\text{TM}}$) for image-guided neurosurgery manufactured by FHC Inc. (image from [61]), and (b) clinical accuracy validation experiment of minimally invasive cochlear implantation surgery using StarFix platform (image from [80]).

Bowdoin, ME, U.S.A.) (see Figure 1.8). These stereotactic platforms were adapted for otologic surgery and manufactured to align a surgical drill along the desired path from the skull surface to the cochlea. Using this approach, bone-implanted markers are inserted into the patient and a CT scan is acquired at a pre-operative visit. The platform is then manufactured and shipped to the hospital between this visit and the day of surgery. The positional accuracy of the frames was validated clinically by placing probes in place of where the drill would be located and checking the alignment of the probe with the target position after a conventional mastoidectomy was performed [80].

This minimally invasive surgical approach was further refined by the development of a rapid-production micro-stereotactic table (Microtable$^{\text{TM}}$) that is manufactured using a CNC machine in approximately five minutes and mounted to the patient via bone-implanted anchors [79]. A flow chart of the workflow is shown in Figure 1.9. Using this workflow, the anchors, which also serve as fiducial markers, can be implanted in the OR and the scan acquired intra-operatively. Compared to the approach using 3D printed stereotactic frames, this eliminates the need for an additional pre-operative visit and for the patient to go home for several days with the bone anchors in place. The Microtable is then manufactured based on the location of the fiducial markers and desired drill trajectory (see Figure 1.10). The position and relative height of the three legs, which lock to the spherical fiducial markers, can be specified to achieve a trajectory of any position and orientation (Figure 1.10b). The drill and guide are then mounted to the Microtable and the surgeon advances the drill along the constrained path into the temporal bone towards the cochlea. The pre-operative planning for this procedure is aided by recent developments in image processing. Automatic segmentation of vital anatomy within the temporal bone [93, 95] facilitates the determination of safe linear paths to the cochlea, which can be specified manually by the surgeon or generated automatically [94] (see Figure 1.6).

The positioning accuracy of the Microtable was assessed clinically during traditional CI surgeries [74] and the approach was further validated by performing the full procedure on cadaver temporal bones [7]. Later, the first clinical implementation using the full surgical protocol, including drilling the path from the skull surface to the cochlea, was then performed [75]. Figure 1.11 shows the placement of fiducial markers and the Microtable mounted to a patient in the operating room. The surgery was performed on nine patients at Vanderbilt University Medical Center. The CI electrode was successfully inserted on eight of the nine patients using the minimally

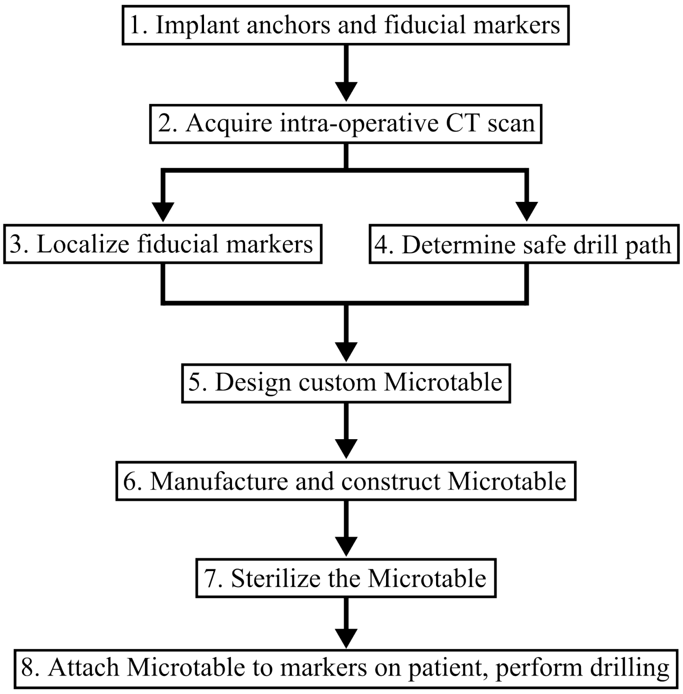

Figure 1.9: Flow chart outlining steps in clinical implementation of Microtable system. (adapted from [79]).

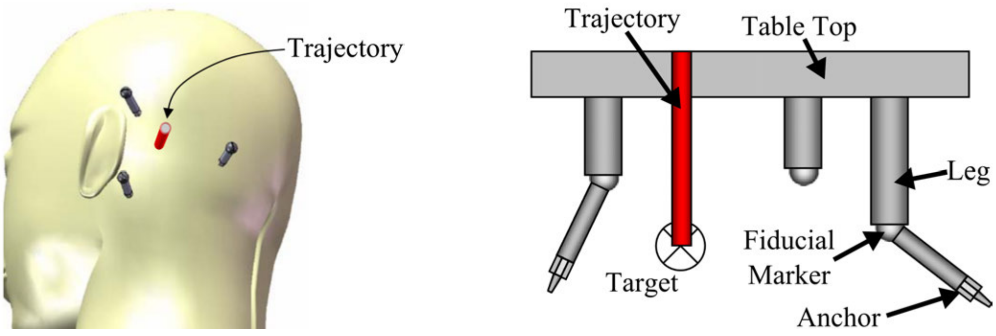

(a)

(b)

Figure 1.10: (a) Planned trajectory to cochlea on patient skull, and (b) schematic of Microtable mounting to spherical tips of extenders that are fastened to the bone anchor screws; the position and lengths of the legs are selected based on these locations and the target trajectory (images adapted from [79]).

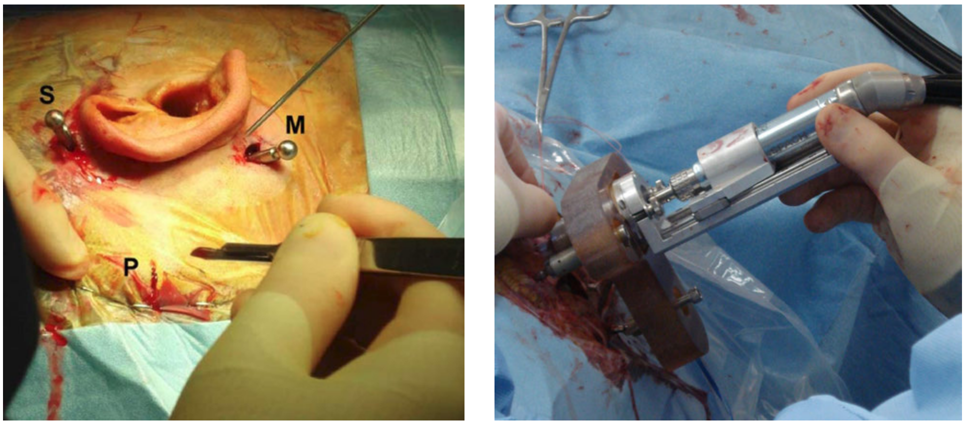

(a) **(b)**

Figure 1.11: (a) Bone anchors and fiducial markers being placed on patient during clinical implementation of minimally invasive CI. The markers are labeled according to their position ("M", "P", and "S" stand for "Mastoid", "Posterior", and "Superior"). (b) Microtable fixed to the patient to align the surgical drill. The surgeon slides the drill into the skull along the planned path (images from [75]).

invasive approach; a mastoidectomy was needed for the other patient after difficulty threading the electrode through the narrow channel. The most significant complication occurred with one patient who experienced immediate postoperative facial nerve weakness (patient recovered to a II/VI on the House-Brackman scale [57] after 12 months). Exploratory surgery performed the next day to examine the cause of the weakness revealed no structural damage to the facial nerve, suggesting that excessive heat generated while drilling was the likely cause of injury. Thus, more work must be done to better understand heat-related and other risks associated with this surgical approach before it can be translated to widespread clinical use.

In addition to the research described above, two robotic methods for image-guided CI surgery have also been investigated by the research group at Vanderbilt. These

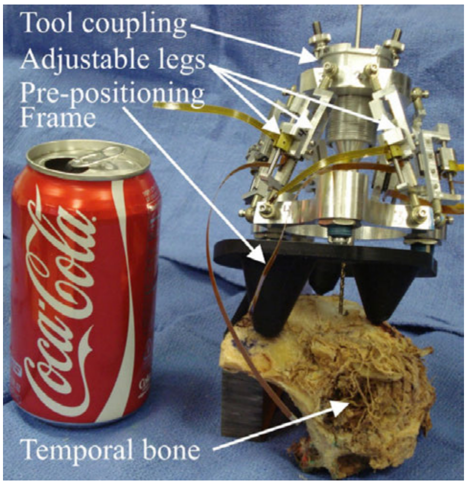

Figure 1.12: Bone-attached robot for minimally invasive CI surgery (image from [70]).

systems overcome one of the limitations of the Microtable approach - the need for a CNC machine and operator at the hospital - by providing a method to guide the drill without patient-specific hardware. First, an image-guided system for minimally invasive CI using an industrial robot was developed and tested on a phantom [9]. The robot end-effector held the surgical drill and was guided to the desired path using an optical tracking system. Additionally, a bone-attached robot for minimally invasive CI surgery was developed [70] (see Figure 1.12). Using the robot, a surgical workflow similar to the Microtable approach is followed. Rather than manufacturing a custom stereotactic frame, the robot is positioned to the prescribed pose. Then, the joints are locked, the robot is powered off and mounted to the patient's skull to guide the drill. Effectively, the robot is an adjustable version of the Microtable, eliminating the need for a CNC machine and operator in the hospital.

Concurrent to much of the work by Labadie et al., the research group led by Stefan Weber at the University of Bern have developed a custom robotic system for

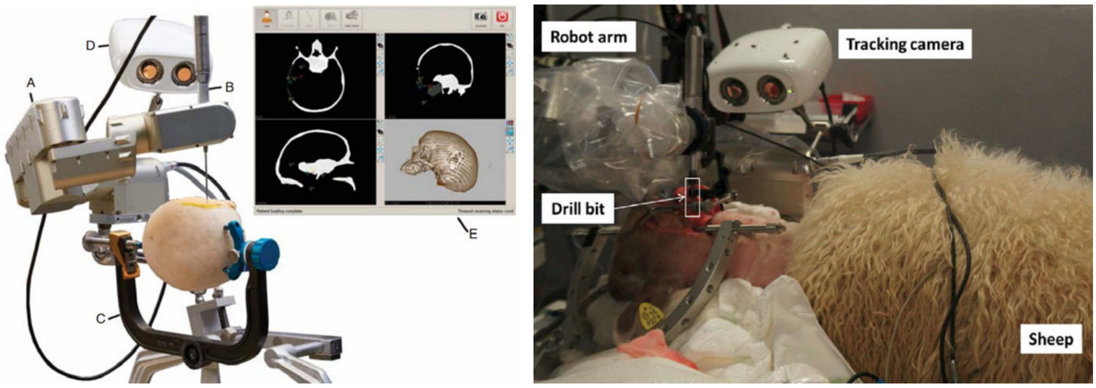

(a) (b)

Figure 1.13: (a) Custom image-guided robot for minimally invasive CI surgery developed at the University of Bern (image from [12]). (b) Robot during animal trial with sheep for the purposes of evaluating the temperature during the drilling process (image from [44]).

drilling a narrow path to the cochlea through the facial recess (Figure 1.13a) [12]. The robot mounts to the side of the OR table and is aligned with the patient via bone-implanted fiducial markers that are localized by the robot end-effector and highly accurate optical tracking system. Using the tracking system, the tool position is monitored and verified throughout the procedure, and the motion of the robot is adjusted as necessary. They have demonstrated clinically sufficient accuracy with their robotic system during in vitro testing (0.15 ± 0.08 mm error) [11] and are moving towards clinical use.

More recently, they have investigated several functional safety measures, in addition to verification using intra-operative CT scans, to accurately localize the position of the drill during surgery and minimize the risk of damage to vital anatomy. These safety measures include: (1) redundant tool pose estimation using a correlation between CT-image density and real-time drilling force measurements [127], (2) neuromonitoring of the facial nerve throughout drilling using a custom probe inserted into the minimally invasive tunnel [3], and (3) thermal modeling of the drilling process based on pre-operative CT data [44]. Their work estimating the temperature at the facial nerve during this surgical approach (see Figure 1.13b) indicated that the nerve can reach potentially dangerous temperatures if adequate safeguards (optimized drilling parameters, irrigation, etc.) are not employed, which corroborated a concern from prior clinical trials with the Microtable system at Vanderbilt [75].

Finally, Kobler et al. have also developed a minimally invasive CI system. Their device is a bone-mounted, passive parallel mechanism, which is manually adjusted to align the drill with the desired trajectory based on a pre-operatively planned path [65] (see Figure 1.14). To improve the accuracy of their system, they have developed an error model used for optimization of the robot configuration [66] based on prior analyses of the surgical procedure, including fiducial localization accuracy [64], accuracy of different drilling strategies [68], mechanical characterization of the bone anchors used for robot attachment [67], and evaluation of loads on the robot during surgery [69]. They have successfully tested the system on custom phantom temporal bones.

Open Research Questions

The minimally invasive CI surgical approach for insertion through the facial recess has matured significantly throughout the past decade but significant challenges remain before the approach can be translated to widespread clinical use. The primary challenges and open research questions involve ensuring the preservation of facial

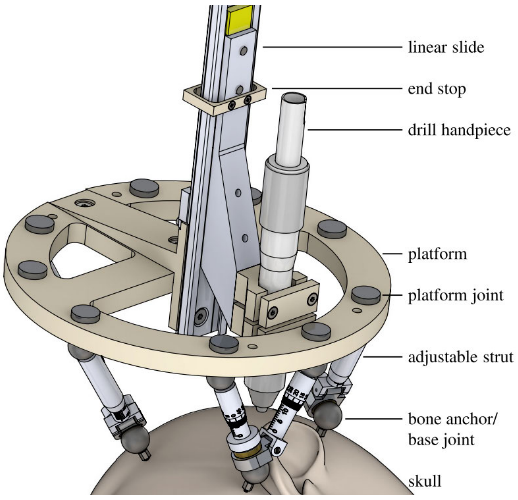

Figure 1.14: Rendering of bone-mounted, passive, parallel robot for minimally invasive CI surgery developed at the University of Hannover (image from [66]).

nerve function while drilling the narrow tunnel from the skull surface to the middle ear. Accurate image guidance and specialized hardware minimize the risk of directly contacting the vital anatomy with the drill. However, nerve injury can occur via thermal damage secondary to heat generated by the bit cutting through nearby bone and/or from friction between the drill bit and the surrounding bone or bushing sleeve, as shown in [75] and [44]. This heat generation, and how it can be reduced during surgery, needs to be better understood before the minimally invasive approach can be safely and reliably executed. General drilling fundamentals as well as patient-specific anatomy must be considered to determine safe drilling methodologies and ensure that the patient is not being exposed to excessive risk. Specifically for the Microtable approach developed by Labadie et al., which relies on the surgeon to manually advance the drill into the bone, the drilling parameters that can be effectively controlled must be standardized to improve the consistency of the clinical outcomes. Furthermore, patient-specific factors that affect positional accuracy of the drilling process must be examined. As stated above, the risk of the drill deviating off path enough to directly contact the nerve (approximately 5 mm) is low but slight deviations could cause substantial changes to the amount of heat conducted from the drill to the nerve. If these two key safety factors are better understood and appropriately accounted for in the approach, minimally invasive CI surgery will be made safer and will be much more likely to be adopted by clinicians.

1.2.2 Robotic Mastoidectomy

Robot-assisted temporal bone milling for a variety of skull base procedures has also been an active area of research in recent years. Federspil et al. were the first to develop a robot for guiding a surgical drill in otologic surgery. They used an industrial robot to autonomously mill a pocket for a CI receiver [41] (see Figure 1.15). They also investigated different milling control strategies, including velocity and force-based control schemes and different milling path parameters (depth of cuts, horizontal vs. vertical milling paths, etc.).

Robotic mastoidectomy was then proposed and tested by several research groups. This represents a significantly more challenging problem than drilling a pocket for a CI receiver because the tool must come much closer to vital anatomy (e.g. the facial nerve) and the milling cavities are unique for each patient based on their specific anatomy. Danilchenko et al. performed the first robotic mastoidectomy in the laboratory on cadaveric temporal bones using an image-guided industrial robot [23] (see


(a) **(b)**

Figure 1.15: (a) Force-controlled milling robot for otoneurosurgery developed by Federspil et al. and (b) cochlear implant receiver in cavity milled by robot (images from [41]).

Figure 1.16). To align the robot with the patient anatomy, bone-implanted fiducial markers were inserted prior to acquiring a CT scan. The markers were then localized in physical space using an optically tracked probe and both the specimen and the robot were tracked throughout the procedure so the target anatomy could be represented relative to the robot's coordinate system.

Another approach for robotic bone milling for mastoidectomy and other skull base surgeries, as described in [83], [129], and [96], uses a cooperatively controlled approach. Instead of the robot performing the milling autonomously, the surgeon and robot both hold the milling tool and the robot enforces virtual fixtures (i.e. "no fly zones") around vital anatomy such as the facial nerve and the IAC. The surgeon is allowed to move freely whenever the drill is in a safe position but the robot prevents any motion that would cause the tool to collide with vital anatomy.

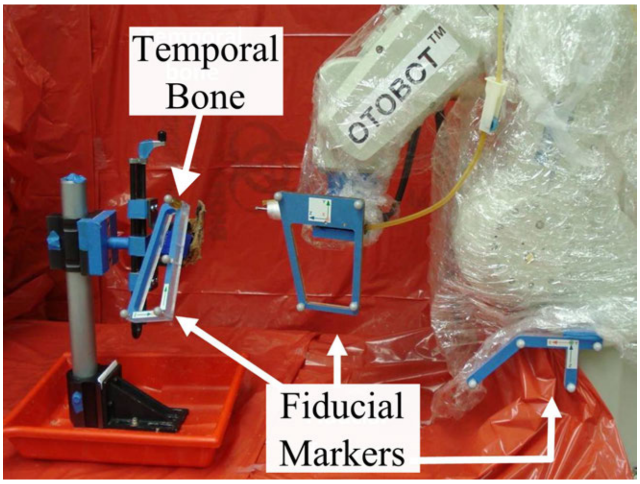

Figure 1.16: Image-guided industrial robot performing robotic mastoidectomy in cadaver (image adapted from [23]).

Open Research Questions

To date, most systems proposed for robotic mastoidectomy and other skull base bone milling surgeries have used large, free standing, industrial-like robots. These systems take up significant space in the operating room, provide workspaces much larger than required for otologic and neurotologic surgery, and require external tracking systems to monitor the position of the robot and ensure alignment with the patient throughout surgery. A compact bone-mounted robot similar to the one developed for minimally invasive CI surgery [70] would enable a much simpler clinical workflow and could potentially improve the accuracy of the system by eliminating the reliance on an external tracking system. However, before such a system could be designed, a better understanding of the requirements of the surgery is needed. Specifically, since bone-mounted robots are necessarily small, they are limited in workspace size and power. Thus, the forces required for surgery and the workspace size necessary to cover a range of mastoidectomy sizes must be evaluated. Additionally, the feasibility of attaching the robot to the skull and safely performing the bone milling using a bone-attached robot must be assessed through cadaver experimentation.

Other factors limiting the translation of robotic surgery to otology and neurotology include ensuring the safety and efficiency (i.e. the time of surgery) of the procedure despite significant patient variation. These factors can be addressed through the use of system modeling and patient-specific planning based on pre-operative imaging. Instead of relying on surgeon judgment to determine how close the robot should come to vital anatomy and how fast the robot should move during the procedure, segmentations of anatomy and models that predict system error and cutting forces throughout procedure can be used to plan the milling cavity and trajectory. Advanced planning methods have the potential to provide more accurate assurances of safety and can enable more efficient removal of the necessary bone, both of which will make the robotic approach more clinically viable.

1.2.3 Surgical Robotics Research in Other Specialties

Much of the image-guided and surgical robotics research in otologic surgery described above was inspired by prior work in other surgical fields. Surgical robotics research began several decades ago and has grown rapidly in recent years. Several robotic systems have been successfully commercialized and are becoming the standard of care for some procedures, most notably the da Vinci Surgical System (Intuitive Surgical, Sunnyvale, CA, USA) for laparoscopic surgery. These image-guided robots have been shown to be beneficial for a variety of procedures due to their high accuracy and repeatability, ability to access and work in small and confined spaces, and capacity to integrate various imaging and sensing modalities into the execution of the surgical task. Computer-assisted or robotic systems add value to a surgical intervention in a variety of ways and function under different paradigms, such as performing tasks autonomously based on a prescribed plan, operating tele-operatively to enhance surgeon dexterity or reduce the invasiveness of a procedure, or cooperatively controlling surgical instruments with the surgeon.

A subset of medical robots, called surgical CAD/CAM (Computer-Assisted Design and Computer-Assisted Manufacturing) systems, help to execute a plan based on pre-operative imaging and modeling in a manner analogous to computer-integrated manufacturing [119], i.e. using computers to plan, control, and integrate all steps of a manufacturing process. Examples of early research in this area include robot-assisted stereotactic neurosurgery [73] and orthopedic bone milling for knee and hip arthroplasty [54, 58, 60, 62, 99, 118]. More recently, several image-guided robotic systems for orthopedic bone milling have received regulatory approval and are being used clinically, including the RIO System (MAKO Surgical Corp., Ft. Lauderdale, FL, USA, subsequently acquired by Stryker Corp.), the ROBODOC Surgical System (Curexo Technology Corp., Fremont, CA, USA, formerly Integrated Surgical Systems, Inc.), the Acrobot Sculptor (Acrobot Company Ltd., London, UK, subsequently acquired by MAKO Surgical) and the CASPAR system (URS Ortho GMBH & Co. KG, Rastatt, Germany). The RIO System is shown in Figure 1.17.

The rigidity of bone and the fact that bone is easily discernible in CT images

Figure 1.17: RIO Robotic Arm Interactive System for orthopedic surgery (makosurgical.com).

enables planning of the surgical task in the pre-operative image with minimal risk of tissue deformation during surgery. Robot-assisted orthopedic bone milling provides a more accurate cavity in which to insert the implant [99], improving implant fixation. Moreover, the accuracy of the robotic system enables better alignment of the prosthetic components compared to the manual approach, resulting in improved post-operative performance of the joint [20].

Another procedure for which an image-guided robotic system has been developed to guide a surgical drill is pedicle screw placement for spinal surgery. Screws must be placed in several vertebrae to hold a connecting rod between them to immobilize a section of the spine, enabling consecutive vertebrae to fuse together. The proximity of the spinal cord to the required screw location makes the procedure challenging without opening a wide surgical site. A bone-attached robot was developed for aligning a drill guide for precise placement of the pedicle screws in a less invasive approach [28, 109].

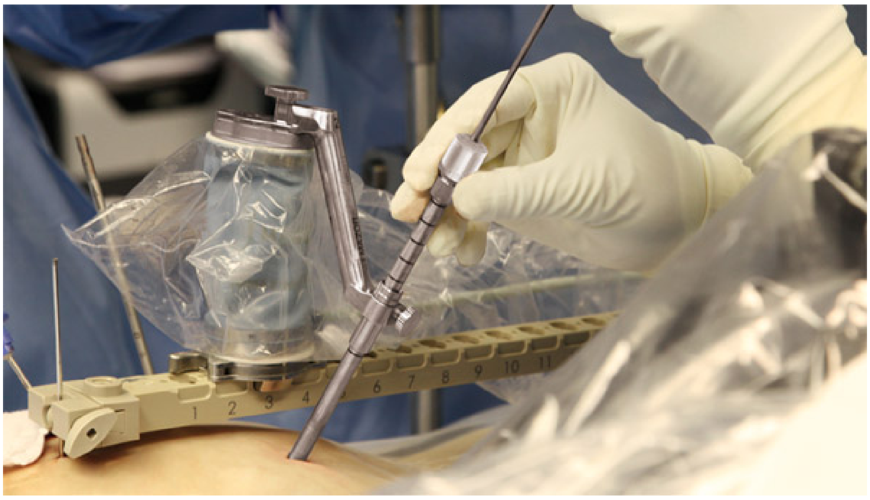

Figure 1.18: Mazor Renaissance robot for minimally invasive pedicle screw placement (mazorrobotics.com).

This system has been successfully commercialized (Renaissance Guidance System by Mazor Robotics Ltd., Caesarea, Israel) and is currently used clinically (see Figure 1.18).

Given the technical similarities between bone milling and drilling in different areas of the human body, a logical extension of this work would be to use similar systems for otologic and neurotologic surgery. However, as described in the preceding section, the unique challenges of these surgical specialties make translating prior research difficult and necessitates focused research in the area of image-guided, robotic otologic and neurotologic surgery.

1.3 Dissertation Overview and Contributions

The purpose of the work described in this dissertation is to analyze, model, and design image-guided and robotic systems for otologic surgery in an effort to address many of the open research questions explained in the prior section and bring these systems closer to clinical translation. The work focuses on improving two procedures within the field of otologic surgery: mastoidectomy (with an emphasis on the translabyrinthine approach to VS removal) and cochlear implantation. The specific goals of the work are to better understand the technical requirements of the procedures, improve the safety and efficiency of robotic surgery by incorporating modeling into the surgical planning phase, and experimentally validate these systems to show feasibility and provide practical insights. An overview of the components of the dissertation and the associated contributions are described below.

1.3.1 Development and testing of the first bone-attached robot for mastoidectomy

The first component of the work involves the development of a custom robot for mastoidectomy. Experimentation and analyses are performed to better understand the technical requirements of mastoidectomy. First, workspace analyses for both standard mastoidectomies and labyrinthectomies are performed to inform the kinematic design of a robot (see Chapter 2.1, [31]). The Cartesian and orientation workspace requirements are provided. These analyses can be used in the design and planning of robotic systems for otologic and neurotologic surgery. A series of experiments are then performed to measure the forces at the cutting burr during robotic milling of temporal bones to determine the range of forces the robot must be designed for and to analyze preferred path planning strategies (see Chapter 2.2, [35]). Prior work has provided force measurements while milling bone under limited ranges of parameters; however, a comprehensive investigation of forces for different burr types, cutting angles, depths, velocities, and bone types was not previously completed and is presented herein.

Next, the clinical workflow for mastoidectomy with a bone-attached robot is presented, followed by the design of two custom robot prototypes. Experiments were performed in cadaveric temporal bone specimens to show the feasibility of the robotic approach (see Chapter 3, [30, 31]). These experiments represent the first-ever use of a bone-attached robot for mastoidectomy. Additional experiments in fresh human cadaver heads were performed to evaluate the system in a more clinically realistic manner, estimate the time required for the robotic approach, and target deeper cavities for the translabyrinthine approach to vestibular schwannoma (see Chapter 3, [33]). In all experiments, vital anatomy within the temporal bone was preserved and the results from the full cadaver head trials indicate that the robotic approach may save time over the manual approach for translabyrinthine access to the IAC.

1.3.2 Patient-specific planning algorithms for improved safety and efficiency during robotic mastoidectomy

The next phase of work in this dissertation focuses on improved planning for robotic mastoidectomy. An algorithm is presented to generate patient-specific safety margins around vital anatomic structures according to surgeon-specified safety levels for the structure (see Chapter 4, [38]). These variable, non-uniform safety margins replace simple, uniform-thickness margins by using stochastic models of the different error sources present in an image-guided robotic system. This work builds upon prior work that used only registration error estimates by incorporating image distortion, robot kinematic, and deflection errors. The framework can be extended to any other procedure in which a robot is guiding a tool in close proximity to vital anatomy, provided that statistical estimates of the various system error sources are developed.

Next, a robotic mastoidectomy trajectory planning algorithm is presented that incorporates bone density and porosity as well as proximity to vital anatomy to improve the milling safety and efficiency (see Chapter 5, [34]). In contrast to constant velocity, Computer Numeric Control (CNC) type paths that are used in industrial machining and bone milling systems to date, this enables patient-specific path planning that reduces forces near vital anatomical structures. This force reduction improves the safety of the procedure and increases efficiency. Experiments were performed in custom-manufactured temporal bone surrogates to compare this approach to traditional CNC-type paths and show that forces are reduced using the new planning algorithm.

1.3.3 Safety analyses and improved drilling approaches for minimally invasive cochlear implantation surgery

The focus of the work then shifts to CI surgery, with an emphasis on further translating the minimally invasive approach towards clinical use. First, the influences of various anatomical configurations, including skull surface angle and mastoid air cell size/position on drilling accuracy were experimentally evaluated by performing the surgery in bone surrogate material and measuring the drilling deviation (see Chapter 6, [32]). The effects of these different anatomical features can be used to help plan safer, more accurate paths to the cochlea.

Second, the surgical approach is improved such that the risk of facial nerve damage due to excessive heat while drilling is minimized (see Chapter 7, [36, 37, 47]). This is accomplished by developing a revised surgical protocol that includes a patient-specific, pre-operative risk assessment as well as an improved drilling strategy. The pre-operative risk assessment uses the patient's CT scan to predict the amount of heat generated while drilling and estimate the conduction between the drill path and the nerve. The new drilling strategy, which is based on a thermal analysis of the bone drilling process, is then tested using a novel experimental setup that enables temperature measurement near the facial nerve of cadaver temporal bone specimens. The results indicate that the minimally invasive approach can reliably be performed safely on low to moderate risk patients and that high-risk patients are effectively excluded using the new pre-operative risk assessment.

Chapter 2

Analysis of Technical Requirements of Robotic Mastoidectomy

This chapter describes several analyses performed to develop a better understanding of the requirements for robotic mastoidectomy. The results can be used as design inputs for developing a robot for mastoidectomy and as guidelines for milling parameter selection. Section 2.1 describes a workspace analysis based on analyzing a set of mastoidectomies performed by surgeons on cadaver temporal bones. Section 2.2 describes experiments performed with an industrial robot in which forces were measured while milling human cadaver temporal bone under a range of parameters.

2.1 Mastoidectomy Workspace Analysis

2.1.1 Background and Motivation

One of the most critical inputs for robot design is the required workspace. This influences the selection of the kinematic structure of the robot as well as the overall robot dimensions. Given the anatomical variations, the size and drill orientation requirements can vary among patients requiring a mastoidectomy and the robot must bet designed such that it can perform the procedure on a wide range of patients. However, it is also important that the robot is not excessively large as this could lead to a unnecessary risk (e.g. the drill could reach areas unrelated to the surgery) and make it more difficult for the robot to fit within the workflow of otologic surgery. As such, a quantitative workspace analysis using anatomical data is necessary.

2.1.2 Materials and Methods

The required workspace of a robot for mastoidectomy was analyzed by examining a set of ten cadaveric temporal bone specimens on which mastoidectomies had been performed. The specimens were verified by an experienced surgeon as performed correctly. It is important to note that during mastoidectomy, the surgeons typically mill away a wide region of bone to facilitate identification of anatomy via various anatomical landmarks. A robotic system would utilize information in the pre-operative image to determine locations of all relevant vital anatomy. Thus, the volume of bone removed by the robot could potentially be specified to be smaller than the typical volume removed by a surgeon. However, for the purposes of an initial workspace analysis, clinically-relevant sized mastoidectomies were used in the since they represent a conservative estimate of the required workspace dimensions.

A photograph of one of the specimens is given in Figure 2.1. A Computed Tomography (CT) scan of each specimen was acquired (Xoran xCAT ENT, Xoran Technologies, Ann Arbor, MI, USA). The drilled volumes were segmented in each slice of the CT scans using a semi-automatic approach and the 2D slice segmentations were stacked to form a 3D volume. The 3D volumes were combined and analyzed in Matlab in two ways: (1) the overall required workspace size was calculated and (2) the

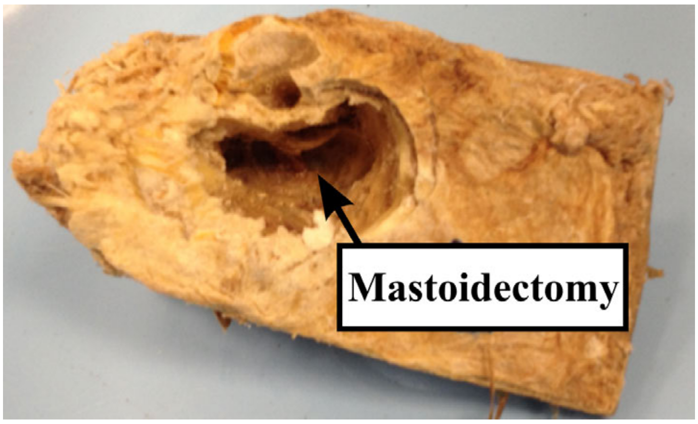

Figure 2.1: Photograph of cadaver temporal bone with mastoidectomy used in workspace analysis.

required tilt angles to safely reach all target points were determined.

Workspace Size

The face corresponding to the lateral surface of the skull was determined for each specimen and the centroid of this face was calculated. The ten specimens were aligned according to their lateral plane and centroid (See Figure 2.2). The minimum total volume that included all points from each of the ten specimens was then calculated. This volume was expanded by 10% to account for additional outliers and imperfect attachment in the operating room (OR), which could result in the target anatomy not being centered with respect to the patient.

Orientation Workspace Requirements

The angular workspace required for mastoidectomy was also analyzed using the same set of specimens. If the target volume was convex relative to the lateral surface, a simple x-y-z stage would be sufficient to reach all of the target points. However, it

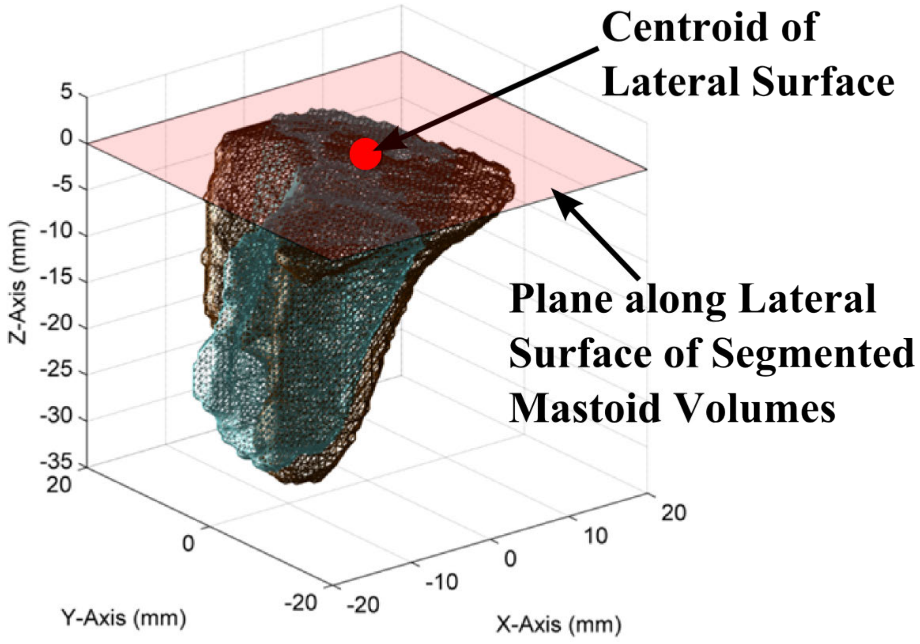

Figure 2.2: Multiple segmented mastoidectomy volumes were aligned along the lateral surface to calculate the required workspace volume of robot.

has been observed through these specimens and actual surgical procedures that the surgical volume to drill might include a cavity to be drilled that is partially overhung with bone, requiring a tilting of the drill. The tilt requirements were evaluated by calculating the drill angle(s) required to safely reach each of the surface points of the ten specimen volumes. An angle or set of angles was considered to be a safe combination, if a line extending out of the skull from the targeted point only passed through the targeted volume and did not cross into untargeted bone or vital anatomy (Figure 2.3). Two orientation cases were considered: one angular degree-of-freedom (DOF) (4 DOF total) and 2 angular DOF (5 DOF total). It was not necessary to consider three angular DOF since the drill bit rotates continuously about the shaft axis. The two orientation angles, θ and ϕ are shown in Figure 2.4.

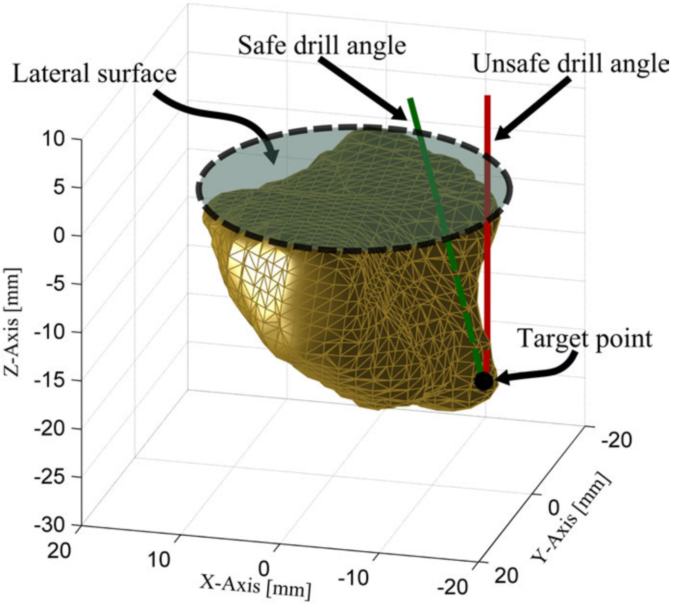

Figure 2.3: Drilled volume from a cadaver specimen with an example of safe and unsafe drill angles to reach a target location. At a safe drill angle (green), the shaft does not cross the boundary of the target volume except at the lateral surface. An unsafe drill angle (red) causes the shaft to touch untargeted bone and/or other anatomy.

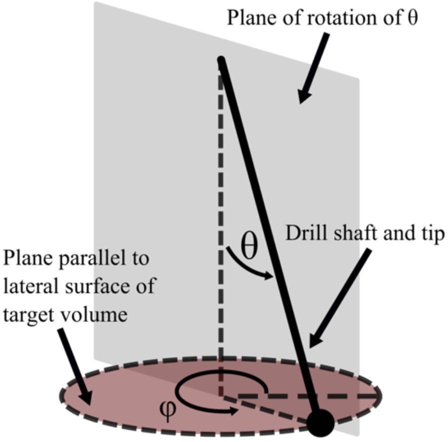

Figure 2.4: Angular DOF considered in workspace analysis. For the case of one angular DOF, ϕ is held constant and the drill can only rotate about θ. In the two DOF case, the drill can move about θ and ϕ.

To calculate the percentage of reachable points with one angular degree of freedom, ϕ was fixed at a given value and the percentage of points that could be reached safely was calculated. Several fixed values of ϕ (in increments of 30°) were selected and the angle that resulted in the highest percentage of points reached was used. In other words, it was assumed that the robot could be positioned on the skull such that its single angular DOF was approximately aligned with the overhung portion of the cavity. The required range of θ was then calculated based on the most extreme angles needed. For the case of two angular DOF, ϕ was also varied and the ranges of θ and ϕ were determined for each specimen.

2.1.3 Workspace Analysis Results

Workspace Size

The Cartesian workspace volume that encompass the drilled volumes of all specimens was determined to be approximately the shape of an inverted elliptical cone with maximum cross-section on the lateral surface. The major and minor diameters of the ellipse on the lateral surface (similar to dashed outline in Figure 2.3) were determined to be 52 mm and 45 mm, respectively, with the required depth being 41 mm.

Orientation Workspace Requirements

A very high percentage ($> 98\%$) of the surface points for each specimen were safely reachable using only one angular DOF (see Table 2.1). It was determined that, if using one angular DOF, a tilt angle (θ) of at least 50° is required. If another angular

Table 2.1: Percentage of points safely reached and associated required tilt range for various drill lengths.

Specimen No.	Number of Surface Points	Percentage Reached	Required Tilt (θ) Range
1	1978	100.0	25
2	1898	100.0	35
3	2288	98.3	50
4	2052	99.1	45
5	2876	100.0	45
6	1708	99.5	45
7	3416	100.0	20
8	1530	100.0	30
9	2238	100.0	35
10	2080	100.0	25

DOF is added, 100% of the points can be reached for all specimens.

Extension to Translabyrinthine Cases

The above analysis was then repeated specifically for translabyrinthine vestibular schwannoma cases, which involves mastoidectomy and labyrinthectomy. An experienced surgeon manually segmented on six patient scans the bone region to be removed to reach the internal auditory canal for accessing the tumor. These segmented volumes were analyzed in the same manner as the other ten mastoidectomy volumes. The required workspace for this procedure is similar to that of mastoidectomy with the exception that the depth requirement is 49 mm.

2.1.4 Discussion

The Cartesian workspace dimensions can be used to specify actuator travel lengths such that the reachable workspace encompasses these dimensions. The interpretation of the angular workspace results is not as straight forward. The orientation workspace requirements of the robot must be balanced with other design considerations, e.g. size and kinematic structure. For a serial manipulator, an additional DOF would likely result in an appreciable increase in kinematic positioning error and a reduction in stiffness. Thus, a lower DOF robot would be more desirable if the limited workspace did not significantly limit the effectiveness of the robot. Additionally, the robot must be more accurately mounted on the patient in the OR to ensure that the single angular DOF aligned with the appropriate anatomical direction. A parallel manipulator would not have the same accuracy and stiffness issues with additional actuators; however, the orientation requirement may result in a prohibitively large robot design.

2.2 Experimental Evaluation of Forces During Temporal Bone Milling

2.2.1 Background and Motivation

In order to design a robot, especially in the case of a compact bone-attached robot, to perform milling with a high level of accuracy, it is necessary to consider the forces between the tool tip and bone. This force data provides the design criteria for a robot that is stiff enough to not have displacements that would cross a given safety zone around these structures. To successfully execute a trajectory, the robot's motors must be adequately powered and controlled, and deformations of the robot's frame due to mechanical stresses must be minimized. The robot must be able to exert a specified force in the direction of the cut, while simultaneously rejecting disturbance forces in other directions so that it can maintain the desired trajectory within the specified accuracy. Therefore, knowledge of these forces is an essential component in determining the robot's kinematic design, selecting materials, and choosing actuators. Also, force information for different cutting parameters and bone types may enable the milling trajectory to be optimized. For example, if there is an area that is expected to induce larger forces due to the bone type or drill angle required in that area, specific depths and cutting velocities can be employed to ensure that the forces stay below a given threshold. In areas of the milling cavity that yield lower forces, faster and deeper cuts can be specified to minimize the time of the procedure.

Several prior studies have investigated the forces applied in both manual and robotic bone removal. Arbabtafti et al. performed several force measurement experiments to verify the accuracy of a haptic simulation of bone machining [4]. The authors examined the effects of drill angles, feed rates and spindle speeds on forces, when milling bovine femurs. The data presented indicates relationships between milling parameters and recorded forces in bone, suggesting a similar pattern may be identified for human temporal bone milling. Plaskso et al. tested forces and specific cutting energies for orthogonal milling in bovine cortical bone for the purpose of modeling and optimizing bone cutting for orthopedic surgery [104]. The authors selected cutting parameters similar to those used in clinical practice (very high cutting velocities and shallow depths of cut) and demonstrated that the cutting forces and specific cutting energy are significantly different than at lower speeds. Denis et al. examined the effects of feed per tooth and spindle speed on forces, surface flatness and temperature rise for robotic total knee arthroplasty procedures and concluded that forces increase with feed per tooth [27]. Bast and Englehardt examined manual milling forces, temperature, time of procedure, as well as accuracy of neurosurgeons of different skill levels using bovine scapula specimens [10]. They then compared robotic milling forces for craniotomies and craniectomies with a robot to that of milling forces of neurosurgeons performing the same procedure and found that the robot was faster, more accurate, and resulted in lower forces than the surgeons [39].

Federspil et al. tested milling forces on human temporal bones and also investigated using a robot to create the pocket for a cochlear implant bed [41–43]. The authors examined some of the parameters required for robotic bone milling by testing milling forces on two temporal bone specimens. Different drill rotational speeds, cutting velocities, various path parameters and burr types were tested and the authors provided a set of parameters for calvarium bone and mastoid bone (5 mm/s at 30,000 rpm in calvarium and 1 mm/s at 30,000 rpm in the mastoid) that best fit within a criterion of 10 N maximum force and 60°C maximum temperature. The study described in this section expands upon the prior work outlined above. It focuses on examining the milling forces across many temporal bone specimens for a wide range of cutting parameters and different bone types to aid in the design and trajectory optimization of a bone-attached milling robot for performing a mastoidectomy.

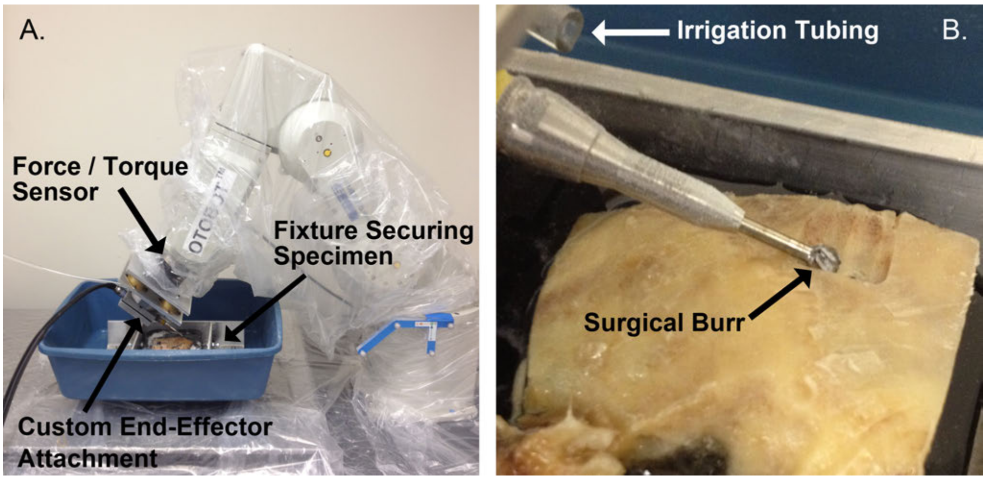

Figure 2.5: (a) Robotic milling force measurement experimental set-up, and (b) close-up photograph of 5 mm fluted burr milling temporal bone.

2.2.2 Experimental Methods

To measure milling forces in human temporal bone, an industrial robot was programmed to mill test specimens under a variety of cutting parameters. An apparatus was constructed to immobilize temporal bone specimens with respect to the base of the industrial robot (see Figure 2.5). The specimens were milled using a drill fixed to the end effector of the robot and force measurements were recorded.

A Mitsubishi RV-3S (Mitsubishi Electric and Electronics, USA, Inc., Cyprus, CA, USA) robot was used for the experiments, which has a repeatability of ±0.02 mm. An Anspach E-max high-powered electric drill (The Anspach Effort, Inc., Palm Beach Gardens, FL, USA) was fixed to the end-effector of the robot using a custom attachment piece, which also held the tubing used for irrigation of the drill tip and bone. This same model drill is used clinically by surgeons in the Otolaryngology department at Vanderbilt University Medical Center. It can operate at speeds up to 80,000 revolutions per minute and contains an integrated cooling system. A six-axis force/torque sensor (Gamma, ATI Industrial Automation, Apex, NC, USA) was mounted between the robot end-effector and surgical drill to measure the forces at the drill tip. The force measurements were recorded using a National Instruments DAQ (National Instruments Corp., Austin, TX, USA) at a sampling rate of 10,000 Hz. Defrosted formalin-fixed temporal bone specimens were used for all experimental trials. Formalin-fixed bones have been shown to have similar material properties to fresh cadaver bones and thus were considered an acceptable alternative to fresh bones in this study [21,121,123,131]. The specimens were potted in a urethane casting compound to immobilize them during milling with the portion of bone to be milled positioned 10-15 mm above the top of the urethane. The urethane block was securely fastened to a table approximately 0.5 m from the base of the robot.

In order to obtain accurate and consistent depths of cut, the area of the experimental milling path was pre-machined by the robot to create a flat surface. The flat surface was machined using the same cutting burr and drill angle as the subsequent experimental run(s) so the exact coordinates of the flat plane in the robot coordinate frame were known. This preparation method took advantage of the high pose repeatability of the robot and it is reasonable to assume that the error in depth of cut was reduced to the repeatability error of the robot (±0.02 mm) using this procedure. After the flat plane was created, an experimental cutting pass was made and the forces were measured in three orthogonal directions relative to the position of the force sensor. Based on the angle of the drill, the forces with respect to a coordinate frame at the surface of the bone could be calculated. This coordinate frame is shown

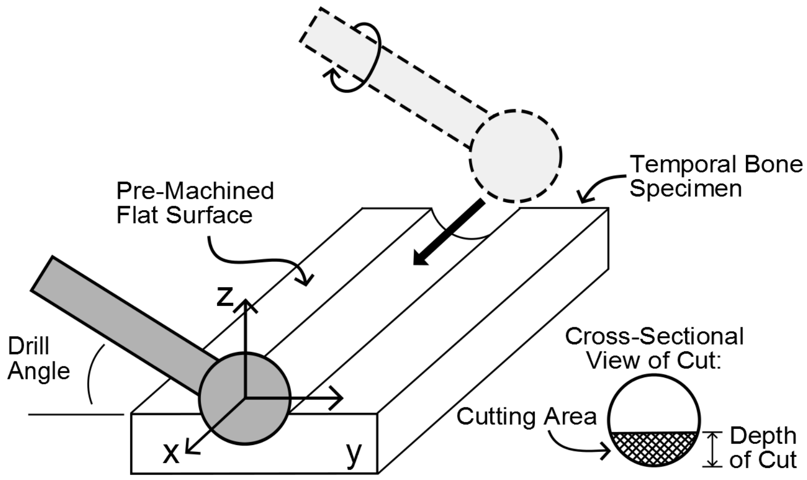

Figure 2.6: Schematic of drill moving through milling path. The surface of each bone was machined to a planar surface prior to each experimental milling trajectory for accurate determination of the drill angle and depth of cut. The bone removal rate was determined by the cross-sectional area of cut and the cutting velocity.

in Figure 2.6. The robot was programmed to move at a constant depth and cutting velocity for the entire experimental cutting pass, which varied between 14 and 18 mm based on the restricted amount of bone available to be milled in that particular area of the specimen. The cuts in cortical bone were performed as close to the surface as possible to allow for a large enough flat surface for a given cut. The cuts in the mastoid region were performed just below the cortical layer, approximately 4.0 to 6.0 mm below the surface of the bone.

Four sets of experiments were performed to measure forces when milling using the parameters listed in Table 2.2. In all experiments, the milling was performed using the climb milling approach (i.e. the burr spins such that the flutes contact the bone in the opposite direction as the motion of the burr, see Figure 2.6). Along with

Table 2.2: Parameters tested in milling force measurement experiments.

Parameter	**Experimental Range**
Burr Diameter and Type	3 mm Fluted, 5 mm Fluted, 3 mm Diamond
Drill Angle	$20 - 90°$
Depth of Cut	0.62-1.64 mm
Cutting Velocity (Feed)	1-8 mm/s
Spindle Speed	80,000 rpm (held constant)

developing robot design criteria, an objective of this study was to acquire data to aid in optimizing milling parameters. Thus it was important to first develop a relationship between cutting forces and bone removal rate for the different burr types so that a burr could be chosen that minimizes the overall duration of the milling procedure while maintaining relatively low required forces from the robot. In manual milling procedures, the surgeon will often change burr types for different areas of the milling cavity. However, in a robotic system, it is desirable to use fewer burrs if possible in order to minimize the overall time of the procedure and avoid complications related to re-registering the images of the patient anatomy to the robot coordinate frame after the burr is changed.

It is also necessary to compare different cutting angles since certain areas of the milling cavity permit different drill orientations. Thus it is important to identify any differences in forces for the various orientations. Next, it is important to compare the forces at various depths of cut and cutting velocities. Together with the burr size, these parameters determine the bone removal rate and, in turn, the duration of a procedure given the size of the cavity to be milled. In solid bone, the bone removal rate is equivalent to the cross-sectional area of the burr engaged with the bone multiplied by the linear cutting velocity as shown in Figure 2.6. The bone removal rate has units of volume of bone over time. In addition to choosing a bone removal rate, it may be possible to choose the combination of depth and cutting velocity for a specific rate that yields lower forces. Therefore, the different depths and velocities tested were selected to enable comparison of each parameter individually, comparison of different bone removal rates, and comparison of parameter combinations for a specific removal rate. Finally, since a mastoidectomy requires the removal of both cortical and trabecular bone, these two bone types were tested and compared. Due to the variability in both hardness and porosity in bone between various specimens, each trial for a given set of cutting parameters was performed in a different specimen and, in most cases, a given specimen was used for one trial of each set of parameters being compared.

Comparison of Cutting Burr Types

Three cutting burrs that are used frequently in otologic surgery were selected for comparison: a 5 mm diameter fluted burr, a 3 mm diameter fluted burr, and a 3 mm diameter diamond-coated burr (see Figure 2.7). Fluted burrs have cutting blades which remove tissue by cutting radially from the center of the bit while diamond burrs have industrial diamonds embedded on their surface to radially abrade tissue. They were tested in cortical bone at a fixed angle of 20° and drill speed of 80,000 rpm under two different combinations of cutting velocity and depth of cut. The velocities and depths were chosen such that the bone removal rates were the same for the 3 mm

Figure 2.7: Photograph of surgical cutting burrs used in experiments; from left to right: 5 mm fluted, 3 mm fluted, and 3 mm diamond coated burr

and 5 mm burrs (i.e. the 3 mm burr must cut faster at a given depth or deeper at a given velocity to remove the same amount of bone as the larger burr). In one of the bone removal rates the cutting velocity for the different burr sizes were equal (depths varied) and in the other bone removal rate the depths were equal (velocity varied).

Comparison of Drill Angles

In the next experiment, drill angles of 20°, 40°, 60° and 90° were tested. The drill angle is measured from the planar surface of the bone (see Figure 2.6). Lower angles utilize more of the side of the burr while higher angles utilize more of the tip of the burr. For all of these trials, which were performed in cortical bone, a 5 mm fluted burr was used along with a spindle speed of 80,000 rpm, cutting velocity of 2 mm/s, and depth of 1 mm.

Comparison of Various Depths of Cut and Cutting Velocities

To test different combinations of depths of cut and cutting velocities, depths were chosen between 0.62 mm and 1.64 mm, and cutting velocities were chosen between 1

Table 2.3: Parameter combinations tested for different bone removal rates.

Depth (mm)	Velocity (mm/s)	Bone Removal Rate (mm^3/s)
0.62	2.0, 4.0, 8.0	2.8, 5.6, 11.2
1.00	1.0, 2.0, 4.0, 6.0	2.8, 5.6, 11.2, 16.8
1.33	1.0, 2.0, 4.0, 5.35	4.2, 8.4, 16.8, 22.4
1.64	1.0, 2.0, 4.0	5.6, 11.2, 22.4

and 8 mm/s for a total of fourteen different combinations (see Table 2.3). The depth of cut and velocity combinations tested were chosen in part to enable comparison of different depth and cutting velocity combinations that resulted in the same overall bone removal rate. For all of the trials in this study, a 5 mm fluted burr was used at an angle of 20° and a drill spindle speed of 80,000 rpm. Again, cortical bone in the temporal bone of a human skull was used for all trials.

Comparison of Different Bone Types

In the final experiment, a subset of the parameters used previously in cortical bone was tested in trabecular bone in the mastoid region (see Figure 2.8). Three depth/velocity combinations were chosen for comparisons at multiple sets of cutting parameters. Since there is more variation in the mastoid within a single specimen than in cortical bone, two trials for each mastoid specimen were performed, compared to one trial per specimen in cortical bone.

In each trial for all four of the experiments discussed above, only the force measurements after the burr was completely engaged in the bone were considered; the “transient” portion of the data, as the forces rose from zero to their relatively “steady-

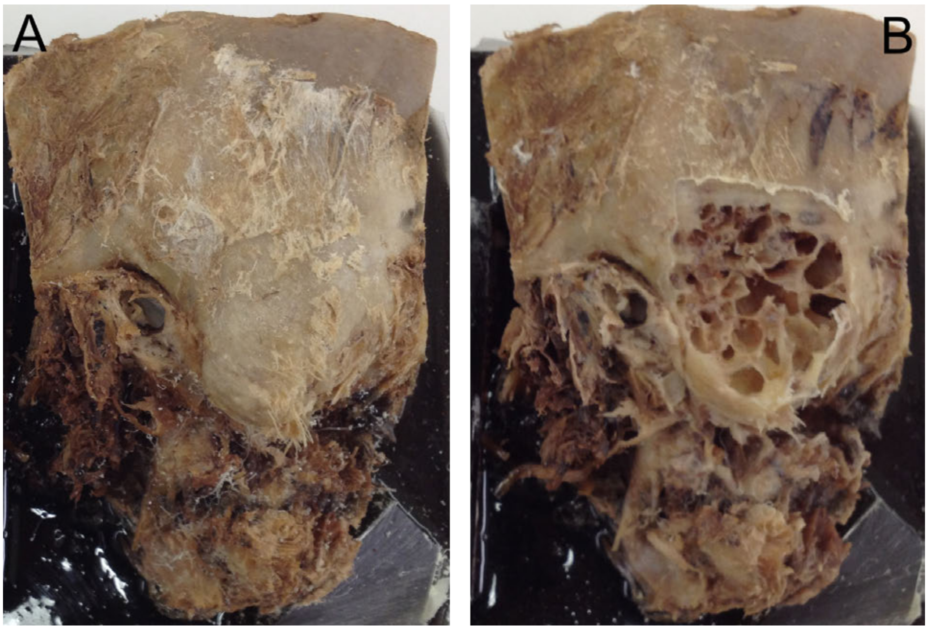

Figure 2.8: (a) Photograph of a temporal bone specimen prior to milling, and (b) after experimental trials showing the trabecular bone of the mastoid region.

state" value, was removed. Figure 2.9 shows an example of the recorded forces for a typical trial, including the transient rise in forces. Once steady-state was achieved, mean force values for each condition over the remaining portion of the trial were generated. Comparisons of two sets of mean force values were conducted using independent samples t-tests. Comparisons of more than two sets of mean force values were initially tested using a one-way analysis of variance (ANOVA). If there was a statistically significant difference among the means, post-hoc pairwise comparisons were conducted to determine which specific pairs of differences were accounting for the overall finding. If the assumption of homogeneity of means was met, Bonferroni adjusted post-hoc tests were used; if not, Dunnett C tests were used. Other than for the post-hoc tests, no adjustment to the overall alpha (α) of 0.05 was used. In other words, an α of 0.05 ($p < 0.05$) was used to determine statistical significance.

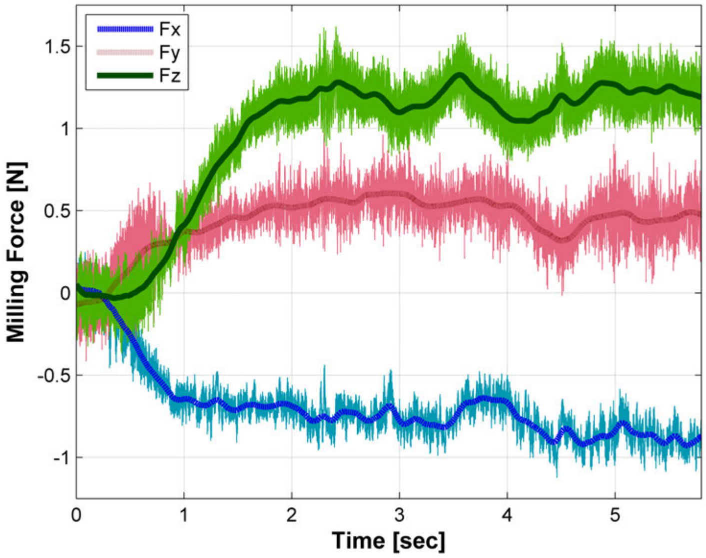

Figure 2.9: Typical plot of raw and filtered (central moving average) experimental data in cortical bone. This plot shows a trial using a 3 mm fluted burr at an angle of 20° relative to the bone, a depth of cut of 1.0 mm, and a velocity of 2.0 mm/s.

2.2.3 Experimental Results

Comparison of Cutting Burr Types

In the first experiment, the 5 mm fluted burr achieved bone removal rates with lower forces than both the 3 mm fluted and the 3 mm diamond burrs (see Figure 2.10). For a bone removal rate of 4.1 mm^3/s, the mean force exerted on the 5 mm fluted burr was 0.75 N (±0.28 N) lower than the 3 mm fluted burr ($p = 0.041$) and 1.16 N (±0.28 N) lower than the 3 mm diamond burr ($p = 0.001$). For a bone removal rate of 8.4 mm^3/s, the mean force exerted on the 5 mm fluted burr was 0.90 N (±0.27 N) less than the 3 mm fluted burr ($p = 0.009$) and 1.37 N (±0.27 N) lower than the 3 mm diamond burr ($p < 0.001$). The difference in cutting forces between the two different

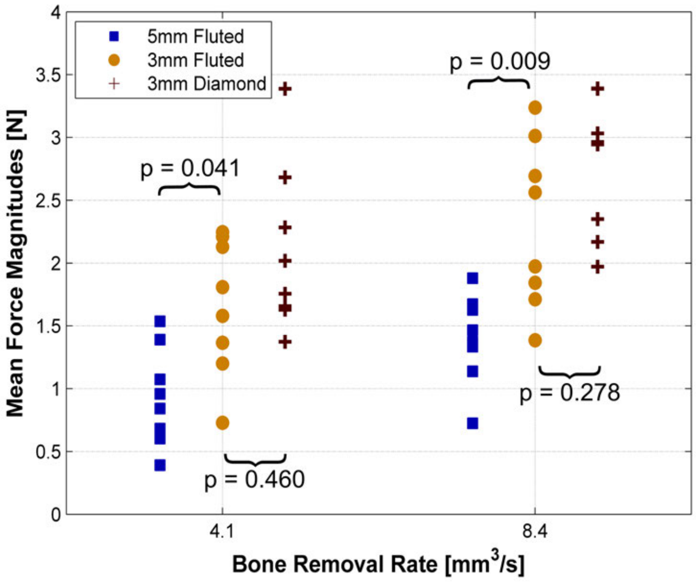

Figure 2.10: Comparison of mean force magnitude for the 5 mm fluted, 3 mm fluted, and 3 mm diamond burrs. For both bone removal rates, the 5 mm fluted burr had lower mean forces.

3 mm burr styles was not statistically significant. Since the forces were lower for the 5 mm fluted burr and the larger burr enables more depth and velocity combinations for a given bone removal rate, the 5 mm fluted burr was chosen to be used for the other experiments.

Comparison of Drill Angles

In the second experiment, four drill angles (20°, 40°, 60°, 90°) were compared using the 5 mm fluted burr and constant spindle speed, cutting depth and linear cutting velocity. The mean and maximum forces recorded for each trial of the four angles tested are given in. There was not a statistically significant difference in mean forces between these angles; however, the maximum forces measured were higher for greater

Table 2.4: Milling force measurement results for various drill orientation angles.

Trial No.	**20°**		**40°**		**60°**		**90°**	
	Mean	**Max**	**Mean**	**Max**	**Mean**	**Max**	**Mean**	**Max**
1	0.91	1.67	0.81	1.95	1.08	2.87	0.98	2.45
2	1.12	2.24	0.75	1.61	0.92	2.12	1.27	3.58
3	1.12	1.75	0.90	2.88	1.76	2.57	1.56	5.11
4	1.50	2.57	1.41	2.67	1.62	2.50	1.40	3.65
5	0.97	1.41	1.29	2.30	1.46	2.53	1.15	4.59
6	1.07	1.54	1.53	2.28	1.85	3.01	1.01	5.41
7	0.89	1.84	1.16	2.67	1.24	2.72	1.36	4.36
8	0.46	1.57	0.55	1.63	0.61	2.35	0.87	13.13
Mean (Std)	**1.01 (0.30)**		**1.05 (0.35)**		**1.32 (0.43)**		**1.20 (0.24)**	

[a] All values are given in Newtons (N)

[b] All trials performed in cortical bone with a 5 mm fluted burr, 1 mm depth of cut, cutting velocity of 2 mm/s, and spindle speed of 80,000 rpm.

cutting angles (see Table 2.4).

Comparison of Various Depths of Cut and Cutting Velocities

As seen in Figures 2.11 and 2.12, the mean cutting force increased as depth of cut and cutting velocity increased as expected. The mean cutting force increased more sharply for increases in depth of cut compared to increases in cutting velocity. Five of the bone removal rates included in the experiment were tested with multiple depth/velocity combinations. In each of these cases (see Table 2.5), the mean force was lower for the settings that had a shallower depth of cut and faster cutting velocity.

Table 2.5: Statistical comparison of milling force results for depth/velocity combinations for a given bone removal rate.

Bone Removal Rate (mm^3/s)	Depth (mm), Vel. (mm/s)		Mean Diff., #1 - #2 (N)	Std. Error (N)	*p* Value
	Set #1	Set #2			
2.8	0.62, 2.0	1.0, 1.0	-0.26	0.11	0.039
5.6	0.62, 4.0	1.0, 2.0	-0.12	0.09	0.596
	0.62, 4.0	1.64, 1.0	-0.92	0.09	<0.001
	1.0, 2.0	1.64, 1.0	-0.80	0.09	<0.001
11.2	0.62, 8.0	1.0, 4.0	-0.29	0.07	<0.05[a]
	0.62, 8.0	1.64, 2.0	-1.36	0.18	<0.05[a]
	1.0, 4.0	1.64, 2.0	-1.07	0.18	<0.05[a]
16.8	1.0, 6.0	1.33, 4.0	-0.40	0.16	0.028
22.4	1.33, 5.35	1.64, 4.0	-0.55	0.22	0.058

[a] Due to inhomogeneous variances, Dunnett C test was used and exact p-value not given.

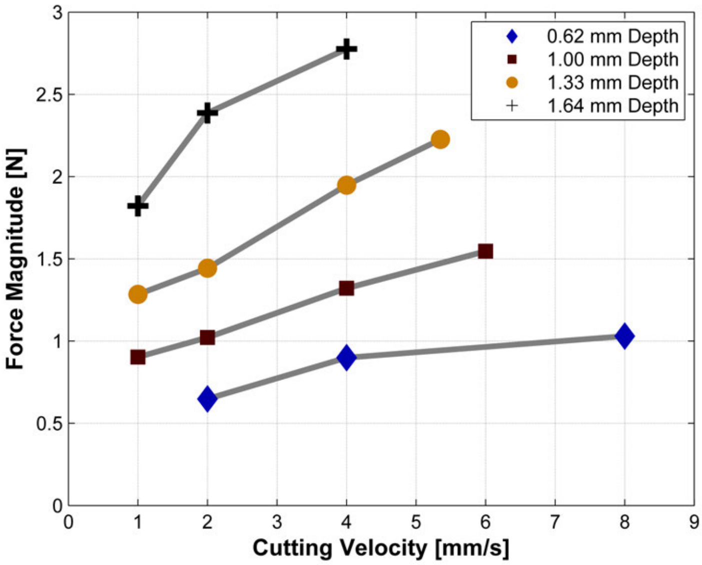

Figure 2.11: Comparison of mean force magnitudes for various linear cutting velocities at four different depths of cut (5 mm fluted burr used for these experiments).

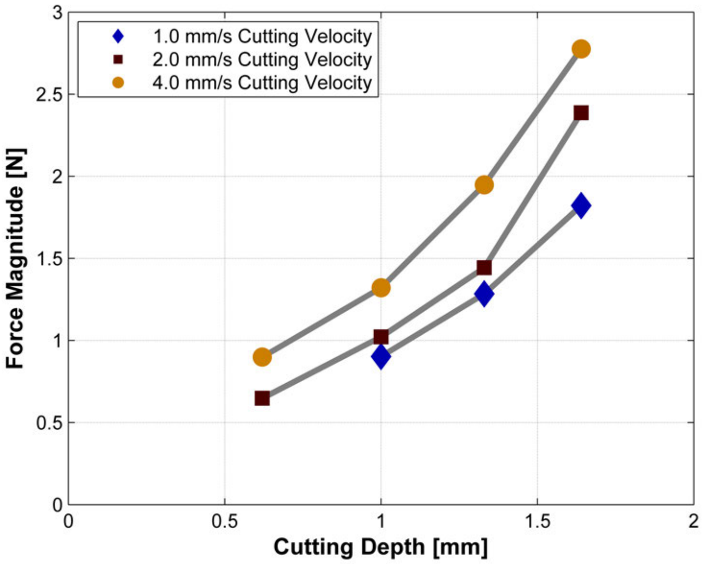

Figure 2.12: Comparison of mean force magnitudes for various cutting depths at three different linear cutting velocities (5 mm fluted burr used for these experiments).

Comparison of Different Bone Types

In the final portion of this study, the forces arising in the trabecular bone within the mastoid were significantly lower than in cortical bone for the two cases tested using higher depths and velocities. Additionally, the variability in force was higher for the trabecular bone in both cases. For a depth of 1.0 mm and velocity of 4.0 mm/s, the mean force was 1.32 N for cortical bone with a coefficient of variance of 0.13 compared to a mean force of 0.86 N for trabecular bone with a coefficient of variance of 0.56 ($p < 0.001$ for comparison of mean forces). For a depth of 1.64 mm and velocity of 4.0 mm/s, the mean force was 2.77 N for cortical bone with a coefficient of variance of 0.12 compared to a mean force of 1.44 N for trabecular bone with a coefficient of variance of 0.44 ($p = 0.016$ for comparison of mean forces). For

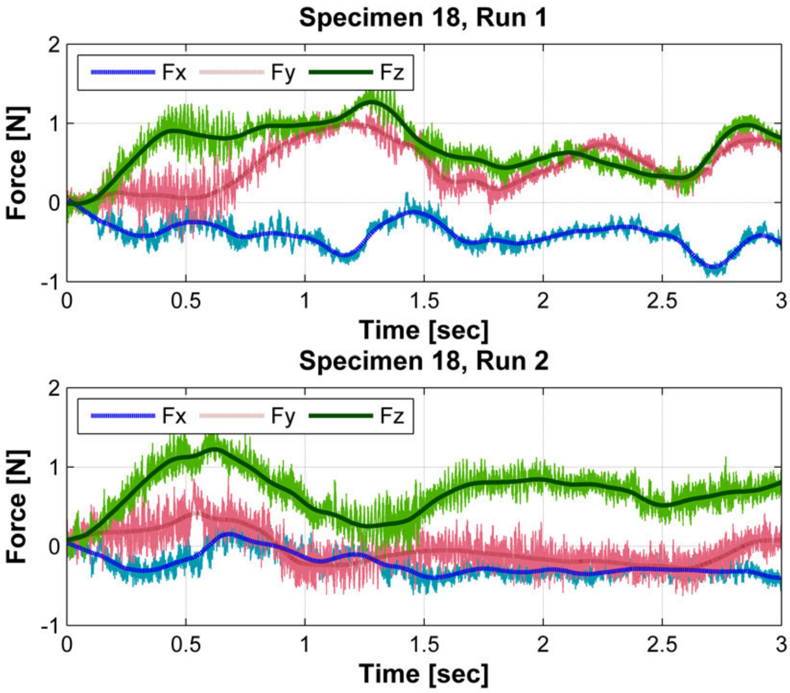

Figure 2.13: Examples of milling forces in the mastoid. Lower overall forces were observed in the mastoid than in cortical bone, though both the direction and magnitude of the force showed greater variance than in cortical bone (5 mm fluted burr used for these experiments).

the shallower/slower set of parameters (1.0 mm, 1.0 mm/s), the forces for both bone types were very low so there was not a statistically significant difference in mean force values ($p = 0.077$). Even within a single specimen, the forces can vary considerably between cutting paths so two trials for each set of parameters were performed in each of the eight specimens. Figure 2.13 shows the variability along a cutting path in the mastoid as well as the potential difference in both magnitude and direction of force from one path to another.

2.2.4 Discussion

Since forces at the drill tip are transferred up the shaft and result in deflection of the robot, these forces have a direct effect on the accuracy of the robot. Therefore, it is necessary to incorporate this force information, along with the necessary robot workspace, required accuracy and size constraints, into the design of a bone-attached robot for mastoidectomy and other skull-based surgeries. In addition to its use in the design process, the force data presented in this study can be used to optimize the milling trajectory such that the forces at the drill tip are minimized. The lower force using the 5 mm burr compared to the 3 mm burr at similar bone removal rates enables faster removal of the target bone volume. Compact robots are inherently limited in the force that they can produce and withstand, thus it is desirable to use the larger burr when possible to achieve a given bone removal rate. However, geometrical constraints of the milling cavity and the critical anatomy within the cavity do not always permit larger burr sizes so these constraints must be balanced with the expected forces when choosing the appropriate burr and cutting/trajectory specifications.

The mean forces at the drill tip do not appear to be significantly affected by the drill angle. However, relatively large force spikes were observed at greater drill angles, suggesting that the angle of the burr relative to the cutting surface should be minimized when possible. While milling larger areas such as the layer of cortical bone and the outer portion of the mastoidectomy it is possible to cut at very small angles, thus utilizing the side portion of the burr for the majority of the cut. However, for the portions of the trajectory that are deeper in the skull, it is not always possible to cut at optimal angles. In these areas, the cutting velocity and/or depth of cut must be reduced to avoid large increases in force that could affect the accuracy of the robot.

Lower forces were observed for the same bone removal rate for parameter combinations that utilized shallower depths and higher cutting velocities compared with deeper cuts at lower velocities. This information can be applied to the design of the robot by specifying actuators and gearing that provide higher end-effector velocities. Furthermore, the time for a robotic procedure can be reduced without increasing forces on the robot and thus impacting the accuracy by limiting the depth of cut and increasing the cutting velocity. Although none of the cutting parameters tested in this experiment resulted in mean forces higher than 5 N, higher values should be anticipated in the design of the robot to account for potential spikes in forces as seen in the angle comparison trials at higher angles and as a general factor of safety. This factor of safety will also account for any differences between the experimental forces measured in formalin-fixed bones and forces in vivo.

The different forces arising in cortical bone compared with the pneumatized bone of the mastoid can also be applied to planning the milling trajectory. The robot should be designed to withstand the higher forces that occur while milling cortical bone but specifying different cutting parameters in the mastoid region enables optimal path planning. However, the cumulative density of bone in the mastoid, accounting for both bone and air, can differ significantly from patient to patient. In general, milling in well-pneumatized bone results in lower forces for a given depth and cutting velocity as there is a lower amount of bone to be removed overall. However, due to the irregularity of the bone and air patterns, the burr can be in contact with different quantities of bone throughout the cut leading to more variability. Even within a single specimen, the forces can vary significantly between cutting paths. A topic of future work in this area could focus on developing a relationship between milling forces and bone density in the mastoid, air pocket sizes and patterns to facilitate for further improvements of the planned trajectory and patient-specific cutting parameter ranges.

Chapter 3

Design and Testing of a Compact, Bone-Attached Robot for Mastoidectomy

This chapter presents the design and testing of a bone-attached robotic system for mastoidectomy. First, the use of bone-attached robots in other surgical specialties is reviewed. Next, the surgical workflow and trajectory planning for the proposed system are presented, followed by the design and experimental evaluation of two custom prototypes.

3.1 Overview of Bone-Attached Robots

A key component of any image-guided robotic system is the registration (i.e. alignment) between the robot and the anatomy of the patient in the operating room. If a robot is programmed to execute a task specified in the pre-operative image, the anatomical features and target trajectory from the image must be registered to physical space so that the robot can be programmed to move to the desired positions. A common method of aligning the various components of an image-guided system with the patient is to use an optical tracking system (for example, the Polaris Spectra, Northern Digital Inc., NDI Polaris, Waterloo, Canada). Tracked markers are fixed to both the patient and the surgical tool to determine the relative positions. The pre- or intra-operative image can be registered to the tracking system, and therefore the robot, with several methods. A tracked probe can be used to touch various points on the patient, which can then be registered to a surface or corresponding points in the image. Alternatively, bone-implanted fiducial markers, which provide a more reliable registration, can be localized with a tracked probe. Throughout the surgery, the markers on the robot and patient are monitored and any relative motion is compensated for by adjusting the robot trajectory.

Despite improvements in surgical navigation technology, which have decreased localization error of tracked markers to under a millimeter, the tracking and alignment inherently adds some level of error to the surgical system. Additionally, tracking systems increase the complexity and cost of any image-guided surgical robot. As an alternative, bone-attached robots have been proposed. Since the robot is rigidly affixed to the patient, there is minimal relative motion and, thus, no need to track the robot throughout the procedure (other than for a redundant safety check). If bone-implanted fiducial markers that also serve as attachment points for the robot are inserted before the pre- or intra-operative image acquisition, the robot can be aligned directly to the image according to the locations of these attachment points and a simple rigid registration.

Prior work using bone-attached robots has shown them to be capable of milling bone in orthopedic surgery [19, 103, 128] as well as aligning a drill for minimally invasive pedicle screw placement for spinal surgery. [28, 109]. More recently, bone-attached robots have been used as adjustable stereotactic frames for minimally invasive cochlear implantation surgery [66, 70]. This prior work guided the approach for

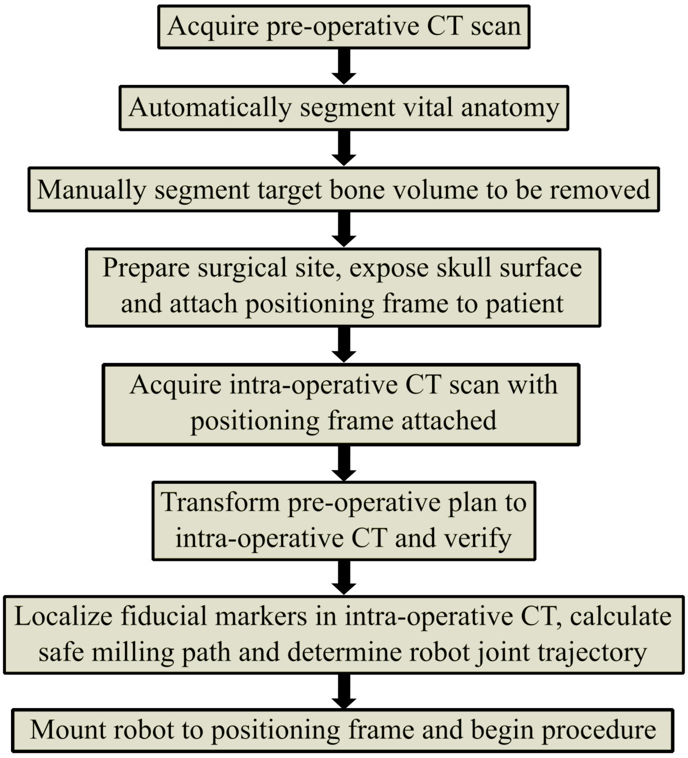

Figure 3.1: Clinical workflow of bone-attached robotic system.

the mastoidectomy robot presented below.

3.2 Surgical Work Flow

With the proposed robotic system, the workflow of the surgery involves pre-operative planning followed by a series of steps performed in the operating room (see Figure 3.1). First, vital structures are segmented automatically in the pre-operative computed tomography (CT) scan, including the facial nerve, chorda tympani, external auditory canal, semicircular canals, and ossicles using previously developed methods [93, 95]. Using the locations of these structures as guidance, the volume of bone to be removed in surgery is then manually segmented by the surgeon in the CT scan. The

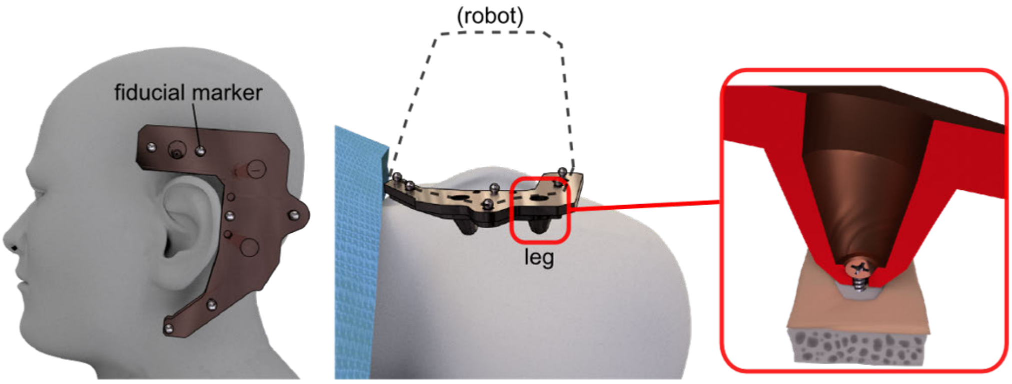

Figure 3.2: The robot positioning frame is fixed to the patient using cranial plating screws prior to acquiring an intra-operative CT scan. The positioning frame contains mounting points for the robot and fiducial markers for registration.

two-dimensional slice segmentations are then combined to form a three-dimensional volume of bone to be removed.

In the operating room, the surgical site is prepared by exposing the bone surface in the area around the mastoid. Then, a positioning frame, which serves as an intermediate attachment piece between the robot and the patient, is attached to the patient using small screws via stab incisions (see Figure 3.2). The positioning frame contains metal (titanium and steel) spheres used to register the robot to the patient's anatomy. Three of the spheres are also used as attachment points for mounting the robot. An intra-operative CT scan of the patient with the positioning frame attached is then acquired. The CT is ideally performed in the operating room using either a portable CT scanner (e.g. xCAT ENT mobile CT scanner; Xoran Technologies, Ann Arbor, MI) or a fixed uni- or bi-plane rotational fluoroscopy machine. The intra-operative CT is registered to the pre-operative CT using intensity-based registration based on mutual information [86] and the pre-operative segmentations are transformed to the intra-operative CT using the registration. The robot is designed to attach to the spheres on the positioning frame in a known configuration. Localizing the spheres in the image, which is done automatically [85], allows for the segmentation data to be transformed to the robot coordinate system by applying a rigid, point-based registration using the sphere locations. The milling path is then calculated using a custom path-planning algorithm and a robot trajectory is generated (described in Section 3.3).

Next, the robot is attached to the positioning frame and commanded to follow the planned milling trajectory. The procedure is monitored by the surgeon under direct visualization or using a surgical microscope. He/she can adjust the speed of the robot, pause the robot, or stop the procedure at any time. Once the milling is complete, the robot is removed, and the surgeon performs any additional steps to complete the surgery, e.g. cochlear implant (CI) electrode insertion, acoustic neuroma tumor removal, etc.

3.3 Trajectory Planning

The path planning algorithm is an extension of an algorithm Danilchenko et al. used in earlier robotic mastoidectomy experiments with an industrial robot [22, 23]. The input to this algorithm is a three-dimensional array of voxel elements such that each voxel's value serves as a label differentiating between air, targeted bone, forbidden bone, and the start point. The original algorithm finds a path for the drill's center that begins at the starting point, passes through every target voxel while avoiding all forbidden voxels, and returns to the start point. Here, Danilchenko's algorithm is extended in two important ways to model physical drill bit geometry. Danilchenko's algorithm assumes that the drill bit occupies only one cubic voxel and visits every voxel to be removed. However, a standard surgical bit is a sphere that covers many voxels.

First, to compensate for the size and shape of the bit, morphological operations are used. Figure 3.3a shows an example voxel input array for the path planning algorithm. While the actual arrays are three-dimensional, a two-dimensional example is shown here to simplify the explanation. In the figure, R1 (black) is the forbidden region and the union of regions R2 (dark gray), R3 (light gray), and R4 (white) is the targeted voxel region input to the planning algorithm, which is intended to be removed with the drill bit if possible (it is the region the surgeon segmented that he/she desired the robot to remove). To ensure the preservation of the forbidden region, R1, the algorithm's input array is modified using the morphological image-processing operation known as dilation [114]. Dilation of a region expands its original boundary into its surroundings in a manner determined by the size and shape of a specified "structuring element". The structuring element used to dilate R1 in this approach is the circle shown centered on P1 (sphere in the three-dimensional case). The identical disk surrounding P2 depicts the drill bit at a specific point on the output path. The dimensions of the structuring element are chosen to match those of the drill bit. The dilation of R1 is accomplished by placing the center of the structuring element on every voxel in R1 and moving all voxels within the structuring element into R2. The new dilated forbidden region is the combination of R1, R2, and R4.

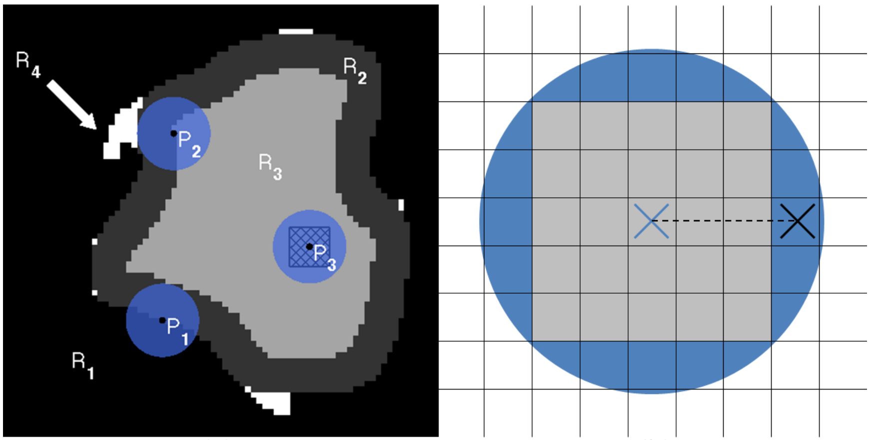

(a) (b)

Figure 3.3: (a) Illustration of the use of dilation to accommodate the finite size of the drill bit. The input targeted region is the combination of R2, R3, and R4. Black is the forbidden region, R1. Output targeted region, R3, is light gray. The circular disk centered on P1 represents the structuring element during preprocessing; the disk at P2 represents the drill bit during ablation; and P3 illustrates the super-voxel (hatched square). R2 represents target voxels that will be removed by the edge of the drill. The white regions, R4, are unreachable because of the bluntness of the bit. (b) Two dimensional illustration of how the super-voxel approach improves the efficiency of the drilling process. The gray cells form the super-voxel within the drill bit (blue circle) centered at the blue cross. When the drill bit is active at this location, all voxels within the super-voxel will be considered as hit and removed from the list of remaining target voxels. The next location for the center of the drill bit is the center of the nearest voxel outside the super-voxel, shown as the black cross. The cutting depth is the distance between the two crosses (length of the dashed line).

The resultant modified targeted region, R3, serves as input to the path-planning algorithm, which determines a path for the center of the drill bit through a sequence of R3 voxels such that all of the voxels in R2 and R3 are removed by some portion of the spherical drill tip. The drill's position, P2, in the target region has been chosen in Figure 3.3 to illustrate a limitation imposed by the bit's physical shape and size. Voxels in R4 are located such that they cannot be removed by the drill bit without also removing at least one forbidden voxel. This problem is a consequence of the dimensions of the bit and also exists when the drilling is performed manually. These unreachable nooks are filled in during the pre-processing dilation. Additionally, a check for connectedness ensures that any isolated, unreachable pockets of R3 are eliminated. All forbidden voxels are protected at the expense of allowing some targeted voxels to remain undrilled, ensuring that the algorithm adheres to the rule "first do no harm". The drill angle associated with each target voxel is determined after the path is generated based on the location of the drill bit within the volume, the locations of nearby undrilled voxels, and potential collisions between the shaft and undrilled/untargeted bone. This component of the trajectory planning (i.e. converting a three-dimensional path to a 4 degree-of-freedom (DOF), patient-specific robot joint space trajectory) is discussed in detail in Chapter 5.

The second modification of Danilchenko's original algorithm stems from its requirement that the drill bit's center visits each target voxel, thereby leaving the relationship between the bit's physical size and the dimensions of the target voxels unexploited. The size of the drill bit is accounted for as it passes through the target voxel region, R3, by creating a "super-voxel" centered on the drill bit and consisting of a group of target voxels whose size is determined by the desired cutting depth. As the path of the drill's center is planned through R3, all of the target voxels within the super-voxel are considered to be removed (hatched square within P3 shown in Figure 3.3a). The identification of these voxels increases efficiency and results in considerable time savings. An exception to this rule occurs at those voxels in R3 that border R2. These voxels must be touched with the center of the drill bit to ensure that the entire original target region is removed. The super-voxel approach enables the adjustment of the cutting depth bit by changing the number of target voxels contained within the super-voxel. For example, without the super-voxel approach, given a voxel size of 0.4 x 0.4 x 0.4 mm, the commanded cutting depth of the drill would be 0.4 mm. Using the super-voxel approach, the cutting depth would be equal to the distance between the center of the super-voxel to the center of the nearest voxel outside the super-voxel (Figure 3.3b). For example, given an image with voxel size of 0.4 x 0.4 x 0.4 mm and a 5 x 5 x 5 super-voxel, the cutting depth will be 1.2 mm.

3.4 Design and Experimentation with First Prototype

3.4.1 Robot Design

For a first prototype, a 4 DOF, serial manipulator with a tilt angle range of 60° was selected. When choosing the kinematic structure of the robot (i.e. one or two angular DOF, see Section 2.1), factors such as complexity, kinematic error, and workspace

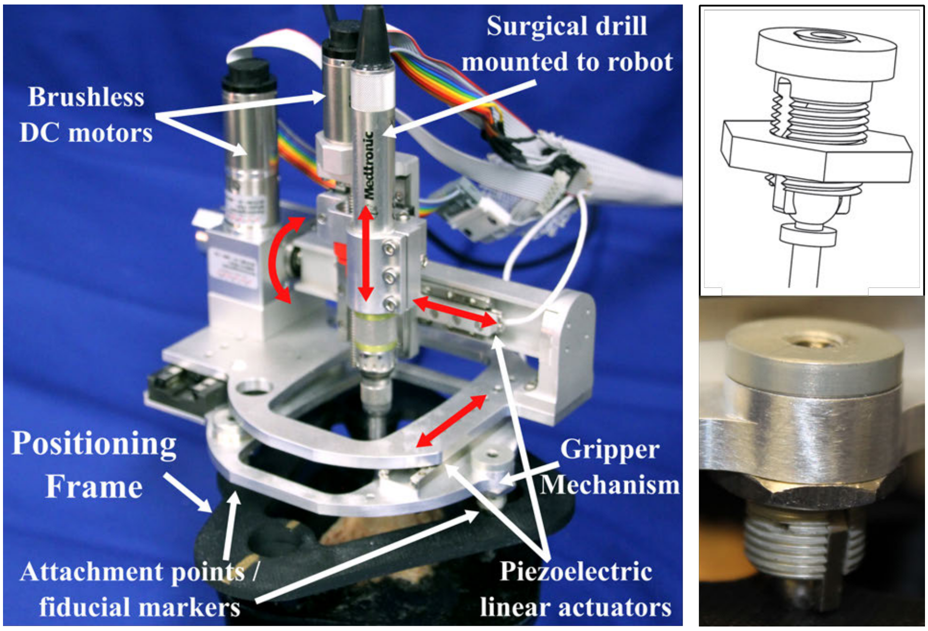

Figure 3.4: First prototype of bone-attached robot for mastoidectomy (left) and gripper mechanisms used to mount robot to the positioning frame (right).

dimensions were considered. It was determined that a tool could be built that could align the robot on the patient to best utilize a single angular DOF and that the added workspace of a 5 DOF manipulator was outweighed by the increased size, complexity, and error propagation. A custom robot with three translational joints and one rotational joint, analogous to a four-axis Computer Numeric Control (CNC) milling machine was designed and constructed (Figure 3.4). Two different types of actuators are used: piezoelectric linear actuators (SmarAct GmbH, Oldenburg, Germany) and brushless DC motors (Maxon Precision Motor, Inc., Fall River, MA, USA). The primary advantages of the piezoelectric actuators are their compact size and sterilizability. Initially, these actuators were planned for use in all joints; however, their limited blocking force when subjected to high frequency vibrations from the surgical drill did not permit them to be used for the two distal joints (z and θ axes).

Because of this limitation, a brushless motor and lead screw mechanism is used for the z-direction linear joint (the direction into the skull), and a brushless motor and anti-backlash worm-wheel gearbox (Gysin AG, Itingen, Switzerland) is used for the rotational joint. A design goal for the final, clinical version of this device is for it to be completely sterilizable. The brushless motors used in this prototype are not sterilizable, but several manufacturers offer sterilizable versions (steam sterilization up to 273° F) of similar size and power which could be utilized in future versions.

The robot is fixed to the patient via the positioning frame (see Figures 3.2 and 3.4), which is attached to the patient's skull using small screws. The robot mounts to the three spheres on the positioning frame with spherical gripper locking mechanisms (Figure 3.4). The drill spindle speed is controlled with a foot pedal and the robot motion is controlled by the surgeon with a small hand piece or computer interface.

3.4.2 Accuracy Evaluation

The free-space accuracy of the system was evaluated using the virtual target method described in [8] using a custom phantom and drill probe (Figure 3.5). Prototype 1 described in the previous section was used for these experiments. The robot attaches to the top of the phantom via three titanium spheres similar to how it would attach to the positioning frame. Seventeen titanium spheres are embedded on the bottom of the phantom to serve as validation markers to register the CT scan of the phantom to the coordinate measurement machine (CMM) used to test the accuracy in these experiments. The CMM used is a FARO GagePlus (FARO Technologies, Inc., Lake

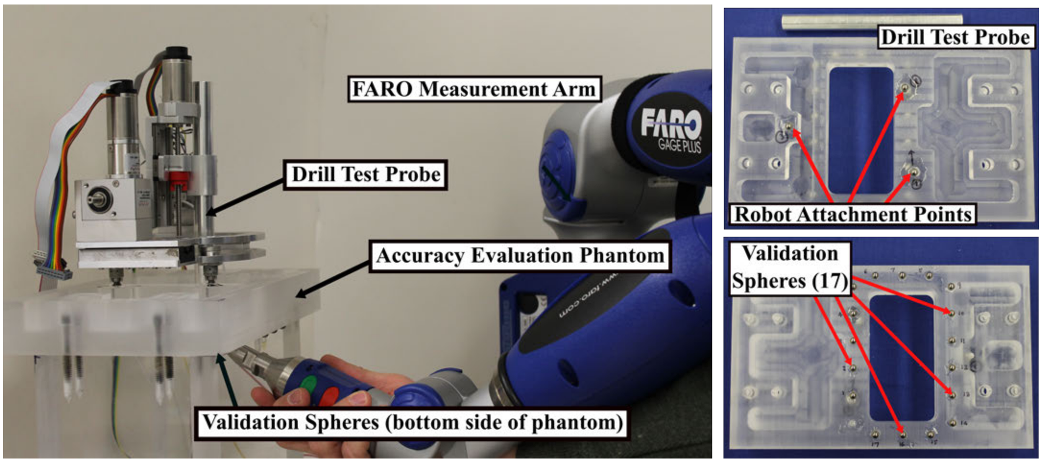

Figure 3.5: Experimental setup for free space accuracy evaluation. The acrylic phantom (right) contains attachment points for the robot on top and validation spheres for registering the experimental measurements to the CT target points on the bottom.

Mary, FL), which has an accuracy of 0.025 mm. The CMM was used to localize the seventeen validation spheres and measure the position of the drill probe at various positions. It was fixed to the same table as the phantom to minimize any relative motion.

Multiple scans of the phantom were taken using a portable CT scanner (xCAT ENT mobile scanner). Clinical CT scans of several patients were used to determine clinically relevant target points at which to test the positional accuracy of the system. Points on the bone surface, in regions close to the facial nerve, the vestibule, and the internal auditory canal (IAC) were chosen as test points. These points were then superimposed onto the scan of the phantom to serve as the “virtual targets” in the experiment. Additionally, each of the seventeen validation spheres and the three robot fiducial spheres were automatically localized in the CT scan of the phantom.

The robot was then mounted onto the test phantom, and the seventeen valida-

Table 3.1: Free space accuracy evaluation results - positional errors at several anatomical locations.

Location	**Mean Error (mm)**	**Std. Dev. (mm)**	**RMS (mm)**
Skull Surface	0.38	0.28	0.47
Facial Nerve	0.42	0.26	0.49
Vestibule	0.43	0.26	0.50
I.A.C.	0.42	0.24	0.48

tion spheres were localized using the CMM. The robot was programmed to move the drill probe to the eight virtual target locations (defined in the CT scan and transformed to the robot space using the three fiducial sphere locations) and the probe tip was measured at each of these target points with the CMM. After the data was acquired, a rigid transformation with least-squares error was calculated between the CMM coordinate system and the CT image coordinate system using the validation spheres [112]. Then the CMM measurements were transformed to the CT coordinate system and compared with the planned data points. The targeting error was then calculated. This error includes several sources of error in the system, including both image processing and physical robot error. This procedure was repeated for three scans of the phantom and each scan used a different set of target points. The measurements for each set of points was repeated three times. The robot was removed from the phantom, powered down, re-attached, and run-through its full initialization process each time. The results of these experiments are summarized in Table 3.1. The mean and root mean square (RMS) targeting error for all four regions were 0.50 mm or less.

3.4.3 Cadaver Temporal Bone Experiments

Experiments in cadaver temporal bones were then performed. The bones were formalin-fixed and previously frozen. Since the specimens used in these experiments are only partial temporal bones and the robot requires a larger surface area for attaching the positioning frame, the bones were cast in a hard urethane compound to provide enough space for the attachment. These experiments followed the surgical workflow outlined in Section 3.2 with one exception: the segmentations were performed in the scan acquired with the positioning frame attached (defined as intra-operative scan in Section 3.2) rather than the preoperative scan before attaching the positioning frame. A 5 mm diameter spherical, fluted drill burr was used in all trials. After the procedure was completed, a post-operative CT scan was acquired. The removed volume was segmented and the post-operative scan was registered to the pre-operative scan for evaluation of the planned versus milled volume borders. The border error was calculated by creating a mesh of each volume and computing the distance between the surfaces for each point on the planned volume surface. Additionally, the specimens were examined post-operatively by an experienced attending otologist or neurotologist to check for violation of critical anatomy.

Mastoidectomies were performed on four temporal bone cadaver specimens. A photograph of a bone after the experiment is shown in Figure 3.6. The size of the segmented volumes ranged from 3.01 cm^3 to 8.85 cm^3. The error along the border of the target cavity was calculated by determining the distance between nearest border/surface points on the pre-operative and post-operative segmentations after the

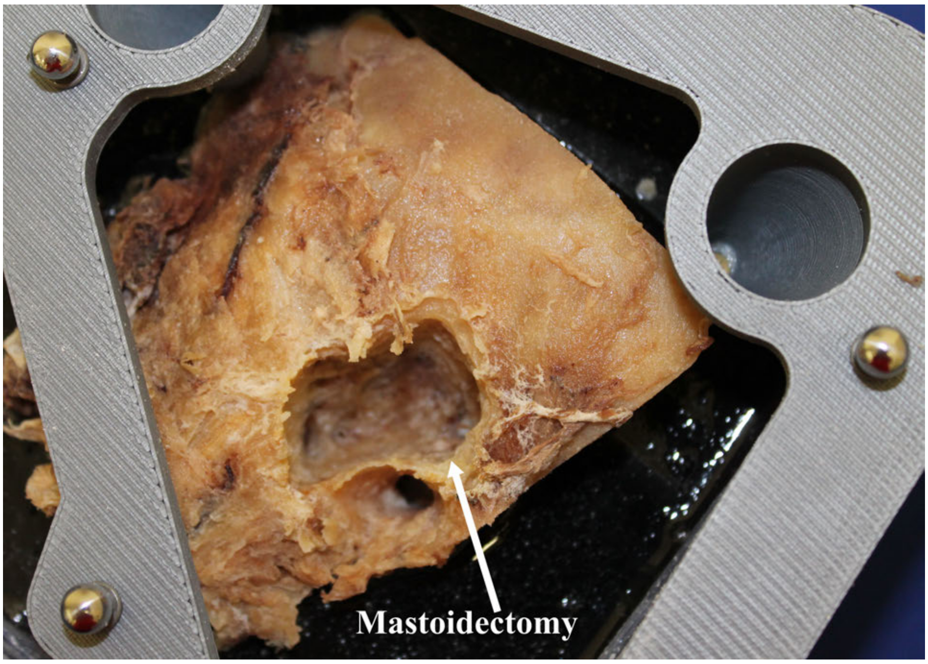

Figure 3.6: Temporal bone specimen after robotic mastoidectomy.

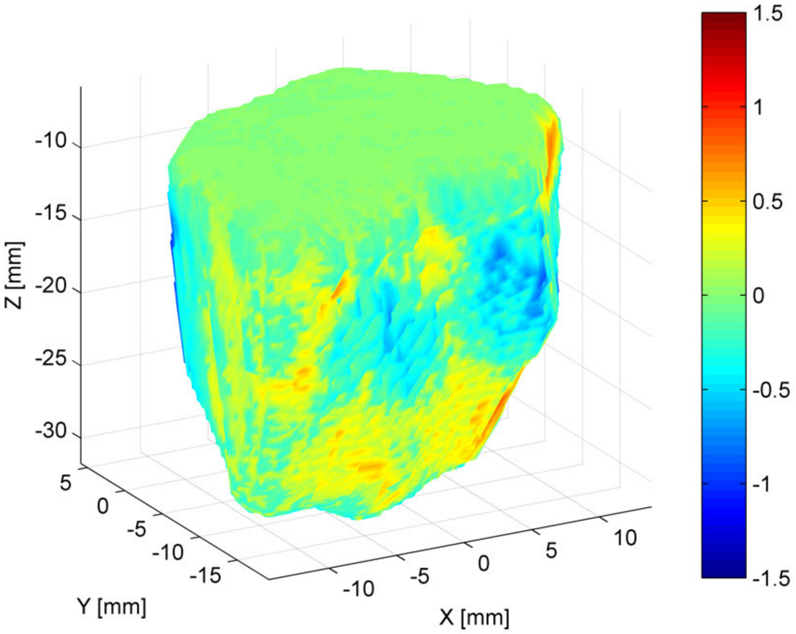

Figure 3.7: Surface error for a cadaver bone. The different colors along the surface represent the error between target and actual milled volumes. A negative error value indicates that the surface of the actual milled volume at that location was inside the planned volume.

Table 3.2: Border error for the removed volume of bone and distances between the removed volume and vital anatomic structures for cadaver experiments.

	Border Error (mm)		**Distance from Vital Nerves (mm)**	
	Mean	**Std. Dev.**	**Facial Nerve**	**Chorda Tympani**
Bone 1	0.73	0.39	2.39	3.48
Bone 2	0.44	0.31	1.71	2.08
Bone 3	0.19	0.13	0.89	2.36
Bone 4	0.18	0.17	1.61	2.90

two scans were registered. The mean border error for all trials was 0.39 mm. The error for a test specimen is shown in Figure 3.7. The border error results of the experiments are given in Table 3.2, along with the distances from the facial nerve and chorda tympani for each specimen. The first trial had higher error margins along the surface. A prior version of the positioning frame was used for this first trial; however, this was replaced with a stiffer version for later trials, which reduced the error. Post-operative examination of all specimens revealed no damage to the vital anatomy.

3.4.4 Discussion

This first set of experiments showed the feasibility and verified the proposed surgical workflow for mastoidectomy with a compact bone-attached robot. The system was shown to be sufficiently accurate for otologic surgery and the mastoidectomies were successfully performed. The time of procedure was not emphasized in these initial experimental trials; however, it is clear that improvements must be made to shorten the milling time. A key factor in the success of a robotic surgical system, in addition to improving patient safety and enabling surgeons to perform procedures that they would not otherwise be able to perform, is cost. A substantial cost associated with surgery is operating room time. So, if the overall time of procedure can be reduced to be at, or below, the current state of the art, a bone-attached robotic system for mastoidectomy would be more clinically viable. The experiments focused on simple mastoidectomies. However, the system could be especially beneficial if used for surgeries that require additional bone removal, such as the translabyrinthine approach to remove vestibular schwannoma (VS). Thus, improvements to the system to decrease operation time are particularly relevant for this surgery.

The primary limiting factor of the first prototype was actuator power. The piezoelectric actuators had some key benefits, including excellent positioning accuracy, integrated sensing, and sterilizability, but could not provide adequate driving force. The ability of the actuator to hold against a force was reduced when the drill was spinning at high frequencies, possibly related to the operating principle of the piezoelectric inchworm actuator, which cycles at high frequencies. Thus, lower drill spindle speeds had to be used, which required lower linear velocities to keep the forces on the drill tip low.

Design revisions should address the limitations described above as well as improve upon other factors. Improved visualization of the surgical site is necessary; the current design restricted the view of the drill within the mastoid at some positions. For the initial experiments, a single cutting burr was used throughout the procedure. When performing deeper mastoidectomies, it is sometimes necessary to change to a smaller cutting burr deep in the cavity. This change should be made easier for the surgeon to do intra-operatively with minimal delay. The next step in the experimental evaluation of this system, after necessary design revisions, is to perform experiments targeting deeper mastoidectomies on complete cadaver skulls and to use the full clinical workflow, including both the pre-operative and intra-operative CT scans.

3.5 System Improvements and Additional Experimentation

3.5.1 Second Robot Prototype

To address many of the lessons learned from the experimental trials with the first prototype, a second design was developed (see Figure 3.8). This robot also has 4 DOF (3 linear joints, 1 rotational joint). All actuators are driven by brushless DC motors (Maxon Precision Motor, Inc., Fall River, MA, USA). The linear joints are custom lead screw linear slides with improved rigidity compared to the prior version. A harmonic gear head (Harmonic Drive LLC, Peabody, MA, USA) is used with the rotational joint to provide high gear reduction in a small package with minimal (approximately zero) backlash. The visualization was improved by opening up the base of the robot at the front to provide a large open space for viewing the drill tip. This results in the positioning frame being positioned slightly posterior and superior compared to the previous version but the attachment screws are still in the region

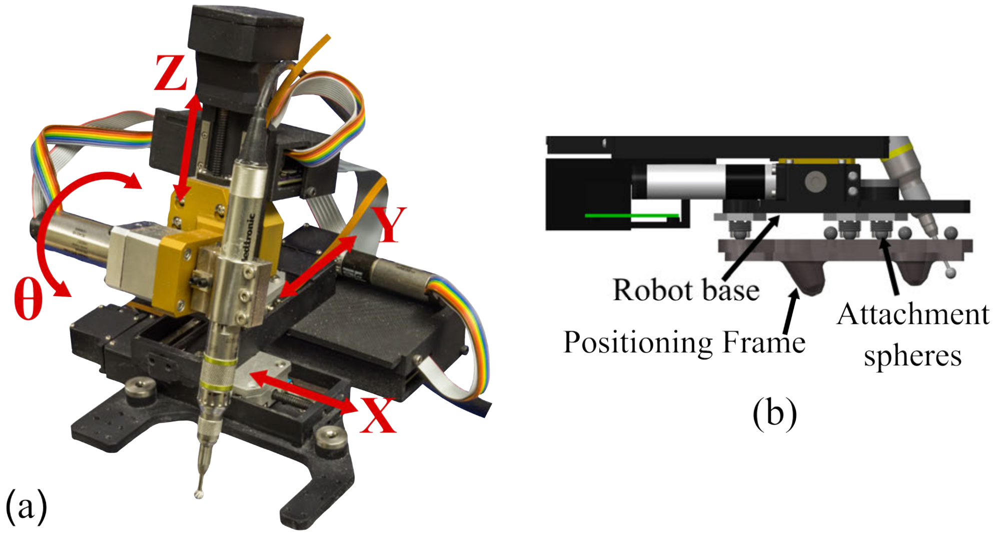

Figure 3.8: (a) Second prototype of bone-attached robot for mastoidectomy with the joint motion directions labeled. (b) Base of robot showing mounting to positioning frame.

of the skull near the temporal bone. All structural pieces are made from anodized aluminum or stainless steel to reduce corrosion.

3.5.2 Full Head Cadaver Experiments

A similar experimental procedure to the one described in Section 3.4.3 was followed to test the second robot prototype. However, these experiments were aimed at evaluating the robot for the translabyrinthine approach to VS so the target volume was considerably deeper than in the previous set of experiments. This volume included the mastoid and much of the labyrinth. The volume varied by specimen and included partial or full removal of all three semicircular canals, as specified by the surgeon to provide access to the IAC for VS removal. The planned volume extended to within approximately 1-1.5 mm from the IAC, depending on the specific anatomy of the specimen. Figure 3.9 shows a segmentation of the deeper target volume for these

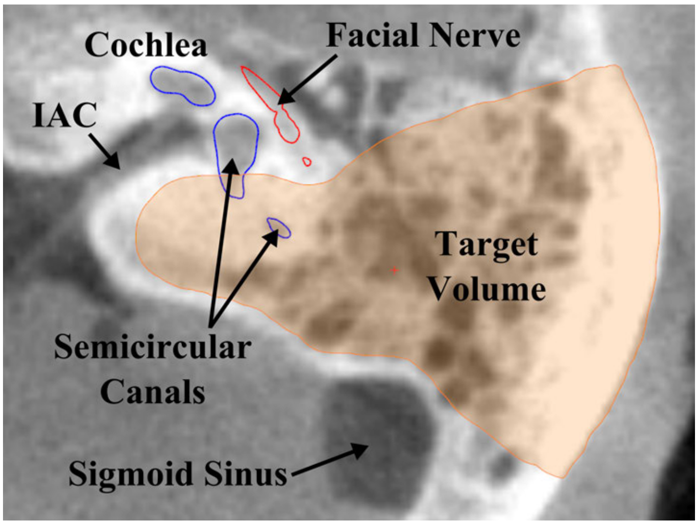

Figure 3.9: Axial slice of CT scan showing the manually segmented target volume of bone to be removed by the robot in the mastoid and labyrinthe. Additionally, the segmented middle and inner ear anatomy, including the external auditory canal, sigmoid sinus, ossicles, facial nerve, chorda tympani, semi-circular canals, cochlea, and internal auditory canal (IAC) are shown.

experiments, which was performed by an experienced attending neurotologist.

Additionally, to make these experiments more clinically realistic compared to the prior trials, the experiments were performed on fresh cadaver heads donated to Vanderbilt University Medical Center. The full clinical workflow described in Section 3.2 was followed, including both the pre- and intra-operative scans. A 5 mm burr was used at the start of all experimental trials and further milling was performed with a 3 mm burr in several of the trials. The 3 mm burr was used only in cases in which the smaller diameter enabled removal of substantial additional bone after milling with the 5 mm burr had reached its limit (i.e. the additional access permitted by the size of the 3 mm burr resulted in substantial bone removal deep within the cavity). During the experiment, milling was monitored and irrigation was administrated manually using

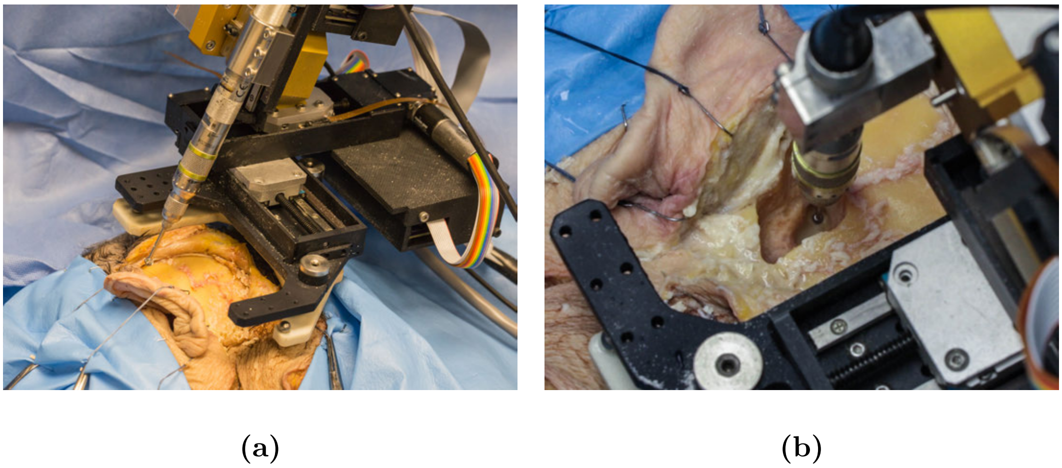
(a) (b)

Figure 3.10: (a) Photograph of robot mounted on a cadaver prior to an experiment and (b) photograph of drill within mastoid while removing the deeper portion of the volume.

a suction-irrigation hand piece. Figure 3.10 shows the robot and positioning frame mounted to a cadaver head prior to, and during, an experiment. The milling time was recorded for each experiment. This time value only represents the time spent by the robot milling bone and not the overall procedure time (see discussion below).

A post-operative CT scan was acquired after completion of each experiment to assess the quality of milling. To align the pre-operative and post-operative CT scans for verification of the accuracy of the milled cavity, titanium bone screws were inserted into the skull surrounding the surgical area and their locations were determined in both CT scans. These markers were not used for planning but rather served as the ground truth registration markers for aligning the planned milling with the actual milled volume. Given the location and number of markers, estimates of fiducial localization error for the scanner of 0.108 mm RMS [38], and locations of the target points, the registration error between the pre- and post-operative scans in the region of the milled volume was estimated to be 0.059 ± 0.004 mm RMS [112]. Given this accuracy of the fused images, registering pre- to post-operative CT scans is unlikely to contribute any clinically relevant error in assessing the milled cavity.

The volume of bone removed was segmented in the post-operative CT scan and compared with the pre-operative plan. The percentage of targeted bone removed was calculated as well as the error between the planned and milled cavity borders. Additionally, the milled cavity was examined under a microscope and the milled volumes and vital anatomy were reviewed in the post-operative CT scan by the surgeon.

A total of six trials were performed on five cadaver heads. For one trial, a post-operative CT scan was not acquired due to a malfunction of the CT scanner (the cadaver had to be returned for cremation prior to the scanner being repaired) so quantitative post-operative measurements are not available for this trial. One additional cadaver head was obtained and scanned; however, the procedure was not performed due to unusual anatomy. More specifically, this specimens sigmoid sinus was located more anteriorly than normal, which limited the access to the labyrinth through the window between the sigmoid sinus and the facial nerve. In clinical cases, the surgeon would decompress the sigmoid sinus to facilitate access to deeper anatomy; however, we did not decompress the blood vessel in this study and thus chose not to perform the milling on this specimen.

Table 3.3 provides data for each trial, including the targeted volume, percent of bone removed, mean surface error, and milling time. The targeted volume ranged in size from 5.03 to 11.67 cm^3. The milling time ranged from 32.7 to 57.0 min. The targeted volume impacts the milling time; however, these values are not directly proportional since the speed at which the robot moves is also affected by the bone

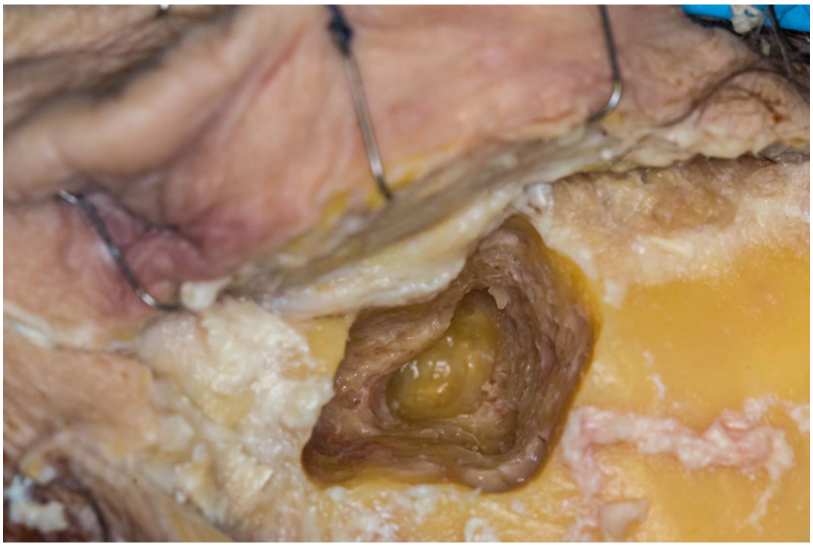

Figure 3.11: Photograph of milled cavity for cadaver head 5 (left side) after milling was completed.

density (i.e., the robot is programmed to move faster in more pneumatized areas) and ability to cut with more efficient drill angles. Additionally, iterative refinement of the robot trajectory planning algorithm throughout the study enabled faster bone removal in later trials.

For all experiments, the facial nerve and chorda tympani were preserved. Figure 3.11 shows a photograph of the milled cavity for cadaver head number 5 (left side). Figure 3.12 shows slices of the post-operative CT scans for cadaver head numbers 1 and 5 (right side). The outlines on the images indicate the planned milling cavity boundaries, which were registered to the post-operative CT scan. Once registered, the two boundaries were compared and the absolute value of the error at each point along the boundary surface was computed.

Table 3.4 provides the planned versus actual distances to various key anatomical structures. The distances shown in the table represent the closest distance be-

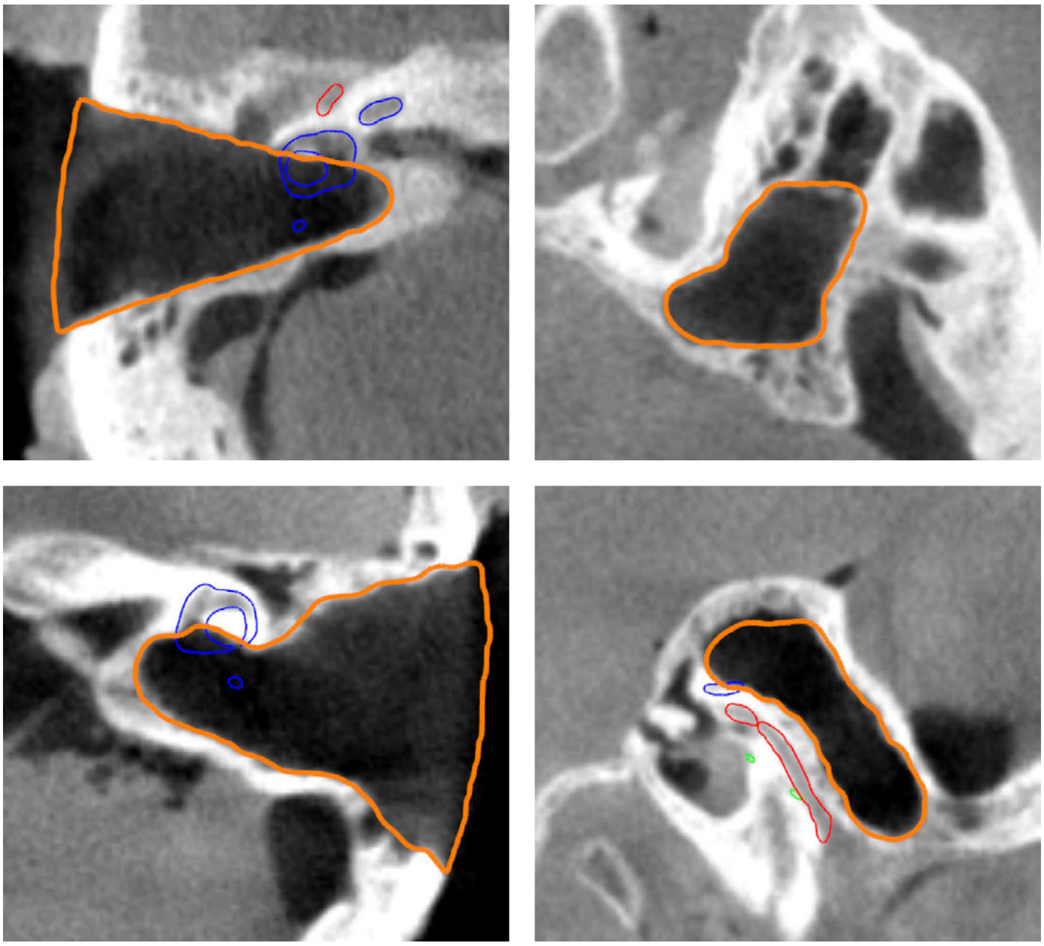

Figure 3.12: Slices of post-operative CT scan showing the bone removed by the robot and nearby vital anatomy for cadaver head 1 (top) and cadaver head 5 (right side) (bottom). The left slices are axial views and the right slices are sagittal views

Table 3.3: Results of full head cadaver milling experiments.

Specimen	Targeted Vol. (mm^3)	Percent Removed	RMS Surface Error (mm)[a]	Nerves Preserved?	Milling Time
1 (Left)	9.65	97.7	0.34	Yes	51 min, 11 sec
2 (Left)	5.03	95.2	0.65	Yes	41 min, 56 sec
3 (Right)[b]	10.22	–	0.44	Yes	57 min, 0 sec
4 (Left)	5.29	96.7	0.33	Yes	32 min, 40 sec
5 (Left)	9.17	96.0	0.35	Yes	45 min, 54 sec
5 (Right)	11.67	98.0	0.23	Yes	36 min, 49 sec

[a] Root mean square (RMS) error calculated from mean and standard deviation of the absolute value of error along surface of volume.

[b] No post-operative CT scan for this specimen (scanner malfunction; cadaver cremated before scanner was fixed).

tween any point in the planned/milled volume and any point along the surface of the nerve segmentation. This value was calculated by analyzing the vertices of a three-dimensional mesh of the planned (or removed) volume and the structure. The distances between each vertex of the two meshes were calculated and the minimum value was determined.

3.6 Discussion

The results from these experiments indicate that a compact image-guided robot attached rigidly to the skull has the potential to safely perform the bulk portion of bone removal for translabyrinthine access to the IAC for VS removal surgery. The accuracy achieved, in terms of both mean surface error and proximity to vital anatomy,

Table 3.4: Planned and actual proximity of milled cavity to various anatomical structures for full head cadaver trials.

Specimen No.	**Facial Nerve**		**Chorda Tympani**		**Ext. Canal**		**Tegmen**	
	Plan	**Actual**	**Plan**	**Actual**	**Plan**	**Actual**	**Plan**	**Actual**
1 (Left)	0.57	0.54	4.35	4.30	2.28	2.03	1.47	0.86
2 (Left)	0.67	0.81	3.32	3.62	1.70	1.75	1.07	1.39
3 (Right)[b]	0.44	–	3.29	–	4.86	–	0.34	–
4 (Left)	0.55	0.51	4.00	3.98	2.13	2.05	0.80	0.72
5 (Left)	0.49	0.48	1.85	1.90	1.99	2.05	0.46	0.52
5 (Right)	1.11	1.34	2.10	2.05	2.05	2.01	0.56	0.54

[a] The closest distance between any point in the planned/milled volume and any point along the surface of the structure.

[b] No post-operative CT scan for this specimen (scanner malfunction; cadaver cremated before scanner was fixed).

i.e. difference between planned and actual distance to the facial nerve, is within the required range for this procedure (see Table 3.4). The exact distance between the milled cavity and various anatomical structures will vary case-by-case according to the required resection volume for access and removal of the tumor. Since the robotic system can use pre-operative imaging to know precisely where the vital anatomy is located, anatomy does not have to be closely approached for identification purposes, potentially enabling larger margins between the removed volume and structures.

The milling times in these experiments are lower than that typically achieved manually for translabyrinthine access to the IAC in the operating room (OR) today, even accounting for the additional steps required for the robotic approach. We estimate that the steps in the surgical workflow of the robot-assisted approach that are not part of the conventional approach would require an additional 22 to 36 minutes depending on the particular patient anatomy. These times are estimated based on our experience in this study as well as experience with a prior clinical study using a bone-attached micro-stereotactic frame for minimally invasive CI that follows many of the same workflow steps [75]. However, it is important to note that translation of this approach to clinical use would present additional challenges and, therefore, a fair comparison with current manual bone milling duration in the OR for this procedure is not yet possible. The experiments described in this chapter were performed in the laboratory by the research group that developed the system so an additional learning curve would be present for new users, which is not accounted for in this data. Also, further bone removal to gain access to the IAC using a smaller diamond burr and surgical pick is required and the time of this component of the surgery, given the access provided by the volume of bone removed by the robot, is unknown. Further experimentation, in which the surgeon completes the opening of the IAC, is necessary to evaluate the timing and difficulty of this task. At the least, these preliminary results show that a compact, bone-attached robot can efficiently perform a substantial component of the bone removal.

As described in the results section, one of the cadaver heads was scanned but the milling was not ultimately performed due to the anterior location of the specimens sigmoid sinus. It is currently unknown what percentage of the general population (or the subset requiring VS removal surgery) has similar anatomy that restrict the robot from performing the procedure without decompressing the sigmoid sinus. In the future, with a modification of the robot planning protocol, it would be possible to account for these cases. The robot could first mill the volume initially accessible. Then it could be removed, the surgeon could decompress the sigmoid sinus, and then the robot could be reattached to finish the milling.

We encountered several implementation challenges through the course of these experiments and have identified various solutions to improve the ease-of-use of the system moving forward towards clinical translation. For example, segmentation of the target volume of bone to be removed is tedious using the current approach because the surgeon must manually outline the bone in 2D slices of the CT scan. This process is both time consuming and geometrically disorienting because the surgeon must make mental estimates of how close a 2D segmented slice is to a more superior and/or inferior slice. To make this component of the workflow simpler and more efficient, we are working on automated processes [91], in which a resection volume for robotic translabyrinthine IAC access is computed and used as a starting point for the surgeon who could then manually adjust where necessary.

Other planned system improvements include: an improved surgeon interface and real-time views of the drill tip location in the pre-operative CT, optimized selection of burr size to mill as much of the cavity as possible while minimizing the number of burr changes, and redundant safety features. These redundant safety features are critical to ensure that any system malfunction is identified immediately to avoid a major error that could cause injury to the patient. This can be accomplished by incorporating a variety of additional sensing modalities and integrating these into the robot control system. An optical tracking system could be used to continually monitor the position of the drill tip and compare the tracked position with the position calculated from the individual joint sensors and robot kinematics. Additionally, facial nerve monitoring could be integrated with the robot controller to detect if the drill tip is closer to the nerve than planned [3]. Finally, the drill tip position can be verified using force sensing and the force-density relationship estimated from the pre-operative CT [127].

Chapter 4

Generating Safety Margins for Robotic Surgery Using Probabilistic Error Modeling

The work presented in the next two chapters focuses on improving the safety and efficiency of robotic mastoidectomy through the development of novel planning methods. In this chapter, an algorithm is presented to generate patient-specific safety margins around vital anatomic structures using error models of the image-guided robotic system.

4.1 Background and Related Work

As discussed in the Introduction, a challenge of otologic surgery is the presence of vital anatomy within the surgical field. As a result, the accuracy requirement of an image-guided system is higher for otologic surgery than for many other surgical specialties and the consequences of system error can be severe. The purpose of the work in this chapter is to provide an additional safety mechanism in the planning stage of robotic surgery by modeling potential errors of the system near vital anatomy. The models, which are spatially varying stochastic distributions, are used to produce patient-

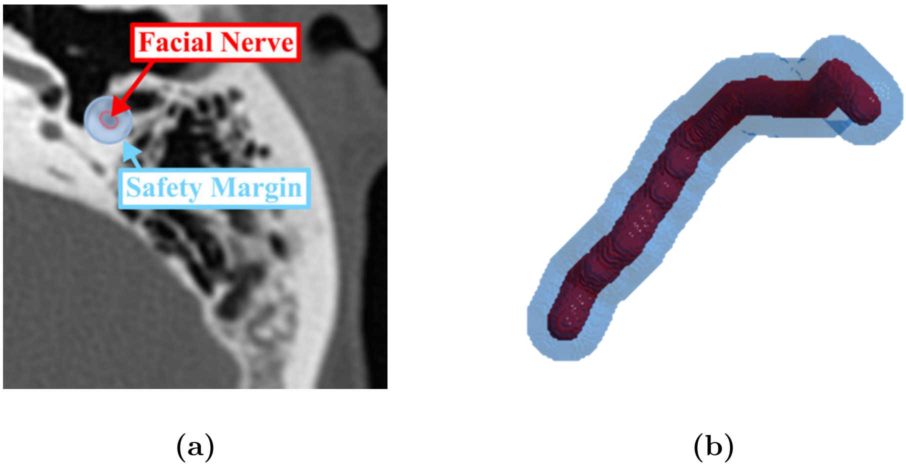

(a) (b)

Figure 4.1: (a) Computed tomography (CT) scan showing the facial nerve and uniform safety margin, and (b) a 3D rendering of the facial nerve with uniform safety margin surrounding it.

specific, statistically-driven safety margins around vital structures. The algorithm is tested specifically for robotic mastoidectomy but is applicable to any surgery in which a robot is working in close proximity to vital anatomy that must be preserved.

Prior work towards developing statistically-informed planning methods of this type has incorporated target registration error (TRE) at the tip of an image-guided cutting tool for linear [94] and three-dimensional trajectories [50, 110, 111]. However, these algorithms have not directly accounted for the physical hardware error in the surgical system or distortion in the images used to plan the procedure. In robotic surgery, kinematic error can result in inaccurate positioning of the surgical tool. Additionally, when a robot interacts with tissue, the end effector deflects away from the desired position. These errors should be modeled in order to determine an appropriate probability of deviation from the planned path and into vital anatomy. A conservative approach to incorporating system errors into planning is to place a

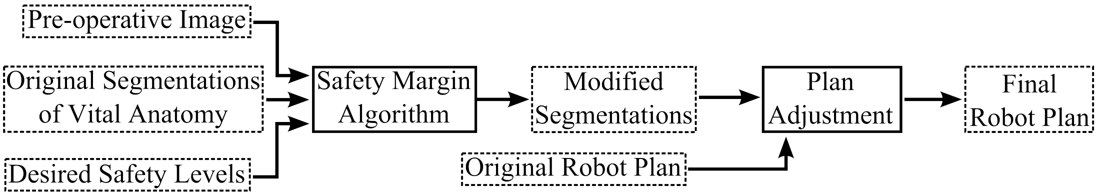

Figure 4.2: Flow chart of surgical planning process including the proposed safety margin algorithm. In this figure, processes are outlined in solid lines and data are outlined in dashed lines.

uniform safety margin around all vital anatomical structures with a thickness related to the maximum possible error of the system (see Figure 4.1). This may work in some cases but if the robot must operate in close proximity to vital anatomy, excessively large margins may limit the usefulness of the system. A better approach, as initially outlined in [111], is to use a safety margin of varying thickness based on the error probability distributions at points near the structure. This work extends the method of [111] (which considered only registration error) to account for uncertainties arising from physical robot attachment, kinematic errors, and deflection during surgery, as well as geometric uncertainty in the image. The algorithm is applied to the bone-attached robot for mastoidectomy described in Chapter 3.5 to generate safety margins around several vital structures.

4.2 Algorithm Overview

The proposed safety algorithm is applied during the surgical planning phase. Safety margins are generated around vital anatomy using error models of the image-guided robotic system, which are then used to alter the planned robot path or target volume (see Figure 4.2). The inputs to the algorithm are the pre-operative images, segmentations of any vital structures that must be avoided during surgery (sensitive anatomical features such as the facial nerve), and a desired preservation probability for each vital structure (e.g. the surgeon can specify, “I want to be 99.9% sure that the facial nerve is not damaged”). The output safety margins are unique to each vital structure and depend on the structure’s position relative to the robot as well as the desired preservation rate. The safety margin thicknesses vary spatially, and combined with the underlying structure, define the set of points that must not be *targeted* by the robot to ensure that the underlying structure is preserved at the rate specified pre-operatively. Thus, any portion of the original planned path or volume that overlaps with the safety margins is removed from the final plan.

Starting with the original segmentation of the vital structure, the algorithm iteratively builds the safety margin until it is large enough to ensure the vital structure’s desired preservation probability. The image, vital structure, and safety margin are all considered as voxelized, i.e. a volumetric discretization, and the algorithm builds the safety margin by adding to it in units of voxels (the image can be down or up sampled as necessary to adjust voxel resolution). For each iteration of the algorithm, the probability of preservation of the vital structure with the current safety margin is first estimated using a Monte Carlo simulation. This simulation considers the shell of all voxels surrounding the safety margin as targeted points. The actual targeted volume of bone to be removed does not necessarily include these points; however, since the safety margin is generated independent of the target volume, all of the surrounding points are included as targets in the simulation. If the preservation probability

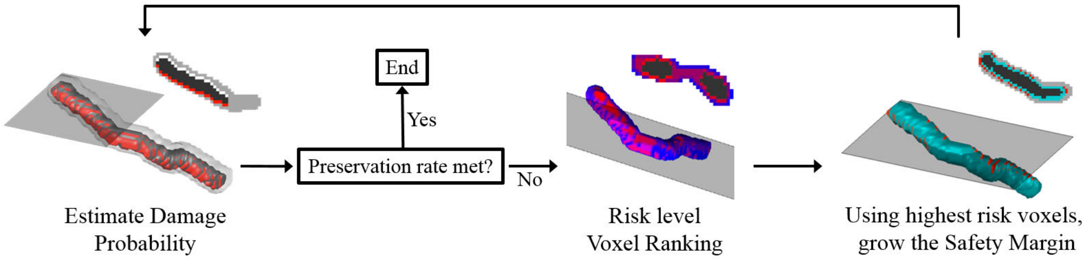

Figure 4.3: A schematic of the proposed safety algorithm. For each iteration, the probability of preserving the vital structure is calculated, given the current safety margin. If this probability is lower than the specified probability, then the highest risk voxels are added to the safety margin. The calculation is repeated until the calculated preservation rate is greater than the specified rate.

predicted by the simulation is lower than the desired probability, the safety margin's volume must be increased. The surrounding voxels are then ranked according to the likelihood that the underlying vital structure would be damaged if they were included in the planned path or volume. The highest risk voxels are then added to the safety margin. This process is repeated by analyzing a new shell of voxels surrounding the updated safety margin (see Figure 4.3). Once the vital structure's simulated preservation rate is at or above the desired level, the algorithm stops and outputs the final safety margin. Since the errors used in estimating the probability of damage are spatially varying and anisotropic, the margins vary in thickness and are generally non-uniform.

The Monte Carlo simulation to estimate the preservation rate at the beginning of each iteration of the algorithm incorporates different potential sources of system error. The various error sources are modeled as probability distributions, and for a given voxel in the shell surrounding the vital structure and safety margin, an error value from each probability distribution is sampled. These errors are combined to form an overall relative positioning error at the drill tip for the point under consideration. If the positioning error at *any* point in the shell would cause the drill to hit the underlying vital structure, the structure is considered to be damaged for that calculation. The calculation is repeated N times with new values sampled from the error distributions for each calculation. The percentage of sample calculations in which the structure is not violated is the preservation rate for the current safety margin. When ranking the highest risk voxels to determine which ones to add to the safety margin, each voxel is subjected to a separate Monte Carlo simulation to determine the probability of damage to the vital structure if that particular voxel were to be targeted.

4.2.1 Error Computation

In each calculation of the Monte Carlo simulation, the various error sources are combined to estimate the total system error at a given point. The error sources considered in the calculation will depend on the specific robotic system; however, in general, this will include image distortion, image registration, robot positioning, and robot deflection errors. The error calculation follows the flow of information in the planning and execution of the procedure and each step that may cause error relative to the original plan should be considered (see Figure 4.4). This section describes the general approach of the error calculation used in the algorithm; a detailed explanation of the various error sources and the calculation of the error distributions for a bone-attached

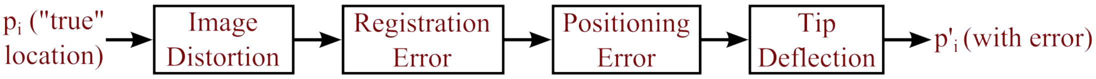

Figure 4.4: Schematic of calculation of positioning error of an individual point. The calculation starts with the "true" location of the point, $\mathbf{p}_i$, and the various sources of error in the system are added to determine the location used in the simulation. In this work, imaging, registration, robot positioning and deflection errors are considered.

robot for mastoidectomy are provided in Section 4.3.

The error calculation for a given point, $\mathbf{p}_i$, begins with the error associated with image acquisition and processing. This imaging error arises from geometric distortion and inaccurate registration. Targeting based on pre- or intra-operative imaging is fundamentally limited by the geometric accuracy of the image. Inaccuracy leads to distortion, or non-rigid mapping, of points in the image relative to their true position in physical space. While any non-rigid distortion is, in principle, possible, it is assumed here that components of second or higher degree are negligible. Therefore, the transformation between physical space and the image is assumed to be strictly affine, i.e. $\mathbf{y} = T\mathbf{x} + \mathbf{t}$, where $\mathbf{x}$ is a point in physical space and $\mathbf{y}$ is that point in the image after distortion. This transformation, T, consists of a rigid and non-rigid component, such that $T = AR$. The non-rigid component A represents image distortion and the rigid component R represents the registration between image and physical space.

The image distortion could be incorporated into the error calculation in two different ways. First, if no prior knowledge of the distortion of a particular scanner is known, a random characteristic transformation for the scanner, A_c, can be generated for each calculation of the Monte Carlo simulation based on known estimates of other similar scanners (for example, see Appendix A of [38] for results from testing several commercially available CT scanners). The distorted point location in image space, ${}^{Im}\mathbf{p}_i^*$, can then be calculated using A_c as

$$ {}^{Im}\mathbf{p}_i^* = A_c \, {}^{Im}\tilde{\mathbf{p}}_i, \tag{4.1} $$

where ${}^{Im}\tilde{\mathbf{p}}_i$ is the true location of the point relative to the centroid of the fiducial markers expressed in the image coordinate system.

Alternatively, if we have an estimate of the characteristic transformation for a particular scanner ($\widehat{A}_c$), the distorted image can be rectified by multiplying points in the image by $\widehat{A}_c^{-1}$. The error associated with image distortion is then reduced to the uncertainty in $\widehat{A}_c$. This uncertainty arises from differences in calculation of a scanner's characteristic transformation using different sample images as reference (see Section 4.3.1 for more details). The uncertainty is represented by probability distributions for each of the elements of A_c. These distributions are sampled to construct a sample distortion matrix, A_i, for each calculation in the simulation and the distorted point location is calculated by

$$ {}^{Im}\mathbf{p}_i^* = \widehat{A}_c^{-1} \, A_i \, {}^{Im}\tilde{\mathbf{p}}_i. \tag{4.2} $$

The distorted point location, ${}^{Im}\mathbf{p}_i^*$, is then converted to the robot base coordinate system (Frame $\{0\}$) by applying a rigid transformation determined by registering the image to physical space:

$$ {}^{0}\mathbf{p}_i = {}^{0}R_{Im} \, {}^{Im}\mathbf{p}_i^* + {}^{0}\mathbf{t}_{Im} + \mathbf{e}_{i,reg}. \tag{4.3} $$

where ${}^{0}R_{Im}$ and ${}^{0}\mathbf{t}_{Im}$ represent the rigid transformation between the image and the robot base coordinate frames, and $\mathbf{e}_{i,reg}$ represents the registration error. Registration error can be estimated based on the method of registration and image quality. For the case of point-based registration, for example, it is possible to determine the distribution of TRE at a given point based on the locations of the fiducial markers and associated distributions of fiducial localization error (FLE) [24]. If closed-form equations are not available to determine registration error distributions, the registration error can be computed for each Monte Carlo calculation by performing a simulated registration.

Next, the robot positioning errors are included in the error computation. The superscript indicating the frame of reference is dropped for brevity from this point forward and it is assumed that all positions are in the robot's base coordinate frame (Frame $\{0\}$). A nominal corresponding set of joint values, $\mathbf{q}_i$, is calculated using the inverse kinematics of the robot:

$$\mathbf{q}_i = \mathrm{InvKin}({}^{0}\mathbf{p}_i, \mathbf{G}). \tag{4.4}$$

where $\mathbf{G}$ is the robot geometry. A new set of joint values, $\mathbf{q}_i^*$, which includes additional joint positioning errors (e.g. joint backlash, sensor error, etc.) is then calculated:

$$\mathbf{q}_i^* = \mathbf{q}_i + \mathbf{e}_q, \tag{4.5}$$

where $\mathbf{e}_q$ is a sum of the various contributions to the joint positioning errors.

Uncertainty in the geometric model of the robot is also considered in the error calculation. Prior to using any surgical robot, a geometric calibration will be performed to determine link lengths, joint axes directions, etc. used in such a model. This calibration will inherently be limited by the calibration measurement method and the limited number of measurements made, among other factors. An estimate of the calibration uncertainty can be made by analyzing these limitations and/or performing many calibrations to determine the variance. To include this error source in the Monte Carlo simulation, the geometric calibration errors are also selected randomly from probability distributions and combined with the calibrated geometry data to determine new values that include error. Using this data, along with the joint values calculated above, the associated drill tip position, including geometric calibration error, $\mathbf{p}_i^*$, is calculated as

$$\mathbf{p}_i^* = \mathrm{FwdKin}(\mathbf{q}_i^*, \mathbf{G}^*), \tag{4.6}$$

where $\mathbf{G}^*$ represents the robot geometry including the sampled error values.

The last component of positioning error included in this model relates to uncertainty in control, which comes from hardware limitations (e.g. controller positioning errors, and/or asynchronous control of the individual joints) and interpolation between target positions. This error, $\mathbf{e}_{p,ctrl}$, which can be estimated experimentally by monitoring the positioning error of the system over time, is simply added to $\mathbf{p}_i^*$.

Finally, errors related to robot deflection are included in the error computation. The estimated deflection is determined by the expected forces at the end-effector of the robot and the stiffness of the robot. Since the robot compliance matrix is pose dependent and a function of the robot Jacobian,, the joint values with sampled error, $\mathbf{q}_i^*$, and robot geometry with sampled calibration error, $\mathbf{G}^*$, are used for the calculation of the robot Jacobian. The compliance matrix, C, is not limited to compliance of the robot joints. Additional off-axis structural compliance can be included (e.g. using the "virtual joints" method described iy [2]) and for the case of bone-mounted robots, the compliance of the attachment can also be included [66, 67]. The tip deflection is then computed using C and a sampled value from a range of forces expected during the procedure, $\mathbf{f}_i$,

$$\Delta\mathbf{p}_i = C\mathbf{f}_i. \tag{4.7}$$

The drill tip position including error, $\mathbf{p}'_i$, is then calculated from the kinematic error and tip deflection:

$$\mathbf{p}'_i = \mathbf{p}^*_i + \Delta\mathbf{p}_{tip}. \tag{4.8}$$

The calculation is repeated many times in the simulation, with the error distributions re-sampled for each calculation. It is also important to note that some of the error sources are coupled among target points, e.g. a rigid registration will apply the same transformation to all points and robot calibration error will affect the kinematic model that is used for all points. For this type of error, a single value is sampled from the error distribution and applied to each target point for that particular Monte Carlo calculation. For error sources that are considered independent among target point locations, (e.g. joint backlash error and forces at the drill tip), a unique value is sampled from the error distributions for each point.

4.3 Error Modeling for Mastoidectomy with a Bone-Attached Robot

This section provides a description of the error sources used in the proposed safety margin algorithm as applied to the bone-attached robot for mastoidectomy presented in Chapter 3.5. Some of the errors considered below are specific to this particular robot; however, others (e.g. image distortion) can be used for any image-guided robot. All numeric error distribution values used in subsequent simulations are listed in Table 4.1 at the end of this section.

4.3.1 Image Distortion

As described in the previous section, image distortion error is the non-rigid component of the transformation, T, between image and physical space. Thus, to calculate the distortion of a particular scanner, it is necessary to first determine T and then calculate the non-rigid component of T. CT is the primary modality used in otologic surgery so a method was developed to quantify the geometric distortion in CT scanners (see Appendix A of [38] for details; the data for the Xoran xCAT ENT scanner is used in this model). Briefly, a precise phantom with titanium spheres embedded at known locations (Figure 4.5) was scanned multiple times. The locations of the titanium spheres in the image ($\mathbf{Y}$) were determined for each scan and the points in physical space ($\mathbf{X}$) are known from the phantom dimensions. Both sets of points were de-meaned to obtain $\tilde{\mathbf{X}}$ and $\tilde{\mathbf{Y}}$, respectively, and the affine transformation, T, that

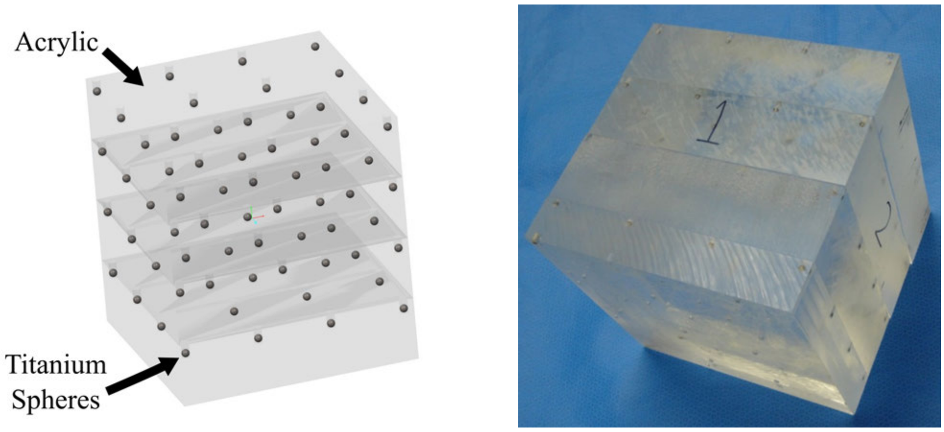

(a) **(b)**

Figure 4.5: (a) Schematic and (b) photo of custom phantom used to quantify the geometric accuracy of CT scanners.

maps $\tilde{\mathbf{X}}$ to $\tilde{\mathbf{Y}}$ was calculated in a least-squares sense. This transformation includes the image distortion as well as the rigid rotation between the image and physical space [112].

To isolate the distortion, T is factored into rigid and non-rigid components using the polar decomposition, $T = AR$, where A is a positive-semidefinite Hermitian matrix and R is a rotation matrix ($R^tR = I$). Figure 4.6 provides a schematic of this decomposition. The registration errors associated with calculating R are covered in the next section. A represents the stretching, or distortion, of the image and is given by

$$A = U\Lambda U^t, \tag{4.9}$$

where the columns of U are the eigenvectors of TT^t and Λ is a diagonal matrix of the singular values of T. A is calculated for each scan acquired of the geometric phantom. The mean of the A matrices for all scans is the characteristic transformation of the

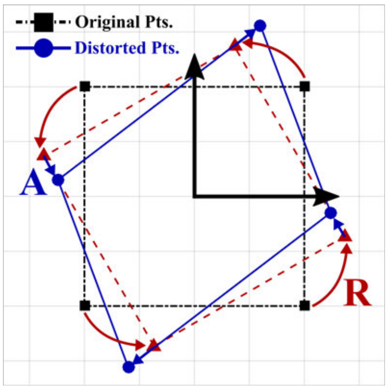

Figure 4.6: Two-dimensional schematic of polar decomposition of scanner affine transformation into a rigid rotation, R, and a distortion, A

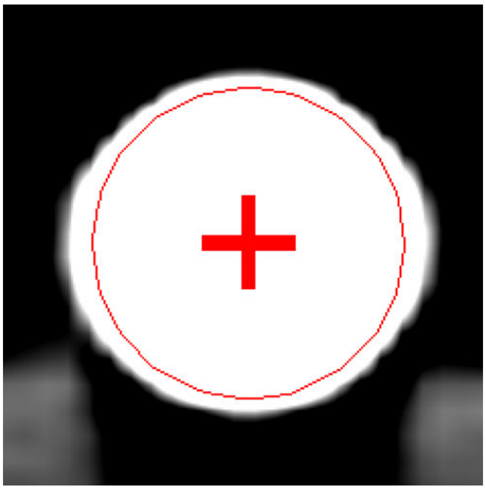

Figure 4.7: Titanium fiducial marker localized in CT scan.

scanner, A_c. The variance in elements of A are used in the error calculation according to Equations 4.1 or 4.2.

4.3.2 Registration Error

Point-based registration is used to align the bone-attached robot to the image data. The TRE distributions at a given target point associated with this registration can be estimated from the FLE distributions [24]. Figure 4.7 shows a fiducial marker localized in a CT scan. As was done in [111], a value from the TRE distribution for a particular point is sampled to determine the error associated with a "mis-registration" (i.e. a registration containing error due to imperfect fiducial localization). This error is added to the transformation from image to physical space.

Knowledge of the FLE and the nominal fiducial marker locations with respect to the target positions is required to calculate the TRE. The FLE was computed using the same scans with the phantom described in Section 4.3.1 (see Figure 4.5). First, for each image, the de-meaned points in image space were "rectified", $\mathbf{Y}_r = A_c^{-1}\tilde{\mathbf{Y}}$. Next, a rigid point-based registration of $\mathbf{Y}_r$ to the de-meaned phantom model $\tilde{\mathbf{X}}$ was performed and the fiducial registration error (FRE) for the registration was calculated. Finally, Equation 8.25 from [113] was used to estimate the Root Mean Squared (RMS) FLE from the FRE.

Prior work by Kobler et al. characterized FLE for various sphere localization algorithms, marker materials, and image interpolation approaches [64]. The values obtained in that work for titanium spheres using the cross correlation and least squares algorithms with image interpolation factors greater than 1 yielded FLE values similar to the value calculated for the Xoran xCAT ENT scanner used in this application. The data in [64] can be used as a reference to estimate FLE if the value for a particular setup is unknown.

4.3.3 Robot Kinematic Errors

Robot error analysis and modeling has been a significant area of research for many years (e.g. [124]) and has been studied within the context of medical robotics [90,92]. Thus, the various sources of kinematic error (joint positioning and geometric uncertainty) are well understood and can be applied to the robotic system analyzed here. More specifically, the joint positioning errors considered in the model for this robot are: (1) joint transmission backlash, (2) joint initialization inaccuracies, (3) joint sensing discretization, and (4) asynchronous control of joint positions. The joint transmission errors were calculated based on hardware specifications and transmission ratios. The linear joints have planetary gearboxes which result in slight backlash, although it is mitigated by a high reduction ratio of the lead screw. This error is modeled as a discrete distribution with two possible values (plus or minus the backlash value from the manufacturer's specifications, multiplied by the gear ratio). The harmonic gearbox used in the rotational joint has negligible backlash, but the compliance of the flexible spline factors into the joint stiffness value.

Inconsistent joint initialization (or homing) each time the robot is powered on results in a slightly different baseline from which all joint values are then calculated. This error was quantified by performing the initialization process, in which the joints are run to their end stops and zeroed, several times and analyzing the differences in zero positions. The sensor discretization error is a function of the encoder resolution and transmission gear ratios. The discretization error is modeled as a uniform distribution with bounds of plus or minus half of the joint discretization value. Given the high gear reduction ratios used, this error is low.

Finally, since the controller cannot bring each joint to its desired position at *exactly* the same time, there is some error associated with this asynchronous joint movement. To quantify this, the maximum allowed positioning error defined in the control software (system shuts down if this is exceeded) is considered. This maximum error is then used to bound a random, uniform error distribution.

The geometric errors come from imperfect calibration of various parameters (e.g. link lengths, joint motion axes directions). To determine the geometric calibration errors, the full calibration procedure was performed ten times and the results for each model parameter were analyzed. This procedure involves moving the robot to a series of points, measuring these locations with a coordinate measurement machine (CMM), and fitting the data to the kinematic model of the robot. The variance in the resulting calibrated parameter values were used to select appropriate error distributions for each value in the kinematic model. Linear dimension errors (e.g. link lengths and position vectors between relevant coordinate frames) are simply added to the nominal value when calculating the error. Joint axis unit vectors and coordinate transformation errors are incorporated by multiplying the nominal value by a rotation matrix that represents a small rigid rotation.

4.3.4 Robot Compliance

Two components of compliance considered in this analysis: compliance of the robot (joints and structural elements) and compliance of the attachment to the patient's skull at the interface between the bone and the anchoring screws. A common method for computing the compliance of a robot is to assume quasi-static loading and infinitely stiff links relative to the joints [122]. This enables a task space compliance matrix for the entire robot to be computed based on the individual joint stiffness values (acting about the joint motion axes) and the configuration of the robot.

$$C = J\chi^{-1}J^{t}, \tag{4.10}$$

where $\chi = \mathrm{Diag}([k_1, k_2, ..., k_n])$ represents the joint stiffness matrix, J is the robot Jacobian, and k_j is the stiffness value along the motion of the j^{th} joint (q_j). k_j is a linear stiffness coefficient for prismatic joints and torsional stiffness coefficient for rotational joints. The assumption of infinitely stiff structural members connecting the joints depends on the size and material selected for the links compared to the expected loads. This assumption is valid for the robot considered here as the robot is constructed from aluminum and stainless steel and the links were sized sufficiently large for the range of forces at the drill tip.

However, additional compliance can exist at the link-joint interfaces in off-axis directions, i.e. directions other than the joint motion axis. For example, a rotational joint can have some angular compliance perpendicular to the rotating shaft axis and/or linear compliance in one or more directions. Any additional compliance must be considered in an accurate model. Thus, experiments were performed on each joint of the robot to measure compliance in all directions. Forces and moments were applied in each orthogonal direction and the associated linear or angular deflection was measured (see Appendix A for more details.). The data was then analyzed to de-

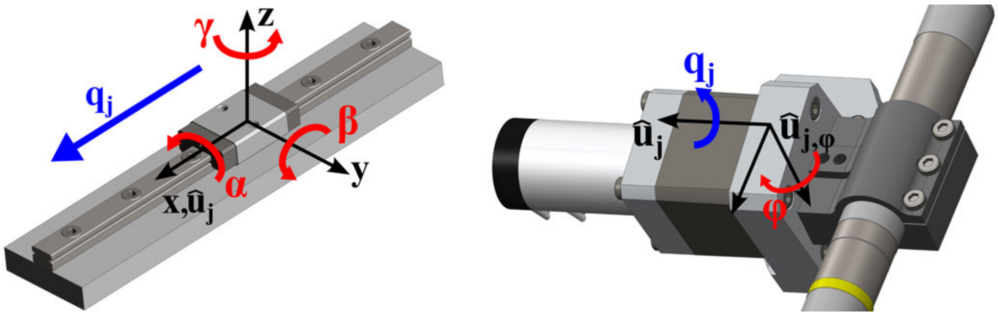

(a) **(b)**

Figure 4.8: An illustration of the off-axis deflection directions of robot joints considered in this analysis. These are in addition to compliance about/along each joint axis, which were also modeled. (a) For linear joints, angular deflections resulting from moments in all three directions were considered. (b) For rotational joints, angular deflection resulting from a moment perpendicular to the joint axis was considered.

termine which additional displacements must be included in the model and a stiffness coefficient was calculated for each direction of motion. The prismatic joints for this robot have angular compliance in all three directions but negligible linear compliance in the off-axis directions. The rotational joint has angular compliance perpendicular to the joint axis (specifically, about the vector that is orthogonal to the joint axis and the drill spindle axis). Figure 4.8 shows the directions of these relevant off-axis compliances for the prismatic and rotational joints of the robot. The stiffness coefficients along the joint motion directions (k_i) were also measured in this manner. Note that both axis and off-axis stiffness values are assumed here to be constant throughout the range of motion of the joint.

To account for the off-axis stiffness and to generate a compliance matrix similar to Equation 4.10, the kinematic model is augmented with additional "virtual joints" which represent motion about the additional directions of compliance that must be considered [2]. When determining the position of the drill tip in the kinematic model, these additional joint values are set to zero; however, their contribution to the robot Jacobian enables them to contribute to the total robot compliance matrix. The full sets of joint displacements for the prismatic and rotational joints are given by

$$\mathbf{q}_j(\text{Prism}) = [q_j,\, \alpha_j,\, \beta_j,\, \gamma_j]^t, \tag{4.11}$$

$$\mathbf{q}_j(\text{Rot}) = [q_j,\, \phi_j]^t, \tag{4.12}$$

where α_j, β_j, and γ_j are the angular compliance displacements associated with the x-, y-, and z-axes of the prismatic joint coordinate frame (see Figure 4.8). ϕ_j is the angular compliance displacement about the axis perpendicular to the rotational joint axis and the drill spindle axis ($\hat{\mathbf{u}}_{j,\phi}$). The columns of the linear velocity Jacobian for the full sets of prismatic and rotational joint displacements are

$$J_j(\text{Prism}) = [\hat{\mathbf{u}}_j \,|\, \hat{\mathbf{x}}_j \times \mathbf{r}_j \,|\, \hat{\mathbf{y}}_j \times \mathbf{r}_j \,|\, \hat{\mathbf{z}}_j \times \mathbf{r}_j], \tag{4.13}$$

$$J_j(\text{Rot}) = [\hat{\mathbf{u}}_j \times \mathbf{r}_j \,|\, \hat{\mathbf{u}}_{j,\phi} \times \mathbf{r}_j], \tag{4.14}$$

where $\hat{\mathbf{u}}_j$ is the j^{th} joint axis unit vector, $\mathbf{r}_j$ is the position vector of the drill tip relative to the j^{th} joint. Thus, the full set of displacements and the linear velocity Jacobian for the robot, including off-axis motions are

$$\mathbf{q}_{Full} = [\mathbf{q}_1,\, \mathbf{q}_2, \mathbf{q}_3,\, \mathbf{q}_4]^t, \tag{4.15}$$

$$J_{Full} = [J_1 \,|\, J_2 \,|\, J_3 \,|\, J_4], \tag{4.16}$$

where $\mathbf{q}_1$, $\mathbf{q}_2$ and $\mathbf{q}_3$ are the displacement sets for the prismatic joints and $\mathbf{q}_4$ is the displacement set for the rotational joint. The compliance matrix for the entire robot, including the off-axis displacements is

$$C_{robot} = J_{Full}\, \chi_{Full}^{-1}\, J_{Full}, \tag{4.17}$$

where χ_{Full} is a 14x14 diagonal matrix that contains the joint axis and off-axis stiffness values.

For a bone-attached robot, further deflection occurs at the interface of the bone anchor screws and the skull. To analyze and model this deflection, a finite element analysis (FEA) model of the robot attachment frame and bone anchor screws was developed. First, a structural model of the bone attachment frame was developed using the FEA software package ANSYS (ANSYS Inc., Canonsburg, PA, USA). However, since the deformation calculation must be performed many times and must be part of the overall error calculation, it was necessary to create a custom, simplified model in MATLAB (The Mathworks, Inc., Natick, MA, USA). The simplified FEA model treats the attachment frame as a structure with 18 nodes and 18 space frame elements (see [46] for MATLAB code and explanation of element types). Deflections at key points in the simplified model were compared to the full ANSYS model. The simplified model deflections averaged within 0.01 mm of the full model when tested under a range of simulated loads.

The bone anchoring screws (see Figure 4.9b) are also modeled as space frame elements with the matrix elements determined from experimental data. Data was used from experiments performed by Kobler et al. on cadaver temporal bones and phantom material in [67], which determined an axial stiffness coefficient of the anchor. Additional experiments were performed on fresh cadaver bones, which determined a

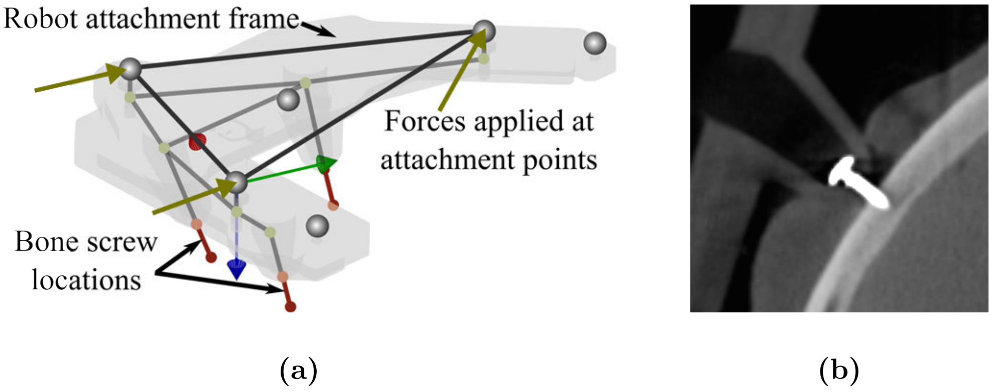

(a) (b)

Figure 4.9: (a) Simplified FEA model of robot positioning frame and bone anchoring screws; the screw stiffnesses are based on experimental data. (b) Image of bone anchoring screw inserted through positioning frame leg and into skull surface of cadaver.

torsional stiffness coefficient. Both of these stiffness coefficients were determined from experiments in ex vivo bones in controlled laboratory conditions and attachment in the operating room on a real patient would likely be more challenging, and perhaps result in less rigid fixation. To account for this imperfect attachment in practice, the stiffness values are randomly varied between 75% and 100% of the nominal values in the error model. For a given set of stiffness values, a three-dimensional space frame element is fit to this data and the compliance matrix associated with bone attachment, C_{attach}, is calculated.

The force at the drill tip, $\mathbf{f}_i$, is estimated using prior research in evaluating the forces during mastoidectomy [35]. Since the safety margin calculation is independent of the final robot trajectory, factors that influence the force magnitude and direction are not known at this stage of the planning process (e.g. cutting velocity, depth, drill angle at the specific voxel). Thus, forces associated with more aggressive cutting parameters (e.g. velocity of 4.0 mm/s, depth of 1.6 mm) are used and applied in random directions at the drill tip. An additional factor of safety is applied to these values to account for lower spindle speeds compared to the value of 80,000 rpm used for all trials in [35].

The deflection caused by compliance of the robot is considered separately from that caused by compliance of the robot attachment since the attachment also depends on the weight of the robot (and orientation on patient). The tip deflection due to milling forces and robot compliance is given by:

$$\Delta \mathbf{p}_i(\text{robot}) = C_{robot}\mathbf{f}_i. \tag{4.18}$$

The deflection of the positioning frame is caused by the same tip force as well as the weight of the robot, which depends on the orientation of the patient's head in surgery.

$$\Delta \mathbf{p}_i(\text{attach}) = C_{attach}\,(\mathbf{f}_i + \mathbf{f}'_{weight}), \tag{4.19}$$

where $\mathbf{f}_{weight} = \mathbf{m}_{robot}\mathbf{g}$ and $\mathbf{f}'_{weight}$ is equal to $\mathbf{f}_{weight}$ except it is zero in the direction toward the skull since the tips of the legs cannot move downward into the skull. $\mathbf{m}_{robot}$ is the mass of the robot and $\mathbf{g}$ is the gravity vector. Since the robot is in series with the attachment frame, the deflections are added and

$$\Delta \mathbf{p}_i = \Delta \mathbf{p}_i(\text{robot}) + \Delta \mathbf{p}_i(\text{attach}). \tag{4.20}$$

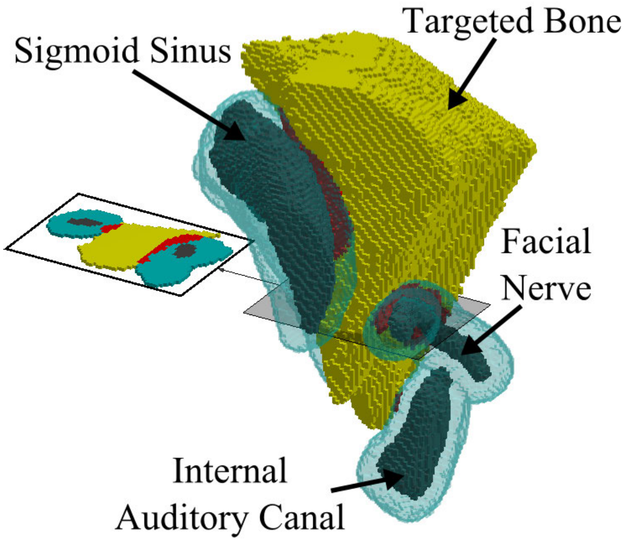

Figure 4.10: Final safety margins for several critical structures in simulation. Portions of the original target volume (in red) are removed as a result of the safety margin dimensions.

4.4 Simulation of Robotic Mastoidectomy Planning

The algorithm was tested on five scans of human cadaver heads that were used for prior experiments with the robotic system. Automatic segmentations of the facial nerve, chorda tympani, and external auditory canal (EAC) were performed using the algorithms described in [93] and segmentations of the sigmoid sinus and internal auditory canal (IAC) were performed manually. The segmentation boundaries were confirmed by an experienced surgeon. These structures were provided as inputs to the algorithm along with their associated preservation probability values. The parameter values used for each error source, as outlined in Section 4.3, are provided in Table 4.1.

Table 4.1: Parameter values used in simulation for generating patient-specific safety margins for robotic mastoidectomy.

Error Source	**Parameter**	**Simulation Model Values**
Image distortion (affine transformation matrix)	A	$\sigma_{A(i=j)}$ (diagonal terms) $= 0.03\%$, $\sigma_{A(i\neq j)}$ (off-diag terms) $= 0.03\%$
Registration (fiducial localization error)	FLE	RMS FLE = 0.091 mm
Joint initialization	$\mathbf{e}_{q,init}$	$\sigma_{q,init}(\text{Prism}) < 0.01$ mm, $\sigma_{q,init}(\text{Rot}) = 3.4 \times 10^{-4}$ rad
Joint transmission backlash and clearance	$\mathbf{e}_{q,trans}$	$\sigma_{q,trans}(\text{Prism}) = \pm 0.017$ mm, $\sigma_{q,trans}(\text{Rot}) \approx 0$ rad
Joint sensing	$\mathbf{e}_{q,sens}$	$e_{q,sens}(\text{Prism}) \approx 0$ mm, $\mathrm{e}_{q,sens}(\text{Rot}) < 1 \times 10^{-4}$ rad
Joint motion control and interpolation	$\mathbf{e}_{p,ctrl}$	$\lvert\mathbf{e}_{p,ctrl}\rvert = \text{rand}([-0.05, 0.05])$ mm
Robot geometry calibration	$\mathbf{G}$ $\hat{\mathbf{u}}_{q,i}$	$\sigma_G(\text{Length}) = 0.08$ mm, $\sigma_G(\text{Ang}) = 5.24 \times 10^{-4}$ rad, $\sigma_{\mathrm{u},\phi} = 1.1 \times 10^{-3}$ rad
Prismatic joint compliance	$\mathbf{k}_i$ (Prism) $=$ $[k_{qi}, k_{\alpha,i}, k_{\beta,i}, k_{\gamma,i}]$	$\mathbf{k}_i$ (Prism) $= [3.23\frac{\text{kN}}{\text{mm}}, 2000\frac{\text{Nm}}{\text{rad}}, 1250\frac{\text{Nm}}{\text{rad}}, 1429\frac{\text{Nm}}{\text{rad}}]$
Rotational joint compliance	$\mathbf{k}_i$ (Rot) $= [k_{qi}, k_{\phi,i}]$	$\mathbf{k}_i$ (Rot) $= [690\frac{\text{Nm}}{\text{rad}}, 2750\frac{\text{Nm}}{\text{rad}}]$
Bone-attachment compliance	$\mathbf{k}_{anchor} = [k_{axial}, k_{rot}]$	$\mathbf{k}_{anchor} = [760\frac{\text{N}}{\text{mm}}, 5\frac{\text{Nm}}{\text{rad}}]$ $\times$ rand$([0.75, 1])$
Forces at drill tip	$\mathbf{f}_{tip}$	$\lvert\mathbf{f}_{tip}\rvert$ (RMS) = 6 N

Table 4.2: Results of simulation of safety margin algorithm (five cadaver scans).

Structure	**Preservation Prob. (%)**		**Margin Volume (mm^3)**		**Removed Target (mm^3)[b]**
	Desired	**Final**	**Original[a]**	**Final**	
Facial Nerve	99.9	99.91±0.01	106 ± 6.2	485 ± 44	25.6 ± 11.1
Chorda Tymp.	95.0	95.17±0.13	16 ± 1.3	111 ± 11	0.0 ± 0.0
EAC	95.0	95.11±0.04	682 ± 124	715 ± 52	1.2 ± 2.3
Sigmoid Sinus	99.0	99.05±0.03	1055 ± 349	1364 ± 275	77.5 ± 64.3
IAC	99.0	99.04±0.04	214 ± 39	404 ± 53	12.9 ± 24.2

[a] Original volume includes all voxels in the image that partially overlap with nerve segmentation.

[b] Removed target volume is dependent on the initial segmentation by the surgeon.

Results of the simulation are given in Table 4.2. The desired safety threshold for each structure is listed along with the volume of the associated safety margin. The targeted volume segmented by a surgeon was compared with the safety margins to determine how much (if any) overlap occurred. There was overlap into the target volume for the facial nerve safety margin and the sigmoid sinus safety margin. The facial nerve has the highest safety threshold (99.9%) and thus is most likely to impact the permissible workspace of the robot. The sigmoid sinus is not considered to be as critical of a structure so the desired preservation probability is lower. However, the large size of the sigmoid sinus increases the likelihood that there will be some overlap with its safety margin and the desired volume since there are so many nearby voxels that could potentially cause damage if targeted.

Figure 4.10 shows the resulting safety margins of several structures. The red voxels are the voxels that were removed from the planned target volume. Figure 4.11 shows cross-sectional views of the facial nerve and safety margin at a single iteration of the

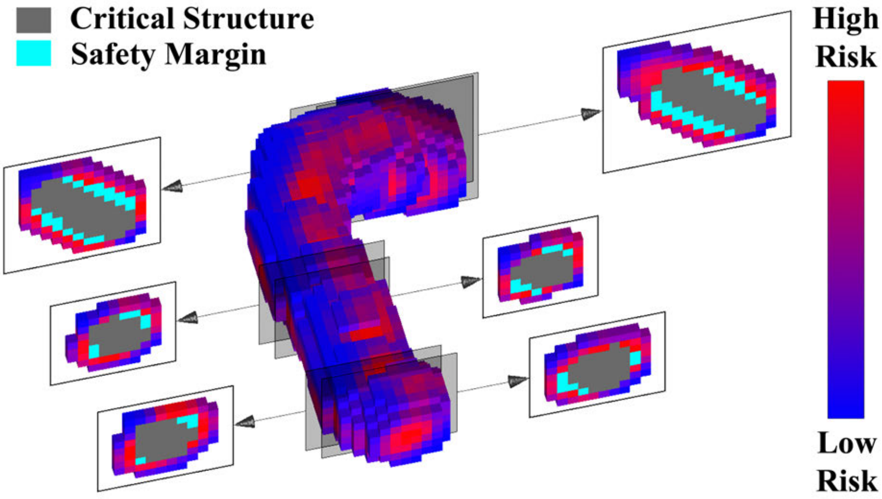

Figure 4.11: Schematic of individual voxel risk around the facial nerve at one iteration of the algorithm. The shading indicates the relative risk of the voxels surrounding the margin. At each iteration, a percentage of the highest risk voxels are added to the safety margin to bring the probability of preserving the structure closer to the desired threshold.

algorithm. The risk levels of the voxels surrounding the safety margin are indicated with different color shading. The anisotropic error sources result in the safety margin having an elliptical cross-section.

The spatially varying safety margins generated by the algorithm were then compared to uniform safety margins, specifically for the facial nerve. Two types of uniform margins were generated. First, the safety margin algorithm applied above was used, with the exception that the margins were grown uniformly outward instead of adding only the highest risk voxels at each algorithm iteration. Thus, these uniform margins will have a final estimated preservation rate equal to that of the spatially varying margins. The purpose of this is comparison is to quantify the effect of adding to higher risk voxels on the size of the final margin.

Second, safety margins of arbitrary thicknesses were compared. This is the type of margin that would be generated if the surgeon said, “I want the planned volume to be at least 1 mm away from the facial nerve.” The purpose of this comparison is to determine the predicted damage risk of margins generated in this manner and measure the inter-patient risk variability of margins of a constant arbitrary thickness. The results of comparing different safety margin generation methods are provided in Table 4.3.

4.5 Discussion

This chapter provides an algorithm for generating statistically-driven safety margins around vital structures based on estimates of imaging, registration, and robot errors. Prior work is expanded upon by incorporating a range error sources present in any image-guided, surgical robotic system and providing a framework for combining the various error distributions. The algorithm was applied to a bone-attached robotic system for mastoidectomy and generated variable-thickness safety margins around several vital anatomical structures. These safety margins were used to modify segmented target volumes so that the desired preservation probabilities of each of the vital structures are met. The algorithm, however, can be applied to any surgical procedure in which a robot is moving through a planned path or region near vital anatomy that must be avoided. If stochastic estimates of the error sources are known, the formulation laid out in this work can be followed to develop a safety margin algorithm for any such procedure.

Additionally, this approach allows for analysis of system error in a way that is very

Table 4.3: Comparison of various methods for generating safety margins around the facial nerve.

	Spatially Varying Margins		**Uniform Margins - Rate Based**		**Uniform Margins - Specified Thickness**[c]		
No.	***Thickness (mm)***[a]	***Preservation Prob.***[b]	***Thickness (mm)***	***Preservation Prob.***[b]	***1.0 mm Pres. Prob.***	***1.5 mm Pres. Prob.***	***2.0 mm Pres. Prob.***
1	1.75 ± 0.15 (1.30, 2.13)	>99.9%[d]	1.74	>99.9%[d]	<90.0%	98.76%	>99.9%[d]
2	1.70 ± 0.11 (1.32, 2.03)	>99.9%	1.74	>99.9%	<90.0%	95.42%	>99.9%
3	1.70 ± 0.20 (1.10, 2.13)	>99.9%	1.73	>99.9%	<90.0%	98.44%	>99.9%
4	1.64 ± 0.20 (1.08, 2.16)	>99.9%	1.74	>99.9%	<90.0%	97.18%	>99.9%
5	1.63 ± 0.21 (1.10, 2.05)	>99.9%	1.74	>99.9%	<90.0%	96.20%	>99.9%

[a] Mean Value ± Standard Deviation (Minimum Value, Maximum Value)

[b] Preservation probability specified as input to the algorithm.

[c] Uniform margins calculated by expanding nerve segmentation by the given thickness. Then, preservation probability of margin evaluated using the first step of the algorithm (Monte Carlo simulation of surgery with errors sampled from distributions).

[d] Given the number of iterations of the Monte Carlo simulation, it is only possible to accurately predict probabilities to a precision of three decimal places.

specific for the intended use. By adjusting the different error distribution parameters and observing the effects on the size of the necessary safety margins for given preservation thresholds, the system components that cause meaningful error are apparent and system improvements can focus on these components. For example, when determining the number of and configuration of fiducial markers, simulations can be run to determine the impact on the overall system error. Similarly, when choosing between actuators of different size and stiffness, the impact of the stiffness difference can be more accurately understood by running simulations.

Finally, the comparisons between the spatially varying margins and uniform margins indicate the need for generating safety margins specifically for each patient. For example, a margin thickness of 1.5 mm around the facial nerve provides a preservation probability of 95.4% for one patient and a 98.7% for another patient. This difference represents how the accuracy of the system can vary according to the fiducial placement and position of the anatomy relative to the robot and thus affects the likelihood of damaging a vital structure.

Using this algorithm, the selection of the desired preservation probability becomes a key component of the safety margin generation process as it directly affects the margin size. The first reaction from a surgeon when asked at what probability he/she wants a particular vital structure preserved is always, “100 Percent!”. However, many of the error sources present in an image-guided robotic system are probabilistic and thus a guarantee of preservation of a structure is impossible, even if the error distributions are known perfectly (which, of course, they are not). In some cases, the error sources can be bound within a maximum range (e.g. a joint on the robot can only deflect so much under load before it reaches a mechanical hard stop). If such maximum bounds were used or a preservation probability very close to 100% (e.g. 99.9999%) was chosen, the resulting margin size would likely be so large that it makes the allowable workspace insufficient for the surgery.

Thus, the user interaction with the algorithm for generating safety margin then becomes an optimization between safety and usefulness of the image-guided robotic system. A good practical rule of thumb would be to specify a preservation probability that exceeds the current standard of care by a reasonable factor. Ultimately, surgeon comfort with the system and personal risk tolerance will certainly play a role, but by using a statistics-based algorithm, the margin selection will become less arbitrary and tied more strongly to actual risk.

Chapter 5

Patient-Specific Trajectory Planning for Robotic Mastoidectomy

The work in this chapter continues the focus on improving the planning of robotic mastoidectomy through the use of novel, patient-specific algorithms. Specifically, a method for generating patient-specific trajectories for robotic milling of the temporal bone that incorporates force modeling and proximity to vital anatomy is presented.

5.1 Introduction

Much of the motivation for the planning method described in this chapter comes from the way in which surgeons perform bone milling in otologic surgery. Surgeons adjust their speed and tool incidence angle constantly, which enables them to efficiently mill porous bone. Surgeons also adjust their accuracy requirements (via speed and depth of cut) throughout the procedure based on proximity to sensitive structures, like nerves and blood vessels.

Unlike surgeons, robots are typically programmed to mill bone like an industrial Computer Numeric Controlled (CNC) milling machine (constant velocity and depth). This approach does not account for the large air pockets and density variations of the mastoid region (see Figure 5.1). The number and size of these air pockets varies con-

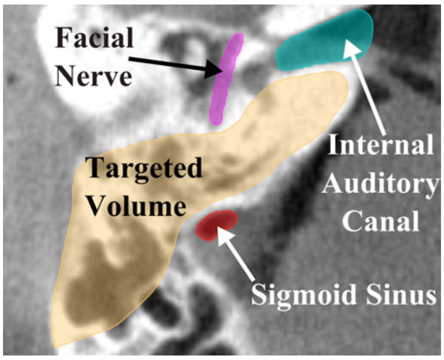

(a)

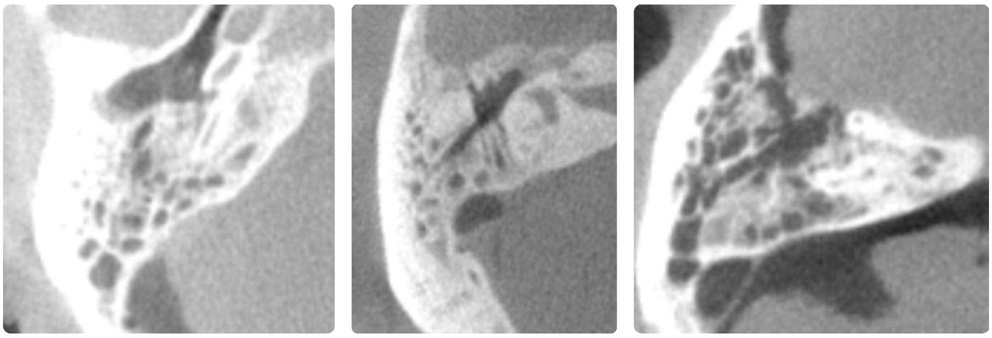

(b)

Figure 5.1: (a) A slice of a CT scan of the temporal bone region. Both the target and vital anatomy that must be avoided are illustrated. (b) Temporal bone CT scans of several patients. Note the inter- and intra-patient variation of bone porosity and density, which is approximated by image intensity.

siderably between patients, and the density of bone varies spatially for each patient. These inter- and intra-patient differences are accounted for in the algorithm described in this chapter through the use of pre-operative imaging and force modeling. Robot trajectories are planned that account for these patient-specific bone property variations as well as the proximity of vital anatomical structures to the cutting burr. In comparison to treating the target region as a homogeneous volume of bone to be removed like a CNC path, this approach enables faster bone removal in areas with lower bone density and in areas far from critical structures. As the burr moves closer to the critical structures, cutting forces that would cause the tool to deflect in the direction of the structure and increase heat generation near temperature-sensitive anatomy are minimized by adjusting the robot velocity and orientation of the surgical drill.

Several methods have been previously proposed for incorporating bone density variations into the planning and/or control of robotic bone drilling and milling. Sugita et al. employed a control scheme that accounted for the transitions between different bone types (cortical and cancellous) and air for reduction of procedure time and minimization of large force spikes in orthopedic bone milling [116]. Wang et al. used force-based control and knowledge of typical force levels in different areas of the vertebrae to avoid drill penetration beyond the targeted bone and damage to nerves [125]. In the field of otologic surgery, Williamson et al. used the correlation between drilling force and bone density to predict the pose of a robot-controlled drill based on density estimates from the pre-operative images and real-time force measurements [127]. Additionally, forces in otologic bone milling have been modeled in the development of a physics-based haptic simulator [4]. The voxelized model developed by Arbabtafti et al. [4] is used in the present work to adjust the cutting tool orientation and velocity along the trajectory for autonomous temporal bone milling such that the forces are decreased when the tool is in close proximity to vital anatomy and the tool is oriented for improved cutting efficiency.

5.2 Motion Planning

5.2.1 Cartesian Path

The first step in the planning procedure is to generate a three-dimensional milling path through the bone that covers as much of the target volume as possible without crossing into untargeted regions (bone that need not be removed, or other anatomy). The output of this portion of the planning procedure is a list of N target points in the image coordinate frame. The only restriction on this path is that the current target point is reachable by the cutting burr and not beneath unmilled bone (i.e. target points 1 to i-1 must provide access to point i for the drill). This path can be calculated using a number of approaches, including a simple "lawnmower" approach (e.g. [41, 116]), contour parallel tool paths [29], or the method described in Section 3.3. Given this tool path, the remainder of this chapter focuses on selecting the tool orientation and cutting velocity using patient-specific data.

For each step along the 3D path, a range of permissible drill orientations can be calculated. This is done by examining the volume of bone previously removed in proximity to the point under consideration. Any shaft orientation that reaches the point, without colliding with unmilled bone, is considered a permissible orientation. Since the cutting burr is constantly rotating about its axis, only two orientation angles must be considered: ϕ and θ (see Figure 5.2).

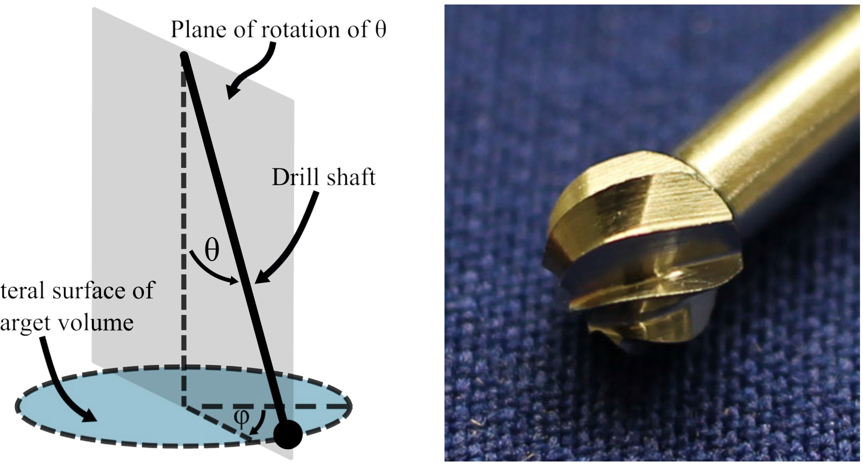

(a) **(b)**

Figure 5.2: (a) Orientation angles of the surgical drill with respect to the bone surface. Since the drill rotates continuously, only two angles must be considered: θ and ϕ; (b) Photograph of a fluted cutting burr used in otologic surgery.

Efficient Cutting Angle

Surgical cutting burrs are typically spherical in shape with either a fluted or diamond-coated surface. Due to its shape, the side of the burr (i.e. near its equator) cuts more efficiently than the distal tip. In the study presented in Section 2.2 and [35], in which forces during milling of the temporal bone were measured, large force spikes (well beyond the mean forces for the parameters) were observed for spherical otologic burrs when primarily cutting with the distal tip. In clinical practice, surgeons use the side of the burr whenever possible to increase cutting efficiency. As a simple metric for quantifying the amount of bone being cut with the side of the burr compared to the tip of the burr, an inertia-like quantity can be used:

$$I = \sum_{i=1}^{n} \rho_i V_i d_i^2 = \sum_{i=1}^{n} \rho_i V_i (r^2 - z_i^2), \tag{5.1}$$

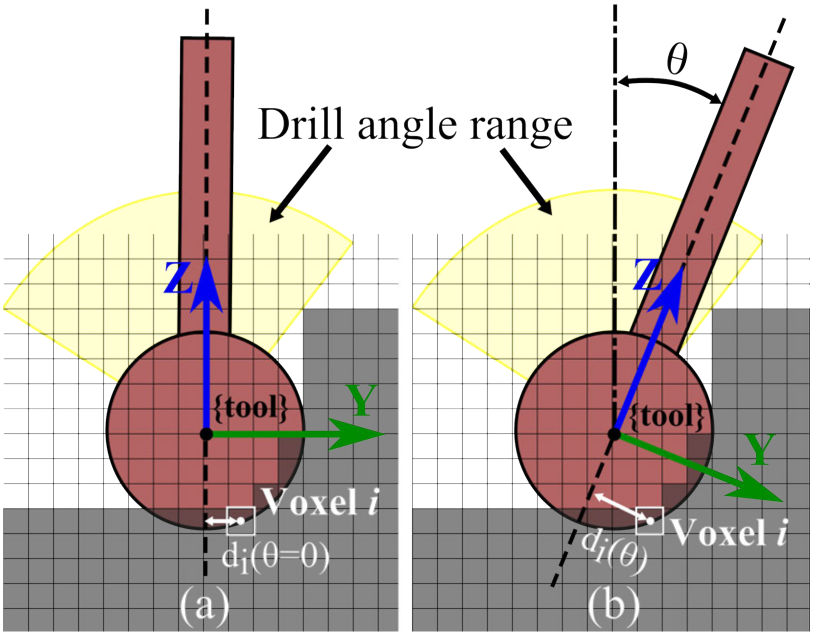

Figure 5.3: Cross-sectional illustration of the range of permissible angles at a given point along the path. Optimal shaft angle (θ) is determined based on the intensity and location of each voxel with respect to the drill shaft (d_i). Note that d_i also has a component in the x-direction in the 3D case and that all of the voxels being cut are at the surface of the spherical burr. The figure shows how the distance between the shaft axis and the center of a single voxel changes with θ.

where $i = 1...n$ represents all of the voxels that are at least partially covered by the cutting burr, ρ_i is the voxel density, V_i represents the partial volume of a given voxel, and d_i is the perpendicular distance from the shaft axis to the center of the voxel. The rightmost expression in Equation 5.1 gives d_i^2 in terms of the radius of the burr, r, and z_i (the z-coordinate of the voxel in the tool coordinate frame shown in Figure 5.3). Density is estimated based on the intensity of the voxel in the pre-operative computed tomography (CT) scan. For different shaft orientations, the density and partial volume remain the same while d_i varies (see Figure 5.3). I is maximized when the side of the burr is removing the largest quantity of bone possible. To account for varying quantity of bone along the path, I can be normalized based on the total amount of bone (calculated based on volume of each voxel covered by the burr and intensity in image) that is to be removed at the given step:

$$I_n = \frac{\sum_{i=1}^{n} \rho_i V_i (r^2 - z_i^2)}{\sum_{i=1}^{n} \rho_i V_i r^2}, \tag{5.2}$$

which gives a value between 0 and 1. The normalization keeps the magnitude of this component of the orientation calculation in the same range for all points so the contribution of this component is consistent throughout the trajectory.

Reducing Forces Near Vital Anatomy

The orientation of the burr also influences the magnitude and direction of the cutting force between the burr and the bone. This is particularly true for spherical surgical burrs and non-homogeneous bone, where there can be considerable differences in cutting force direction with orientation change. When milling near vital anatomical structures in the temporal bone (e.g. the facial nerve), it is desirable to reduce the forces for two reasons. First, reduction of force in the direction of the structure decreases the likelihood of the burr deviating from the plan and colliding with the structure that needs to be preserved. Second, lower forces reduce the heat generation, decreasing the likelihood of thermal damage.

The model developed by Arbabtafti et al. [4] as part of their haptic simulator for bone machining using a spherical fluted cutting burr enables force estimation based on position of the burr and voxel intensity values. This model can be used to aid in robotic trajectory planning by predicting the forces based on the pre-operative images. From the Arbabtafti model, the total force acting on each blade at any instant is given by:

$$\begin{bmatrix} F_x \\ F_y \\ F_z \end{bmatrix} = \oint_s \begin{bmatrix} dF_x \\ dF_y \\ dF_z \end{bmatrix} = \oint_s \left(T_{local}^{tool} \begin{bmatrix} K_t \\ K_r \\ K_a \end{bmatrix} t \right) ds, \tag{5.3}$$

where K_t, K_r, and K_a represent the specific cutting energy for the material in the tangential, radial, and axial directions of the local coordinate frame, respectively, T_{local}^{tool} is the transformation between the local coordinate frame at the cutting position and the tool coordinate frame, and t is the chip thickness or depth of cut. Note that T_{local}^{tool} is unique for each position on the surface of the cutting burr (see Figure 5.4). The cutting energies can be calibrated for the particular material by recording forces at various depths and tool orientations. The cutting tool also impacts the calibration since its geometry can influence how chips are removed, which can affect the forces on the tool.

Using Equation 5.3, the differential forces acting along the blade are integrated over the entire surface of the blade engaged in cutting. This equation is expanded in discrete form for use in voxelized images and to account for all cutting blades [4]. The forces along each discretized element of a blade are integrated along the z-direction at N_γ angular increments as the blade moves through a total angle of Ψ, which is the angle between two blades. This calculation is performed for each of the blades $(1...N_\beta)$ and averaged for each of the angular increments to obtain the total force on

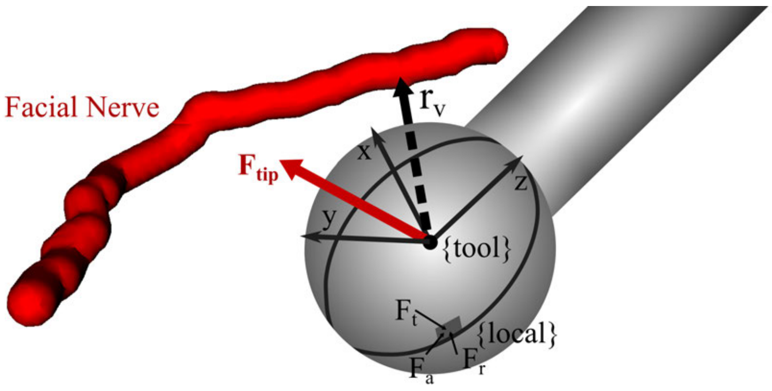

Figure 5.4: Cutting burr in a position close to vital anatomy (facial nerve) showing the vector, $\mathbf{r_v}$, pointing from the burr center to the nearest point on the nerve. The tool coordinate frame and force vectors in the local coordinate frame for a single point along a blade are shown in the figure. F_t, F_r, and F_a represent the tangential, radial, and axial components of the force in the local coordinate frame, respectively.

the burr:

$$\begin{bmatrix} F_x \\ F_y \\ F_z \end{bmatrix} = \left(\sum_{i=1}^{N_\beta} \sum_{j=1}^{N_\gamma} \sum_{k=1}^{N_z} T_{local}^{tool} \begin{bmatrix} K_t \\ K_r \\ K_a \end{bmatrix} t(i,j,k) dz \right) / N_\gamma \tag{5.4}$$

where N_z represents the number of differential elements along the cutting blade in the z-direction and dz is the height of each element. See [4] for a more detailed derivation of the above equation.

The direction of the force, $\mathbf{F} = [F_x, F_y, F_z]^T$, can be compared to the vector between the cutting burr and the nearest point on the vital structure, $\mathbf{r}_v$, to determine if the cutting force is pushing the burr towards the structure (see Figure 5.4). The component of the force in the direction of the vital structure is:

$$F_v = \mathbf{F} \cdot \hat{\mathbf{u}}_v \tag{5.5}$$

where $\hat{\mathbf{u}}_v$ is the unit vector along $\mathbf{r}_v$ (F_v is set to 0 for $\mathbf{F} \cdot \hat{\mathbf{u}}_v < 0$). This information can be used to adjust the orientation of the drill such that the resultant force in the direction of the vital structure is minimized. Therefore, if there is a deflection of the robot, the likelihood of that deflection causing damage to the patient is reduced.

Orientation Selection

Given a range of shaft orientations for which the robot can safely reach the current target point, knowledge of what bone has been removed thus far in the path, and the CT scan of the patient, a desired shaft orientation can be calculated by minimizing a cost function that incorporates Equations 5.2 and 5.5:

$$C = \alpha_1 \frac{F_v}{||\mathbf{F}||} + \alpha_2(1 - I_n) \tag{5.6}$$

$$\begin{bmatrix} \theta_{desired} \\ \phi_{desired} \end{bmatrix} = \text{argmin}(C, [\theta, \phi]). \tag{5.7}$$

The coefficients α_1 and α_2 are varied based on the proximity to the nearest vital structure. When the burr is close to a structure that must be avoided, the first term of the cost function is the primary consideration. As the burr moves further away from the structure, the second term becomes the primary consideration. The scaling for a given point is based on the distance away from the vital structure at that point compared to the minimum allowable distance, $r_{v,min}$, as follows:

$$\alpha_1 = \alpha_{1,max} e^{-\kappa_\alpha (r_v - r_{v,min})} \tag{5.8}$$

$$\alpha_2 = 1 - \alpha_1 \tag{5.9}$$

where κ_α determines how quickly the value of α_1 drops off with distance away from the structure and $\alpha_{1,max}$ is the maximum value of α_1 (i.e. the value when the burr is very close to the structure). If multiple vital structures are used in the planning algorithm, the closest one can be chosen for a given calculation. If multiple structures are in close proximity to the burr at any point in time, the higher priority structure can be used in the calculation. Alternatively, an additional term can be added to Equation 5.6 to represent the force directed toward the second structure.

5.2.2 Incorporating Robot Deflection

Instead of simply using the direction of the force on the cutting burr, the deflection of the burr can be estimated given knowledge of robot stiffness. Assuming quasi-static loading and that the robot links are rigid relative to the joints, tip deflection can be approximated for a given force as:

$$\Delta \mathbf{p} = \begin{bmatrix} \Delta x \\ \Delta y \\ \Delta z \end{bmatrix} \approx C(q)\mathbf{F} \tag{5.10}$$

where $C(q) = J\chi^{-1}J^T$ is the compliance matrix of the robot. J is the robot Jacobian and $\chi = \text{diag}[k_1, ..., k_m]$ is a matrix of joint stiffnesses, where k_i $(i = 1...m)$ are the stiffness values for each of the m robot joints. Stiffness values representing "virtual joints" as described by Abele et al. [2] and used in the error model in Chapter 4 can also be included to account for off-axis joint compliance. Then, Equations 5.5 and 5.6 become:

$$\Delta p_v = \Delta \mathbf{p} \cdot \hat{\mathbf{u}}_v \tag{5.11}$$

$$C = \alpha_1 \frac{\Delta p_v}{||\Delta \mathbf{p}||} + \alpha_2(1 - I_n) \tag{5.12}$$

Δp_v is set to 0 for $\Delta \mathbf{p} \cdot \hat{\mathbf{u}}_v < 0$.

5.2.3 Cutting Velocity

The velocity of the cutting burr along the trajectory is selected based on two factors: the amount of bone being removed and the orientation of the shaft at that point. When there is more bone (in terms of both volume and density), the robot should be programmed to cut slower. Since the total force is proportional to the mass of bone in contact with the burr and inversely proportional to the cutting velocity, an inverse relationship between mass and velocity is used ($v_{cut} \propto \frac{1}{m}$). The "mass" of bone can be calculated from image intensity and the partial volume of voxels within the burr as $m = \sum_{i=1}^{n} \rho_i V_i$. To also account for the orientation-based cutting effectiveness and proximity to vital anatomy, the value determined from Equations 5.6 or 5.12 is used. A low minimum cost function value means that there is an achievable orientation that provides good cutting performance. Thus, the velocity should be higher for lower values of C.

$$v_{cut} = k_{vel} \frac{1}{m} (1 - C) \tag{5.13}$$

where k_{vel} is a constant value that accounts for the magnitude of the intensity mapping such that the mean calculated velocity falls in the center of the allowed velocity range ($v_{min} \leqslant v_{cut} \leqslant v_{max}$). The above equation yields high velocities at points when the amount of bone in contact with the burr is low or the bone to be cut is located at the side of the burr. Lower velocities are commanded when the burr is in contact with a large amount of dense bone, close to a vital anatomical structure, or it is not oriented well for efficient cutting. Due to the presence of air cells, the commanded v_{cut} values can fluctuate rapidly as the burr moves in and out of air cells. A simple weighted, moving average filter is applied to the v_{cut} data to ensure smooth motion and avoid very high accelerations at bone/air transition points.

5.2.4 Joint Trajectory Generation

The joint trajectory is generated from the target points ($\mathbf{p}_{burr}$), velocities (v_{cut}), and desired orientation values (θ_{des}, ϕ_{des}). The desired drill orientation, as determined from minimizing the cost function, may change suddenly due to variable bone density and porosity. Thus, it is necessary to smooth these values to avoid rapid angle changes that may require joint velocities beyond the limits of the robot and reduce the ability of the surgeon to safely monitor the procedure. This smoothing can be applied directly to the desired angular values by using a low-pass filter. Alternatively, the orientation could be accounted for by considering only the Cartesian path positions as the task space and steering the orientation towards the desired value as a subtask in a redundancy resolution approach.

5.3 Experimental Methods

The algorithm described in this chapter was tested on the four degree-of-freedom (DOF), bone-attached robot designed for mastoidectomy presented in Section 3.5 (see Figure 5.5). As described in Chatper 3, bone-attached robots can achieve higher positional accuracy since they do not require intra-operative tracking, which inher-

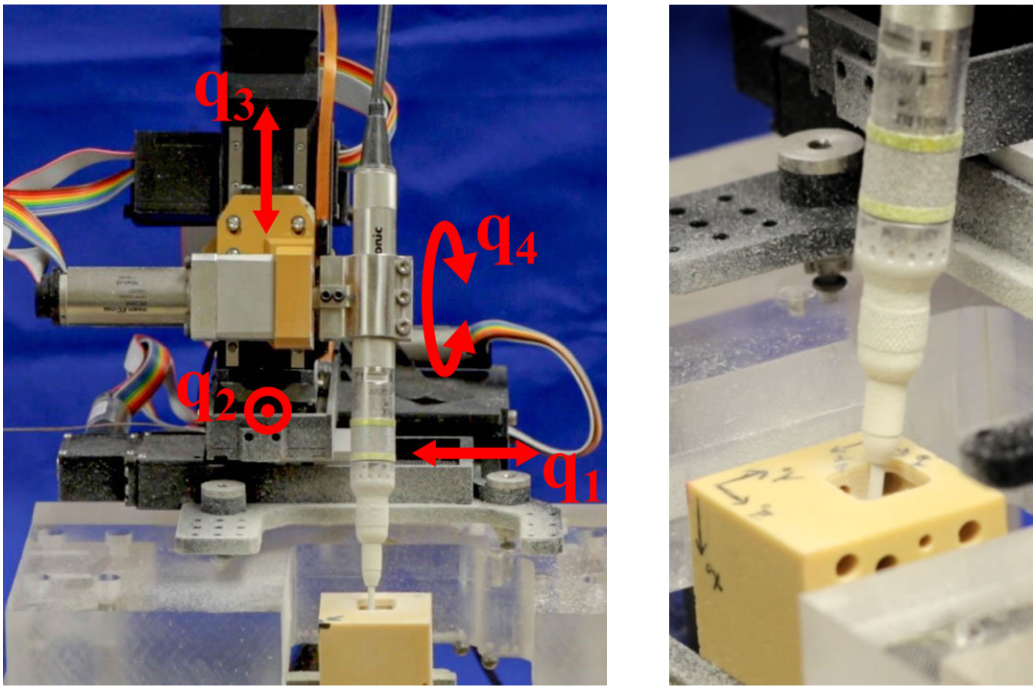

Figure 5.5: (a) Four DOF bone-attached robot for mastoidectomy mounted to test platform. The fourth joint (q_4), which controls the drill orientation (θ) is determined by the optimization algorithm. (b) Close-up of surgical drill milling temporal bone phantom during an experiment.

ently introduces some level of registration error. However, they must be made small enough to mount on the patient without causing too much stress on the mounting points. Thus, these robots may not be as stiff as a larger robot and can therefore benefit from a planning algorithm that incorporates the minimization of deflection towards vital anatomy. Since the robot used in these experiments has three linear joints and one rotational joint, the drill shaft orientation is defined by this joint and the cost function is minimized over one variable, θ.

Experiments were performed using Sawbones mechanical test blocks (Pacific Research Laboratories, Vashon Island, WA USA) made from solid rigid polyurethane

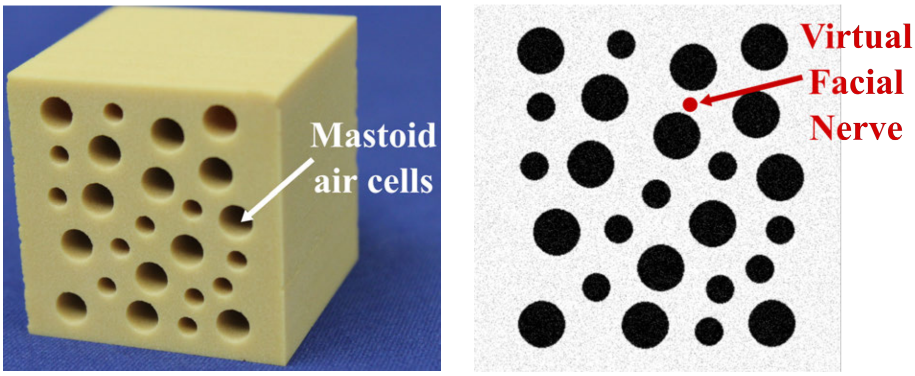

Figure 5.6: (a) Photo of biomechanical test block used in experiments and (b) image slice of test block showing virtual facial nerve that was added to the image for testing the planning algorithm.

foam ($\rho = 0.8\frac{g}{cm^3}$). The blocks were custom-machined to add holes (3-5 mm in diameter) that mimic the air cells found in the mastoid region of the temporal bone. Figure 5.6 shows a photograph of the test blocks and a slice of the image used for planning. To simplify the experimental protocol, the image was generated from a model of the custom-machined test blocks. To make the image-based planning more realistic, Gaussian noise with a standard deviation of 5% of the mean voxel intensity was added to the generated image. A virtual facial nerve was added to the image (see Figure 5.6b) and its position was used in the trajectory planning algorithm. The block was placed in an experimental jig at a known location with respect to the robot. The same planning process would be used if the image was acquired using a CT scanner with the additional steps of localizing the structures and registering the anatomy to the robot.

A total of three experimental trials were performed. All trials were performed with the same Cartesian path at the same location in the phantom block, which enabled comparison between the different optimization approaches. The trajectory optimization step described in this paper is independent of the Cartesian path, therefore any path could have been used in the experimental trials. For simplicity, the path used was a simple "lawnmower" type path in which the volume of bone was removed layer-by-layer. The outer path dimensions were 15 mm x 15 mm x 15 mm and the depth of each layer was 1.5 mm.

The first two trials were performed to evaluate the orientation selection component of the motion planning algorithm. The first trial, which serves as the control trial, used a constant angle ($\theta = 0°$) and constant milling velocity ($v = 1.5\frac{\text{mm}}{\text{sec}}$). The second trial was constrained to the same velocity but the orientation was varied along the path, with the value selected by minimizing Equation 5.6. The optimization was performed using the `fminbnd` function in MATLAB 2015a (The MathWorks Inc., Natick, MA, USA). The drill inclination angle θ was bounded by both the limits of the robot and the constraints imposed by the unmilled bone at each point along the trajectory. Forces were recorded throughout both trials using a six axis force/torque sensor (Mini40, ATI Industrial Automation, Apex, NC, USA) positioned between the second and third joints of the robot. The force data was smoothed using a moving average filter and analyzed according to the position of the cutting burr at the time of the force reading. When the burr was within 2 mm of any point on the facial nerve, the measured force was projected along the unit vector between the burr and the closest point on the nerve ($\hat{\mathbf{u}}_v$). The magnitudes of forces towards the facial nerve were compared for the two trials. Additionally, the force values for all points along the trajectory were compared for the two trials.

A third milling trial was performed to include the velocity scaling component of the motion planning algorithm as well as the orientation selection. The same Cartesian path used in the two trials described above was planned in the phantom material. For this trial, the linear velocity, v_{cut}, was regulated according to Equation 5.13. The linear velocities were scaled such that the total procedure time was equal to the control trial (9 minutes, 26 seconds) and a fair comparison of forces could be made to prior trials. Again, Equation 5.6 was used to select the drill orientation. The force data was recorded and compared to the first two trials.

5.4 Results

Figure 5.7 illustrates the reduction of forces towards the facial nerve that was achieved through the implementation of the proposed approach. When the cutting burr was within 2 mm of the facial nerve, the control trial resulted in a mean force of 0.51 N, a 75th percentile force of 0.67 N, and a peak force of 1.60 N. The trial using the orientation optimization had mean, 75th percentile, and peak force values of 0.32 N, 0.50 N, and 1.16 N, respectively. Finally, the trial using the full (orientation and velocity) optimization had mean, 75th percentile, and peak force values of 0.19 N, 0.33 N, and 0.80 N, respectively. Compared with the control trial, the full optimization trial resulted in a 63% reduction in mean forces and a 50% reduction in peak forces toward the facial nerve.

In addition to minimizing forces directed at the facial nerve, the proposed approach was found to produce an overall reduction of cutting forces throughout the milling

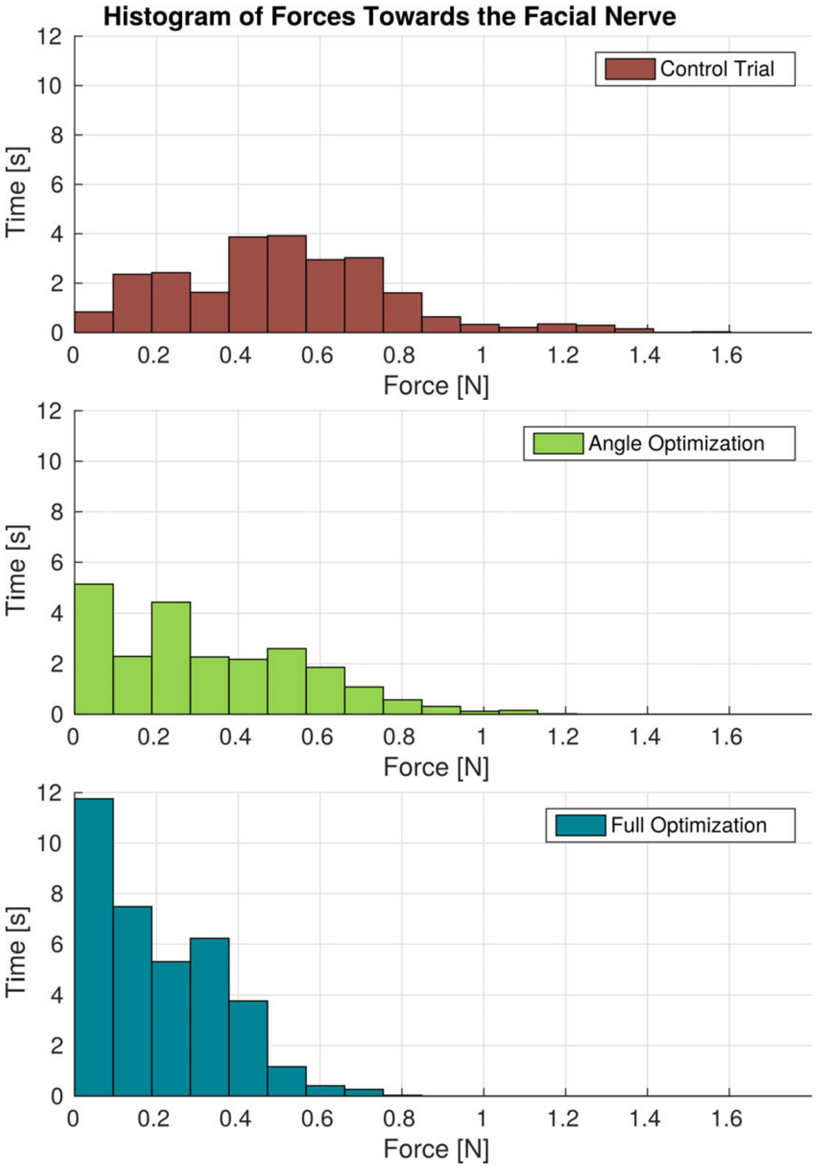

Figure 5.7: Cutting forces towards the facial nerve when the burr was within 2 mm of the nerve. “Angle Optimization” refers to the trial in which only the regulation of the incidence angle was enabled and “Full Optimization” refers to the trial that used both angle and velocity regulation based on Equations 5.6 and 5.13.

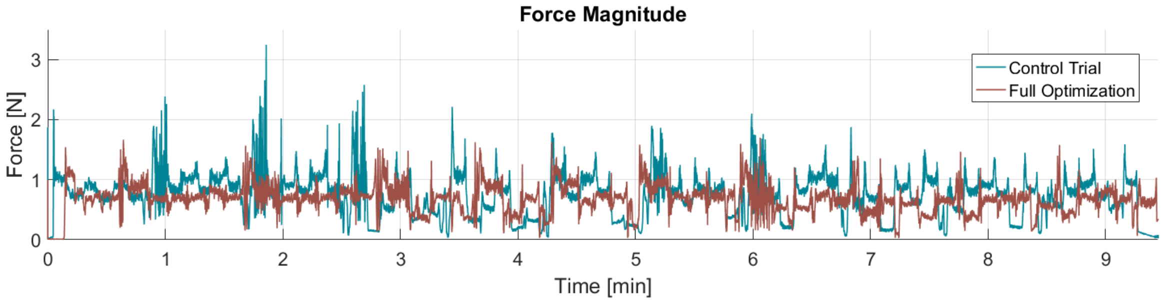

Figure 5.8: Force magnitude observed throughout the milling process. Here, "Full Optimization" refers to the trial that used both angle and velocity regulation. These plots show an overall reduction in mean and peak forces using the angle and velocity regulation. Note that the velocity was not constant throughout the full optimization trial, therefore specific points along the path for the two trials do not occur at the same time. Thus, this plot provides a general comparison of the overall forces rather than a comparison at specific points along the path.

process. This can be observed in the force magnitude plot (Figure 5.8): the control trial resulted in a mean and peak force of 0.73 N and 3.24 N, whereas the trial that used variable incidence angle and milling velocity had mean a mean force of 0.66 N and a peak force of 1.69 N.

5.5 Discussion

The experimental results demonstrate that the proposed methodology has the potential to decrease cutting forces near vital anatomical structures and throughout the bone milling procedure. This is attributed to the incidence angle and velocity regulation scheme described by Equations 5.6 and 5.13, which makes the robot mill more like a surgeon, i.e. varying the angle to control the cutting efficiency, moving slower when close to critical anatomy, and faster when in non-critical areas. This reduction of cutting forces is expected to bear two important clinical advantages. The first and most evident is that deflections of the robot towards vital anatomy (e.g. facial nerve, major blood vessels) will be smaller, thereby reducing the risk of accidental collisions when the burr is moving in close proximity to the structures. Second, lower cutting forces are expected to reduce the rate of thermal energy transferred to the surrounding bone, which could lead to heat-related trauma to the underlying vital structures. This latter implication is especially important in light of recent work that suggests high temperatures induced by bone drilling may cause thermal injury to the facial nerve [44, 75]. However, thermal dose is related to the temperature and time of exposure [106] so this relationship (as opposed to simply force magnitude) would have to be included in the optimization to accurately account for temperature rise.

It is important to bear in mind that these results were obtained through experiments on synthetic bone, and that further experimentation is required to quantify the force reduction that can be achieved in a more clinically-relevant scenario. Temporal bone is denser than the material used in this study (up to $1.87\frac{g}{cm^3}$ vs. $0.80\frac{g}{cm^3}$ [67]). As a result, forces in actual bone will generally be higher than those reported here, which further emphasizes the importance of accounting for bone density and porosity variations. Future research to translate the methodology to actual temporal bone will be directed at evaluating how this method scales up to scenarios that involve higher forces and potentially higher variability in bone composition. This will require exploration of strategies to regulate the coefficients of the cost function, Equation 5.6, that govern the trade off between cutting efficiency and force minimization near the vital structures. It will also be necessary to precisely quantify the performance improvements achievable with respect to CNC-like temporal bone milling.

In addition to reducing cutting forces, the velocity regulation method presented here has the potential to enable time savings during robotic mastoidectomy, particularly for procedures such as the translabyrinthine approach for vestibular schwannoma, in which the surgeon spends several hours manually removing bone before beginning the primary surgical task of tumor resection. Thus, speed improvements during the milling component of the procedure would reduce overall operation time. This procedure time improvement is accomplished by increasing the velocity when the cutting burr goes through either non-critical areas or porous regions of the bone. This time decrease is partially balanced by the slow velocities used when milling close to critical structures. Note that in a clinical scenario this would save more time than was saved in these experiments because a larger percentage of time would be spent milling far from critical structures (in these experiments, a smaller pocket than would typically be required in mastoidectomy was milled - 15 mm x 15 mm x 15 mm vs. approximately 30 mm x 40 mm x 40 mm). Future research should focus on further experimental validation of the approach in cadaver temporal bones to determine whether the advantages seen in this preliminary evaluation translate as expected to biological tissues.

Chapter 6

Drilling Accuracy Evaluation and Error Analysis of a Minimally Invasive Cochlear Implantation System

The remaining chapters in this dissertation focus on minimally invasive cochlear implantation surgery. Specifically, two analyses are performed to better understand potential safety issues with the surgical approach. First, the accuracy of the drilling process is tested and anatomical features that could lead to high risk of drill deviation are identified (Chapter 6). Second, the heat rise near the facial nerve during manual drilling of the minimally invasive tunnel is experimentally evaluated and a safe drilling strategy is developed (Chapter 7).

6.1 Background and Motivation

Given the close proximity of the facial nerve to the desired drill path for the minimally invasive cochlear implantation (CI) approach, sub-millimetric accuracy is required [78]. Even if the drill bit does not contact the nerve, damage could occur due to excessive heat caused by the drilling process [44] so slight deviations towards the nerve could increase the likelihood of thermal damage. Additionally, sub-millimetric accuracy is necessary to successfully gain access to the cochlea and properly insert the CI electrode array into the scala tympani. The drill bits are susceptible to deflections caused by transverse loadings at their tips. The drill bit used in the medial stage, which must pass close to the facial nerve along its path, is particularly error prone due to its small diameter and the fact that it must extend deep into the skull. Thus, the drilling accuracy and potential errors must be understood to ensure patient safety and accurate placement of the CI using this surgical approach.

Several other groups have investigated drilling accuracy in minimally invasive CI surgery. Williamson et al. used the correlation between force and bone density while drilling through the mastoid bone to estimate the location of the drill tip [127]. Their algorithm also provided the surgeon with pre-operative density information to assess the risk of the drill deviating from the planned path. Kobler et al. presented a method for evaluating various types of drill bits for this procedure with respect to bore hole accuracy [68]. They measured the drilling error through bone surrogate materials for various bone surface angles and determined that a drilling strategy employing a gun barrel drill bit for the medial path resulted in better accuracy than twist drill bits and spherical surgical bits.

The work presented in this chapter uses a similar approach to that used in [68] and expands upon this work to investigate the effect of several key factors on the drilling accuracy during minimally invasive CI, which can be used to assess the efficacy of the surgery and define safer drill paths. Specifically, the effects of the following parameters on drilling accuracy are assessed: (1) skull surface angles, or contact angles, at the entry point; (2) the use of bushings to guide the drill and the bushing locations with respect to the trajectory; (3) the composition of bone at the transition between drilling stages (i.e. the point where the lateral hole ends and medial drilling begins); (4) cantilevered length of the medial drill bit when passing through air cells; and (5) angle of bone at the air/bone interface of an air cell along the trajectory. Some of these factors are discussed in a general sense in prior works; however, a thorough investigation has not yet been performed. Finally, the errors measured in this study are discussed in the context of the overall accuracy of the surgical procedure and used to identify anatomical conditions that may lead to unacceptably large error.

6.2 Accuracy Evaluation Methods

6.2.1 Setup and Procedure

The experimental setup was designed to mimic the minimally invasive CI approach using the Microtable while isolating the error caused by deviations in the drill path. In practice, there are multiple additional sources of error, including error from (1) image distortion (2) identification of vital structures and target points, (3) registration, (4) manufacture and assembly of the Microtable, and (5) mounted position of the Microtable relative to the patient. In this work, the intent was to analyze the error in targeting due to drilling through bone with air cells. The presence of mastoid air cells differs considerably among patients based on individual temporal bone anatomy. Thus, it is necessary to evaluate various anatomical effects on this particular component of the surgical error.

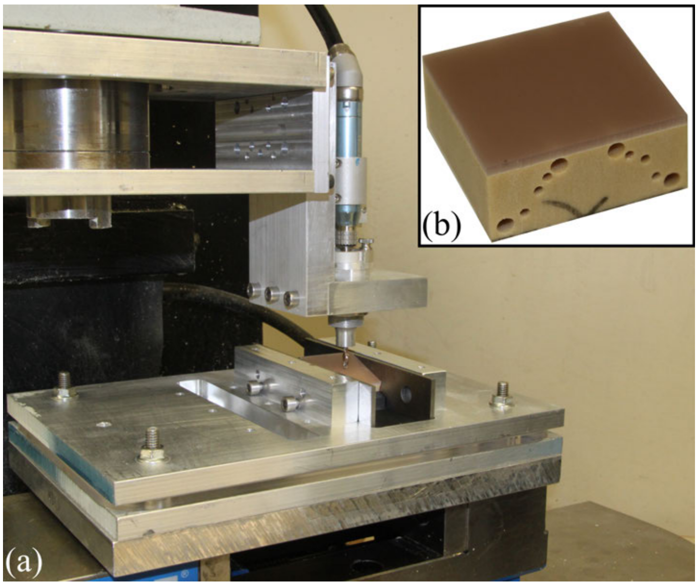

Figure 6.1: (a) Experimental setup showing drill press mounted to bracket on CNC milling machine. (b) Bone surrogate material made from short-fiber-filled epoxy (top layer representing cortical/surface bone) and solid rigid polyurethane foam (bottom layer representing mastoid bone).

Drilling accuracy was measured by making divots in an acrylic sheet that is positioned under a test piece before and after drilling. For the study, the drill press was mounted to a Computer Numeric Control (CNC) milling machine (Exact Jr. 3-axis CNC, Broussard Enterprises, Inc., Santa Fe Springs, California, USA, with a Fagor 8040M CNC controller (Fagor automation, Elk Grove Village, IL)) using a custom bracket (see Figure 6.1). This set up enabled precise positioning and movement of the drill press as the maximum CNC positioning error is 0.0005 in (0.0127 mm). The drill press was placed in the bracket mounted to the CNC machine such that the drill press was along the z-axis of the CNC machine. However, only the x- and y-axes of the CNC were used for positioning the drill press. The z-axis of the CNC was fixed throughout the experiments and the drill press was used for moving the drill up and down. Test blocks made of a bone surrogate material were placed in a jig held by the milling machine vise

An acrylic sheet was placed under the test block and held in place by the vise. For each target point, two pre-drilling divots were made in the acrylic sheet using the drill bit tip with the drill powered off before inserting the test block and performing the drilling. These divots were located 1 mm in either direction of the target point along the y-axis of the CNC. Then the test block was inserted, the drill press moved to the target point (the center of the line segment formed by the two pre-drilling divots), and the two-stage drilling was performed. After completion of the drilling through the test block, the drill was turned off and the tip of the drill bit pushed into the acrylic sheet to make another divot (see Figure 6.2). The jig held the test block slightly above the acrylic sheet because there is an air gap between the end of the drill path and the cochlea in a clinical case. This existence of space also allowed for the drilling to stop in this gap prior to making the post-drilling divot.

6.2.2 Drill Press System

A two-stage drilling approach is used for this technique: a pilot hole through the lateral portion of the mastoid is made with a larger drill bit and a narrower drill bit is used medially to drill farther towards the cochlea through the facial recess. The narrow drill bit is required in the medial portion of the trajectory to avoid damage to critical anatomy; however, using this size drill bit for the entire trajectory would lead to large deflections. The two drill bits used in these experiments were a 3.8 mm

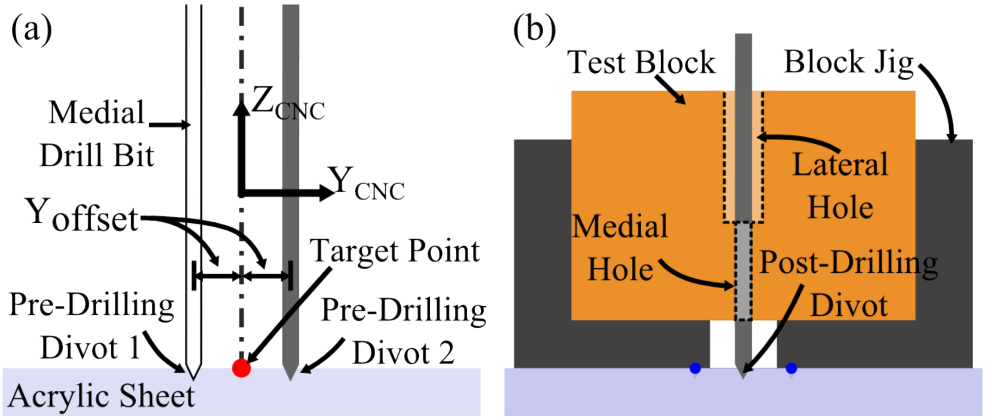

Figure 6.2: Steps in the experimental procedure for a single targeting trial: (a) Creation of pre-drilling divots. The drill press is moved along the negative y-axis of the CNC milling machine such that the y-coordinate of CNC, Y_{CNC}, is Y_{Offset}. The drill is moved down along the z-axis such that the drill tip makes a divot in the Acrylic sheet. This divot is called the Pre-Drilling Divot 1. The same process is repeated by moving the drill press along the positive y-axis to $Y_{CNC} = Y_{Offset}$ to make the Pre-Drilling Divot 2, (b) Creation of the post-drilling divot. The jig and test block is inserted and the drill press is moved to $Y_{CNC} = 0$. Drilling is performed through the test block. With the drill turned off, the drill is moved down into acrylic to make Post-Drilling Divot.

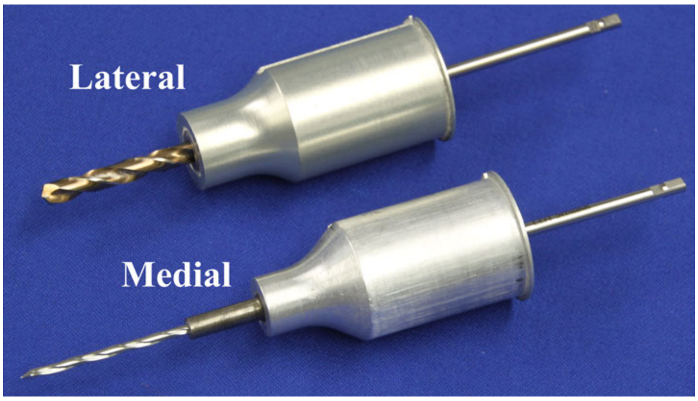

Figure 6.3: Lateral (top) and medial (bottom) drill bits and bushings used for minimally invasive cochlear implantation.

twist drill bit made from cobalt steel for the lateral stage and a 1.59 mm CingleBit^{TM} drill bit made from hardened stainless steel for the medial stage (Orchid Orthopedic Solutions, Holt, MI, USA). For each drill bit there was also a bushing assembly that mounted to the Microtable to control the movement of the drill bits. Both drill bits and bushings are shown in Figure 6.3. For the experiments, the drill press mounted to the CNC milling machine using the same coupling used to mount it to the Microtable. A surgical drill (Anspach eMax 2, Synthes, Inc., West Chester, PA, USA) was fixed in a clamp on the linear slide of the drill press with its length calibrated so that it drilled to the correct depth.

6.2.3 Bone Surrogate Materials

The test blocks (Figure 6.1b) were Sawbones biomechanical test materials (Pacific Research Laboratories, Inc., Vashon Island, Washington, USA). The temporal bone consists of a thin layer of dense cortical bone at the surface and a mastoid bone region with air cells deeper into the skull. Hence, a custom laminated block was manufactured consisting of a 3 mm top layer made from short fiber filled epoxy representing the cortical bone and a 12-25 mm bottom layer of solid rigid polyurethane foam (ρ = 50 lb/ft^2) representing the mastoid bone. This material was previously used as a temporal bone surrogate in studies by Kobler et al [67, 68]. Holes (2-3.5 mm in diameter) were drilled in the bottom layer of the test blocks to represent the mastoid air cells present in the temporal bone. Two different patterns were chosen for the locations of the air cells with the difference between the two being the composition of bone at the location where the lateral drilling ends (air cell versus solid bone). The size of the air cells were chosen based on a review of clinical CT data. The air cell patterns are not intended to represent specific patient anatomy; however, it has been observed in clinical cases that the lateral hole ends in an air cell for some patients and solid bone for others. Thus, this characteristic is differentiated in the two patterns.

6.2.4 Divot Localization and Error Calculation

The target point was defined as the mid-point of the line segment connecting the two pre-drilling divots. The error was therefore the vector displacement between this target and the divot made after drilling (see Figure 6.4). An image of the three divots was acquired using an optical microscope and then the divots were localized in the image using a custom program written in Matlab (The MathWorks, Inc., Natick, MA, USA). A calibration grid slide (Thorlabs, Inc, Newton, NJ, USA, part no. R1L3S3P) was placed on the acrylic sheet during the acquisition of the microscope image and various points on the grid were selected in software to calculate the scale of the image.

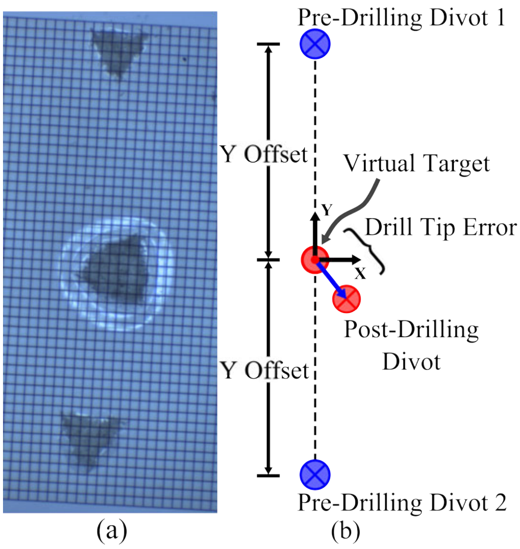

Figure 6.4: (a) Photograph pre-drilling and post-drilling divots after drilling. (b) Schematic of error calculation. The virtual target is defined as the midpoint of the two pre-drilling divots.

6.2.5 Validation of Method

A control study with 12 trials was performed to validate the measurement method. The acrylic sheet was held in place with the vise, and no test block was used in this control study. For each trial, the following four steps were performed: (1) The CNC machine was moved to desired position along the x- and y-axes for the trajectory and x and y values were zeroed, (2) With x-axis of the CNC machine held constant at zero, two pre-drilling divots were made as described earlier by moving the CNC machine along the y-axis to -Yoffset and +Yoffset positions and moving the drill in the drill press down to make the divots. (3) A target divot was made by moving the CNC machine to y = 0 (x still at zero). (4) The error in the target divot location was calculated as described above. All the divots were made with the medial drill bit. The calculated error for these control trials represents a combination of the CNC positioning error, error in localizing the pre-drilling divots in the image and calculation of the target point based on these locations, and error localizing the post-drilling divot. If the localization of the divots was perfect, the errors measured in these control trials would fall within the tolerance of the CNC. The control study trials (n=12) had a mean error of 0.012 mm ± 0.008 mm, which is slightly outside the positioning tolerance of the CNC indicating that there is a small amount of error between the various error sources described above. However, the drill tip errors measured in these trials are considerably lower than the errors in the drilling experiments and the required accuracy of the surgery confirming that this is a suitable method of measuring drill deviation for this study. Additional trials were performed to check for errors that may result from repeated mounting and removal of the drill press from the Microtable mount (e.g. between trials and when changing drill bits). The errors observed in these additional trials were also inconsequential.

6.3 Drilling Accuracy Experiments

Two groups of drilling experiments were performed as part of this study. First, the full, two-stage drilling was completed on the laminated test blocks to assess the drilling accuracy and examine the effects of various clinical parameters on drilling accuracy. Next, experiments were performed to further isolate the drilling error at individual bone contact points along the medial drill path (air/bone interfaces at air cells) to identify specific anatomical features within the mastoid that may influence drilling accuracy.

6.3.1 Two-Stage Drilling Experiments

Data from prior clinical studies of the minimally invasive image-guided CI system [74] were used to select drilling parameters used in these experiments, including the depth of drilling for the lateral and medial drilling, positioning of drill guide bushings, angle of drill relative to skull surface, and location of the cochlea relative to the end of the drilling path (Table 6.1). In the experiments, three variables were adjusted: angle of drill relative to the skull surface, location of bushings relative to skull surface, and composition of bone at the end of the lateral hole (solid bone vs. air cell). Distance between target point (cochlea), where we wanted to measure the error, and the end of the medial drilling was fairly consistent among patients and therefore kept constant in these experiments. Figure 6.5 provides a schematic of the test setup with the various parameters displayed.

A total of ten combinations of parameters were tested with twelve trials per set. Statistical analysis was performed on the error data to determine which parameters significantly affected the drilling accuracy. The data for each set of parameters was first checked for normality and then comparative tests were used to determine if the means were significantly different. Additionally, the results from these experiments can be used, along with an estimate of other sources of error in the system, to estimate the overall root mean square (RMS) error of the procedure, $e_{total}(RMS)$. In a prior study [79], the free space positioning error, $e_{pos}(RMS)$, resulting from image

Table 6.1: Parameters for accuracy evaluation (two-stage drilling) experiments.

Parameter	**Average from Clinical Data**	**Value(s) used in Experiments**
Drill depth for lateral drilling	13.0 mm	13.0 mm
Drill depth for medial drilling	9.9 mm	10.0 mm
Angle of drill relative to skull surface at point of entry	40°	00°, 20°, 40°, 60°
Distance of the base of the bushing above skull surface along trajectory[a]	Lateral: +9.3 mm Medial: -2.7 mm	Lateral: +6, +9, +14 mm Medial: -6, -3, +2 mm
Composition of bone when the lateral drilling ends	Solid bone or air cell	Solid bone or air cell
Drill Speed	20,000-80,000 rpm	30,000 rpm

[a] A positive value indicates that the bushing ends above the skull surface; a negative value indicates that the bushing is within the temporal bone.

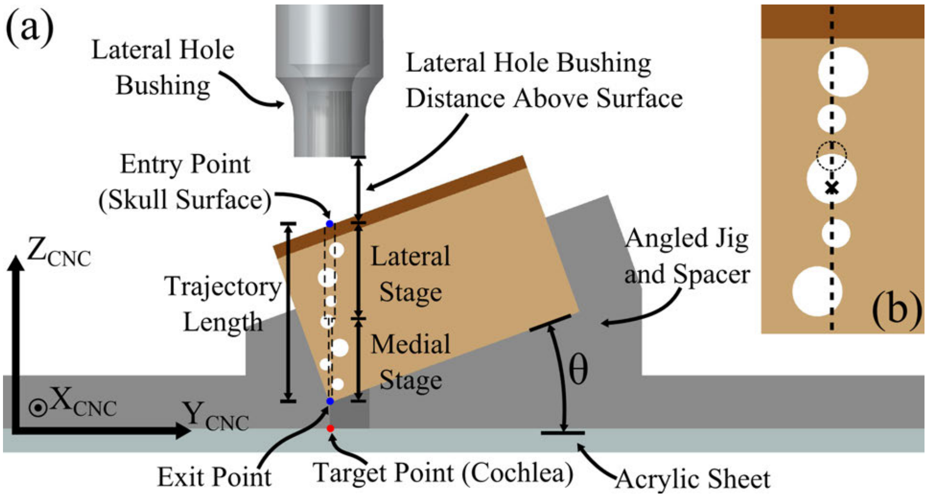

Figure 6.5: (a) Schematic of test setup indicating the various parameters used in the experiments. The length of drill path and location of target point relative to the skull surface were held constant. The angle of the surface, height of bushings, and composition of bone at the end of the lateral hole were varied. Note: the lateral bushing is shown in this figure. During the medial drilling stage, a different guide bushing is used, which extends into the hole created by the lateral drilling. (b) Close-up of the mastoid air cell pattern for the case of the lateral stage ending in an air cell. For the case of the lateral stage ending in solid bone, the large middle air cell is replaced with a smaller air cell located at a shallower depth (dashed line).

processing, Microtable manufacture, and Microtable assembly errors was measured. Assuming both error sources are normally distributed, the RMS errors for free space positioning and drilling can be added in quadrature to calculate total RMS error.

$$e_{total}(RMS) = \sqrt{e_{pos}^2(RMS) + e_{drill}^2(RMS)} \tag{6.1}$$

where the $e_{drill}(RMS)$ value was measured by the two-stage drilling experiments. The RMS errors of the free space positioning and drilling errors are given by $e_{pos}(RMS) = \sqrt{\mu_{pos}^2 + \sigma_{pos}^2}$ and $e_{drill}(RMS) = \sqrt{\mu_{drill}^2 + \sigma_{drill}^2}$, respectively.

6.3.2 Medial Drilling Experiments

A major contribution to the drill deviation error was assumed to be due to the deflection of the medial drill bit since it is narrower and is used to drill deeper than the lateral drill bit. This effect has been observed in some of the cadaveric testing where the lateral hole was aligned well to the desired trajectory, but the end of the medial hole missed the target. Therefore, experiments to isolate the error during the medial drilling were performed. Most of the deflection of the drill tip, which leads to inaccurate hole placement, occurs at the initial penetration of the material [82]. For the case of solid, homogeneous material, this penetration is at the surface of the material only. In the mastoid, the presence of air cells results in many air/bone interfaces along the path and thus numerous penetration (deflection) points. The overall drilling error is a result of the combination of these numerous sources of error. This overall error is captured in the first group of experiments discussed above.

The purpose of this second group of experiments is to identify the parameters that lead to large errors during the medial stage of drilling. Again, various angles were tested ($0° - 75°$) as well as different cantilevered lengths of the drill bit (i.e. length of drill bit extended out from bushing when contacting bone). The same protocol described above in the Experimental Methods section was used for these trials with the exceptions that drilling was performed only using the medial drill bit and thinner blocks made of only solid rigid polyurethane foam (representing mastoid region only) were used for this study.

6.4 Experimental Results and Discussion

6.4.1 Two-Stage Drilling Experiments

The experimental results for the ten cases tested in the first group of experiments is provided in Table 6.2 and scatter plots for this data are given in Figure 6.6. The range of errors meets the accuracy requirements of the surgery; however, there are some parameters sets that lead to larger errors that, when combined with the other sources of error in the surgery, could lead to insufficient targeting accuracy. Specifically, combining the RMS errors observed in these experiments (0.039-0.247 mm) with the free space positioning data ($e_{pos}(RMS) = 0.40$ mm) [79], yields an overall RMS error of 0.41-0.48 mm. The results for the different parameters are discussed in the sections below. Note that in all trials, the block was angled such that the positive y-axis of the CNC machine pointed up the slope.

Table 6.2: Drilling accuracy data for two-stage drilling experiments.

		Error Magnitude (mm)			**X-Y Position Error (mm)**	
Case[a]	**Parameters**[b]	$\mu \pm \sigma$	**RMS**	**Max**	X, $\mu \pm \sigma$	Y, $\mu \pm \sigma$
1	0° / Bone / 9 mm	0.036±0.015	0.039	0.064	+0.019±0.018	+0.012±0.028
2	20° / Bone / 9 mm	0.074±0.044	0.086	0.126	+0.003±0.021	−0.068±0.048
3	40° / Bone / 9 mm	0.074±0.044	0.086	0.126	+0.003±0.021	−0.068±0.048
4	60° / Bone / 9 mm	0.093±0.063	0.112	0.235	+0.017±0.036	+0.060±0.089
5	0° / Air / 9 mm	0.070±0.021	0.073	0.100	−0.039±0.032	−0.049±0.022
6	20° / Air / 9 mm	0.153±0.071	0.169	0.258	−0.101±0.036	−0.106±0.076
7	40° / Air / 9 mm	0.178±0.054	0.186	0.231	−0.052±0.039	−0.166±0.051
8	60° / Air / 9 mm	0.072±0.045	0.085	0.167	−0.018±0.057	−0.031±0.055
9	40° / Air / 14 mm	0.241±0.055	0.247	0.320	−0.058±0.017	−0.234±0.055
10	40° / Air / 6 mm	0.170±0.060	0.180	0.259	−0.020±0.024	−0.168±0.058

[a] 12 trials were performed for each case.

[b] Parameters are Angle of drill relative to skull surface at entry point / composition of bone at end of lateral drilling / height of lateral bushing from skull surface. The height of the medial bushing is 12 mm deeper than the lateral bushing (e.g. 3 mm inside skull when lateral bushing is 9 mm from skull surface).

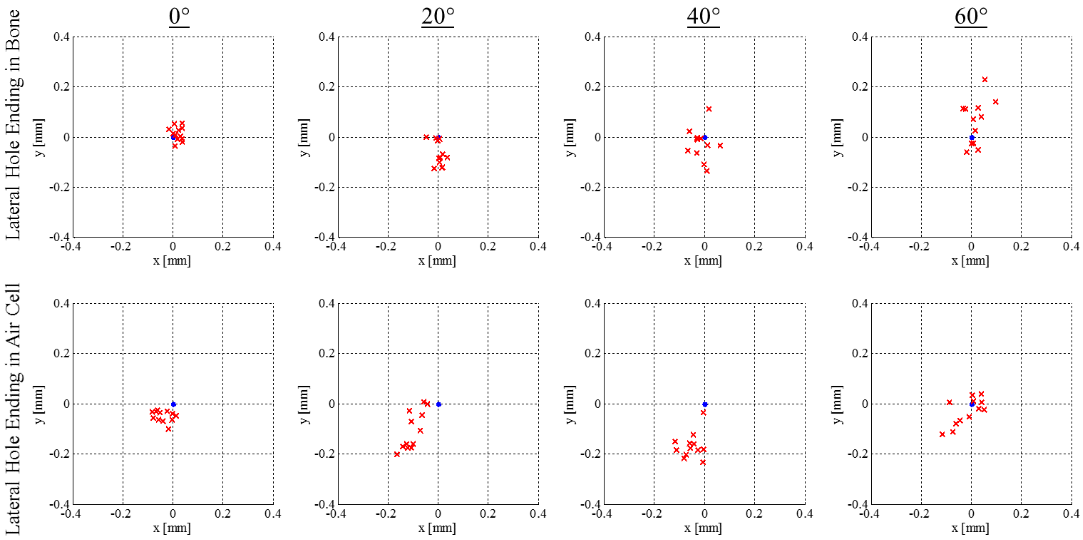

Figure 6.6: Scatter plots for the eight experimental cases comparing skull surface angle as well as lateral stage stopping location. The target point for each plot is at the origin.

Angle of skull surface

The effect of the angle of the drill shaft relative to the skull surface was examined for both lateral drilling ending locations with a constant height for the bushings (solid bone: case 1 vs. 2 vs. 3 vs. 4, air cell: case 5 vs. 6 vs. 7 vs. 8). For both sequences, an analysis of variance (ANOVA) test indicated a significant difference in the means between the groups. Subsequent comparisons were performed between the individual groups using the Bonferroni correction factor, which indicated that only some parameter sets were significantly different. For the cases in which the lateral drilling ends in solid bone, the difference between the 0° and 60° cases were statistically significant at the 5 percent level (i.e. $p < 0.05$). For the cases in which the lateral hole stops in air, the results of the 20° and 40° cases were statistically different from the 0° case ($p < 0.05$).

This data indicates that there is some effect of drill/bone angle on the drilling accuracy; however, it is difficult to determine the extent of the effect since the results are not consistent. This is likely due to the fact that there are many other factors influencing the drilling accuracy, most notably the location and size of the air cells in the test blocks. Different deflections at the surface lead to the medial trajectory passing through air cells at different points and thus leading to a range of deflections deeper along the trajectory. In particular, the 60° case for the lateral hole stopping in air does not follow the general trend of the rest of the data. Looking at the test blocks after drilling indicates that the location of the drill path with respect to the final air cell in the test block was slightly offset compared to the other blocks, which may have caused a different deflection at this point in the trajectory. It is clear that steeper angles at the skull surface negatively affects the drilling accuracy but this is only one component of the drilling error and must be considered with the parameters along the medial stage as discussed in more detail in the Medial Drilling Experiments section below.

Composition of bone at end of lateral hole

For each drill angle, a comparison was made between the case in which the lateral stage ends in solid bone and the lateral hole ends in an air cell (cases 1 vs. 5, 2 vs. 6, 3 vs. 7, 4 vs. 8) using a two-sample t-test. The difference between results (bone vs. air cell stopping point) for the 0°, 20°, and 40° cases are statistically significant ($p < 0.001$, $p = 0.003$ and $p < 0.001$, for angles of 0°, 20°, and 40°, respectively) and all indicate that drill deviation error is greater when the lateral stage ends in an air cell. The difference in results for the 60° case is not statistically significant at the 5 percent level. This may be caused by the medial bit passing through a different part of a deeper air cell as discussed above.

These results show that higher accuracy can be achieved by planning the drill trajectory such that the lateral drilling ends in solid bone. This finding is likely due to the fact that when the lateral stage stops in an air cell, the medial drill bit is cantilevered out from the bushing a longer distance before initially contacting bone. Therefore any transverse force on the tip of the drill results in a larger bending moment on the drill bit shaft. Additionally, when the lateral hole ends in solid bone, the shape of the drill bit provides a conical shape at the end of the hole, which helps to center the medial drill bit.

Bushing location relative to skull surface

Three different bushing locations were tested (note: the medial bushing extends 12 mm beyond the lateral bushing so raising/lowering one affects the other the same amount). In each case, the bone was fixed at an angle of 40° relative to the drill and the lateral hole was planned to end in an air cell (cases 7, 9, and 10). An ANOVA test indicated a difference between the group means and subsequent individual comparisons with Bonferroni correction performed. The error difference between the two cases with the medial bushing located inside the skull (Case 7 and 10) is not statistically significant. However, there is a statistical significance between these two cases and the case for which the medial bushing is located outside of the skull ($p = 0.006$ for Case 10 vs. Case 9 and $p = 0.009$ for Case 7 vs. Case 9). This implies that there will be a decrease in accuracy when the Microtable is placed higher above the skull surface, particularly when the medial bushing does not reach the skull surface. This agrees with the finding that accuracy decreases when the lateral drilling ends in an air cell. In both situations, the longer cantilevered length of the narrow medial drill bit leads to more deflection.

6.4.2 Medial Drilling Experiments

The results for the medial drilling experiments are provided in Table 6.3. In these experiments, the errors increased along the direction of the angle of the block and with increase in cantilevered length of the medial drill bit as expected. For most of the parameter sets, the errors were very low relative to the positional accuracy required for successful surgery; however, it is important to note that this error represents the deflection at one point along the medial trajectory. In a typical trajectory there are several deflection points so it is possible for the cumulative deflection to result in more significant drilling error. These results are discussed in more detail in the following paragraphs.

The medial drill deflection increased significantly for angles of 45° and greater compared to the 0°-30° cases. The data for the three cases with lower angles are very similar and, accounting for the experimental error and number of trials, can be considered approximately equal for the purpose of predicting deflections in surgery. The magnitude of these deflections is considerably low compared to the required positional accuracy and would only need to be considered if the addition of other

Table 6.3: Drilling accuracy data for medial drilling experiments.

Parameters[a,b]	**Error Magnitude (mm)**			**X-Y Position Error (mm)**	
	$\mu \pm \sigma$	**RMS**	**Max**	X, $\mu \pm \sigma$	Y, $\mu \pm \sigma$
0° / 6 mm	0.035 ± 0.011	0.037	0.060	-0.031 ± 0.014	$+0.012 \pm 0.007$
15° / 6 mm	0.027 ± 0.009	0.029	0.042	-0.019 ± 0.011	$+0.094 \pm 0.017$
30° / 6 mm	0.028 ± 0.021	0.035	0.071	-0.023 ± 0.024	$+0.003 \pm 0.012$
45° / 6 mm	0.053 ± 0.023	0.058	0.090	-0.028 ± 0.021	-0.041 ± 0.020
60° / 6 mm	0.098 ± 0.036	0.105	0.166	-0.056 ± 0.029	-0.079 ± 0.028
75° / 6 mm	0.116 ± 0.011	0.117	0.131	-0.037 ± 0.021	-0.109 ± 0.012
45° / 3 mm	0.072 ± 0.017	0.074	0.104	-0.052 ± 0.022	-0.046 ± 0.011
45° / 9 mm	0.117 ± 0.043	0.125	0.185	-0.054 ± 0.022	-0.103 ± 0.041

[a] 12 trials were performed for each case.

[b] Parameters are angle of bone at contact point / cantilevered length of drill bit from end of bushing to contact point.

factors was likely to result in higher error (e.g. presence of large air cell or bushing placement that leads to long cantilevered length of drill bit). Higher angles, on the other hand, (45° and above) may result in much higher errors and affect the success of the surgery, especially when coupled with other parameters that lead to higher errors. The errors in these trials were primarily directed along the negative y-axis in scatter plots, which is the downward direction of the angled blocks, and the negative x-axis (Figure 6.7). The angle of the block causes the bit to first contact only part of the bone, which results in an unbalance of the forces between the drill bit flutes and the material. The direction of the cumulative force is dependent on the spindle direction of the drill. The drill bit spins clockwise (as viewed looking down the drill shaft towards the tip) in this system so the error is directed in the negative x-direction

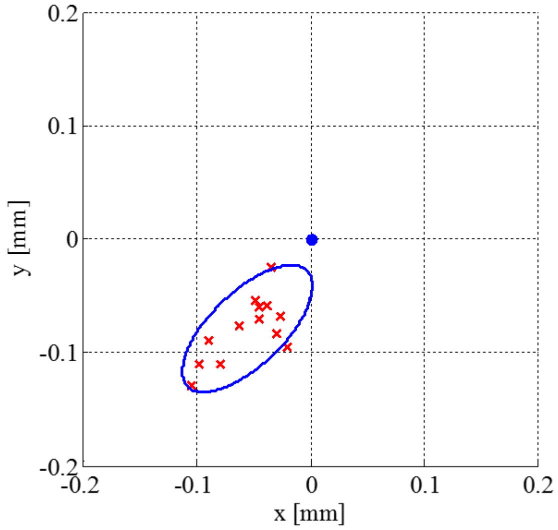

Figure 6.7: Scatter plot for medial drilling error at a single bone contact point with the bone at an angle of 60^o. The ellipse around the data encloses two standard deviations along the principal axes.

as well as down the angled face.

Additional experiments comparing the cantilevered length of the drill bit at the bone contact point indicated that the accuracy decreases with longer extension of the medial drill bit. These experiments were performed with a bone angle of 45°. The error increased significantly for a cantilevered length of 9 mm as compared to 3 mm and 6 mm lengths. The error was primarily in the same direction as the higher angle trials discussed above. For most points along the medial trajectory the cantilevered length will be low since the bone serves as a constraint similar to the bushings; however, for large air cells and the initial contact point, the drill bit may be extended up to 10 mm. These longer extensions must be accounted for when predicting medial drill deflection.

6.5 Discussion

In this chapter, a method for evaluating the drilling accuracy of a minimally invasive CI surgical technique was presented. The drilling accuracy of this approach was evaluated in bone surrogate material and found to be within the tolerance of the procedure and within the range seen in cadaveric and clinical trials for most parameter sets; however, it is clear that specific anatomical features can lead to inaccurate drilling and must be accounted for when planning the surgery, especially since slight deviations could result in excessive heat at the nerve. Furthermore, these errors must be considered in the context of other error sources. Given the overall RMS error range of 0.41-0.48 mm predicted by combining the data from the prior free space accuracy study [79] and this work, it is especially important to avoid certain trajectories and keep the expected error within that range.

The material used in this study is similar to bone; however, it is obviously not a perfect substitute and there can be large variations in the properties of bone among patients. Thus, these results are best used as a guide to determining a range of possible errors and identifying which factors affect the drilling accuracy during surgery. Specifically, it is clear that the lateral drilling stage should end in solid bone. If this is not possible given the patients anatomy, particular attention should be paid to minimize the cantilevered length of the medial bit when it first contacts bone and avoid drilling trajectories that lead to steep air/bone contact angles along the medial stage. The use of and position of the guide bushings also play a significant role in drilling accuracy and is likely the primary reason for the increased accuracy observed in this study compared to the work of Kobler at al., as the authors of that paper also hypothesized. Based on the results of this study, the most accurate percutaneous drilling approach should employ guide bushings and design the apparatus such that they are placed as deep as possible in the bone.

The results of this study help explain the reason for the inaccurate placement of an electrode array in a previous cadaveric trial performed with this system [105]. The electrode was inserted into the scala vestibuli subcomponent of the cochlea instead of the scala tympani as had been planned. The pre-operative CT scan of this cadaveric temporal bone specimen along with the planned drilling trajectory is shown in Figure 6.8. The lateral stage of the trajectory ended in a very large air cell causing the medial drill bit to be extended quite far from the bushing at the initial contact point. The angle at this initial contact point was also very steep. This trial would be best modeled by parameter set 10 from the two-stage drilling experiments. Additionally, the results from the medial drilling experiments with higher angles at the air/bone contact point and long cantilevered length of the medial drill bit helps to explain the large error. These factors likely contributed to a deflection from the planned path that resulted in the deviation of the drill bit into the scala vestibuli. Using the information learned from this study, an alternative trajectory could be planned for future cases in which the patient anatomy indicates a possible large deflection. In this particular case, a shallower lateral stage would allow the lateral hole to center the medial drill bit and limit the cantilevered length of this bit along the deeper portion of the trajectory. A deeper lateral stage would also help center the medial bit and

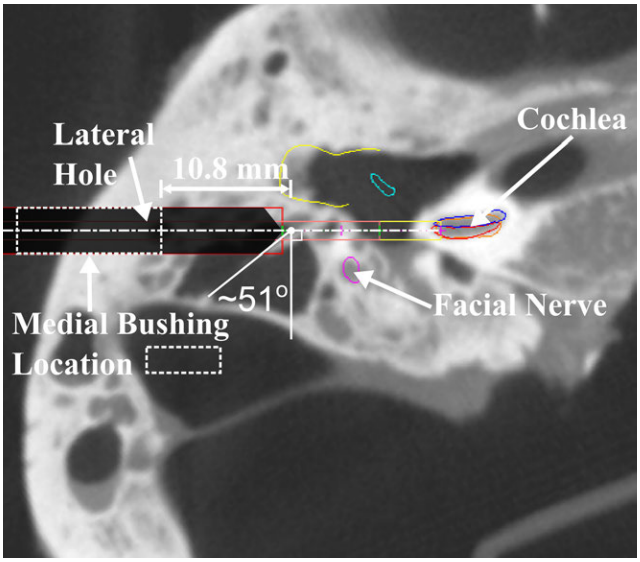

Figure 6.8: Pre-operative scan from a prior cadaver trial in which the drill path deviated from the target path and the electrode was inserted into the scala vestibuli instead of the scala tympani. The data presented in this study explains the reason for the large drilling error for this case. The medial drill extended 10.8 mm from the bushing before first contacting bone and the large air cell at the end of the lateral stage resulted in a steep initial contact angle of 51°. The dashed lines in this figure represent the location of the medial bushing.

would remove the bone in the area of the steep angle.

The simplest way to use the results of this study to improve the planning for future clinical cases would be to implement safety checks while planning the drill path such that anatomical conditions that would lead to larger deflections are identified. A path could then be selected that avoided any of these high risk conditions. Furthermore, the likelihood that the drill would deviate significantly off course could be considered by the surgeon when deciding whether to use this minimally invasive CI approach or the traditional surgical approach.

Chapter 7

Thermal Analysis and Reduced Heat Generation During Guided Manual Drilling for Minimally Invasive Cochlear Implantation

This chapter provides an analysis of the heat generated while drilling the narrow tunnel for minimally invasive cochlear implantation surgery. The analysis results in a safer approach for the minimally invasive technique that includes a pre-operative risk assessment and an improved drilling strategy to reduce heat generation near the facial nerve.

7.1 Background and Motivation

The drilling of bone results in a temperature rise in surrounding tissue as the mechanical energy required to cut the bone is transferred to thermal energy. This temperature rise is particularly important when the tool is removing bone in close proximity to vital anatomy (e.g. nerves) as high temperatures can result in permanent damage [1,16,84]. As discussed in Chapter 1, prior clinical trials using the minimally invasive cochlear implantation (CI) system developed at Vanderbilt resulted in temporary facial nerve paralysis in one patient [75], which was attributed to heat-related injury secondary to drilling nearby bone. The location of the nerves within the temporal bone relative to the cochlea dictate that the drill must pass in close proximity in order to gain the required access for optimal CI electrode insertion (as low as 0.5 mm for some patients). Thus, further investigation of the temperature rise while drilling through the temporal bone and the associated risk to the facial nerve is critical for clinical translation of this approach.

The fundamentals of bone drilling have been studied extensively for orthopedic procedures (see [13] or [98] for a review of the literature). The main objective of much of this prior work is to minimize the thermal damage to adjacent bone and associated thermal osteonecrosis (i.e. loss of blood supply) to the bone that results in death of the bone tissue. Heat is generated by two primary modes: the shearing of bone at the cutting blade and friction between the tool and bone (especially for higher rotational speeds). The effects of different drilling parameters (e.g. drill rotational speed, feed rate, axial force) on this temperature rise have been examined but the results reported in the literature vary substantially and thus do not provide consistent guidelines for determining “optimal” drilling parameters. Specific drill bit geometry and material properties of bone (e.g. density, specific heat, thermal conductivity) also impact the amount of heat generated. Thus, there are no ideal sets of parameters; instead, parameters must be determined through modeling and/or experimentation for a particular system along with some general recommendations from prior literature.

Another factor to consider when evaluating drilling parameters and the associated heat rise is whether the drilling is automated or performed manually. This is a key difference between the minimally invasive CI systems proposed to date. Several systems (e.g. [79], [70], and [65]) require the surgeon to manually advance the surgical drill along a linear path that is constrained by the patient-specific stereotactic frame, robot, or adjustable mechanism. In other systems (e.g. [87], [9], and [12]), the robot performs the alignment of the drill and the advancement along the desired linear trajectory through the bone. There are advantages and disadvantages with each method. The guided manual drilling enables a simpler overall surgical system and keeps the surgeon more directly involved with the drilling process, which better utilizes his/her expertise and may facilitate earlier adoption by clinicians. The automated drilling approach provides more control over the drilling parameters (e.g. feed rate, drilling intervals) and supports the integration of additional sensors (e.g. force/torque sensors), which enables optimization of the drilling process and redundant safety monitoring.

Feldmann et al. examined the effect of temperature rise secondary to drilling for minimally invasive CI surgery using the automated drilling approach [44]. They tested their previously developed minimally invasive CI robotic system [11,12] on live sheep and measured the temperature at a point several millimeters from the drilling trajectory using a thermocouple inserted into the bone. Their experimental data was then used to calibrate a computed tomography (CT) image-based thermal model in which the heat generated at the drill tip was modeled as a moving point heat source. The power of the heat source was varied according to the bone density along the path and the bone through which the heat spread towards the nerve was considered to be homogeneous with material constants similar to those of compact bone. After the model parameters were calibrated, the temperature at any point in the bone (at any time) could be computed. Temperatures at a distance of 0.5 mm from the edge of the drill path were calculated, which represents the closest distance at which the drill is likely to pass the facial nerve in a clinical case. The results indicated that the facial nerve reached potentially dangerous temperatures in several of the trials. However, it is important to note (as the authors explain) that the drilling parameters were not optimized for minimizing temperature. Furthermore, additional safeguards (e.g. irrigation, planning of trajectories through more porous bone) could potentially reduce the temperature rise in the surrounding tissue.

The recent results from Labadie et al. [75] and Feldmann et al. [44] indicate that controlling the heat generated during drilling in minimally invasive CI surgery is critical for the approach to be a viable alternative to the current state of the art. The difference between the approaches for drilling the minimally invasive tunnel discussed above (manual vs. automated drill advancement) is particularly relevant for the reduction of heat and must be considered when evaluating the safety of the approach. It is impossible to control the manual advancement of the drill with precision and consistency comparable to that of automated advancement; however, there are other factors motivating the use of manual drill advancement (as described above). Thus, further investigation is needed to develop a procedure for performing the manual drilling for minimally invasive CI in a manner that does not result in high temperatures near the nerves, thereby enabling safe execution of the surgery. The purpose of the work of this chapter is to develop a methodology for performing this procedure such that the risk of causing heat-related damage to the facial nerve is minimized despite patient anatomical variations and differing levels of surgeon experience with the approach.

Included in this methodology is a pre-operative step in which individual patient risk is assessed based on bone density and position of vital anatomy with respect to the planned drill path. This assessment can be used to determine if a particular patient is a candidate for the minimally invasive approach or if the patient should undergo the conventional approach. An analysis of the manual drilling process is then used to develop an improved surgical drilling strategy. Finally, an experimental setup for the thermal monitoring of the bone near the facial nerve is presented and the revised drilling strategy is tested on fresh cadaver temporal bones.

7.2 Surgical Approach

This section describes the proposed surgical approach for minimally invasive CI surgery using the previously developed Microtable microstereotactic frame to guide a surgical drill [7, 75, 79]. There are two primary components that contribute to safe execution of the procedure: (1) accounting for patient variability and specific anatomical conditions that could yield unsafe temperatures and (2) safe, consistent execution of the drilling near the facial nerve. Figure 7.1 provides a flow chart of the surgical workflow. A pre-operative risk assessment, described in the first part of this section, is used to decide if a patient should undergo the minimally invasive or the traditional approach to CI surgery. The second part of this section describes the development of the drilling strategy used for candidates of the minimally invasive approach.

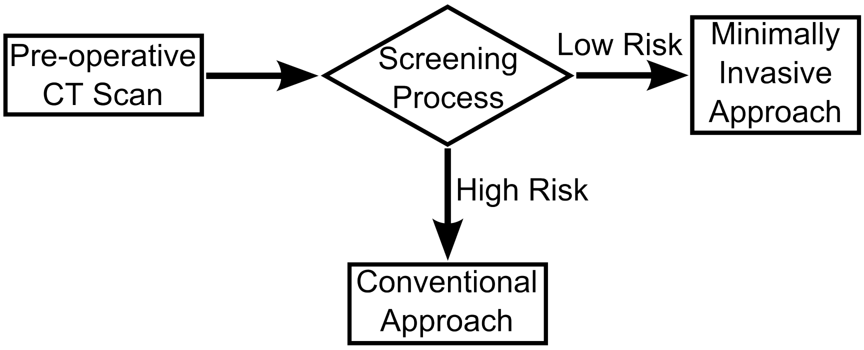

Figure 7.1: Proposed surgical workflow for cochlear implantation (CI) surgery. Patients are screened using their pre-operative CT scan to determine if they at high risk for thermal damage during the minimally invasive approach. High risk patients undergo the traditional approach to CI surgery.

7.2.1 Pre-Operative Patient Screening and Exclusion

Given the variability of human temporal bone anatomy and the temperature measurements recorded in live sheep by Feldmann et al. [44], it is clear that some patients are at higher risk of excessive heat rise near the facial nerve based on their specific anatomy. For example, dense bone conducts heat better than less dense bone or air. While it is likely that the minimally invasive approach could be performed safely on all patients with an appropriate drilling strategy, the manual drill advancement introduces some inconsistency which could lead to higher temperatures for some patients. Thus, patients that are high risk given the composition of their temporal bone should undergo the traditional approach for CI surgery, especially while the minimally invasive approach is in its infancy.

A precise temperature prediction cannot be made from the preoperative data since there will be variability in how the manual drill advancement is performed and effective irrigation at the drilling site is inconsistent. Instead, it is possible to assess the relative risk between patients. Then, if only lower risk patients are considered candidates for the minimally invasive approach, variations in drilling and irrigation that lead to higher temperatures are less likely to result in unsafe temperatures at the nerve. This risk can be estimated from the pre-operative CT scan by examining the bone density along the planned drill path near the facial nerve, as well as the proximity of the facial nerve to the planned drill path and the bone density between the planned path and the nerve. To predict the risk of high temperature at the nerve it is important to consider two factors: (1) the amount of heat generated by the drill as it creates the minimally invasive tunnel and (2) how much of that heat spreads to the nerve. The two preoperative risk metrics described below provide an assessment of these two factors and give the surgeon a basis for deciding whether the patient should undergo the minimally invasive approach.

Bone Intensity Along the Planned Drill Path

The amount of heat generated at a given point along the path is a function of the process parameters (e.g. linear velocity, spindle speed, etc.) as well as the bone density at that point [44], which can be approximated by the image intensity in Hounsfield Units (HU) (see Figure 7.2). Since bone has a low thermal conductivity (0.55 W/mK [25]), only the region of bone along the path near the facial nerve needs to be considered in this analysis and heat generated earlier along the path does not result in a high temperature near the nerve. Based on preliminary thermal measurements of bone drilling, the region considered is 3 mm lateral and medial to

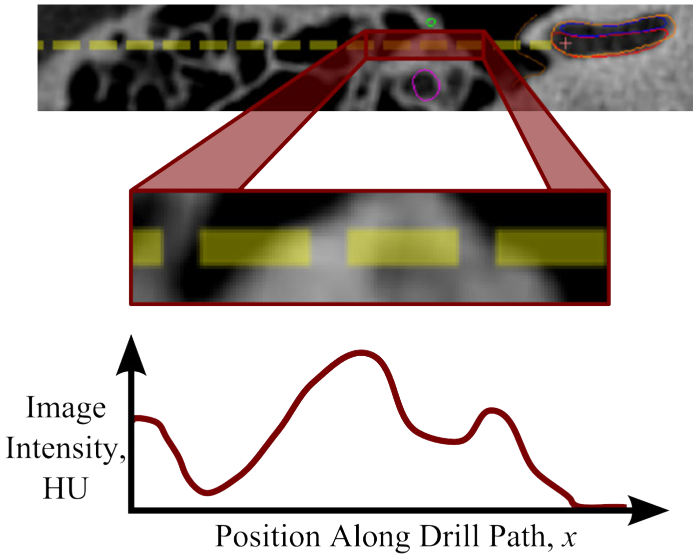

Figure 7.2: One of the risk metrics used to evaluate individual patient risk is the integral of the bone intensity along the drill path. A schematic of this metric is shown here. The intensity in Hounsfield units is examined in the area in which the drill path passes close to the facial nerve.

the point at which the drill passes closest to the nerve. A simple integral of bone intensity in this critical region can be calculated as:

$$I_{crit} = \int_{p_{FN}-3}^{p_{FN}+3} HU(x)dx \tag{7.1}$$

where x is the distance along the planned drill path, and p_{FN} is the point on the path at which the drill passes closest to the nerve. To account for the fact that heat generated closer to the nerve has a greater effect on the temperature of the nerve, the integral can be weighted according to this distance:

$$I_{crit} = \frac{1}{K^{\overline{d_{FN}}}} \int_{p_{FN}-3}^{p_{FN}+3} HU(x)K^{d_{FN}(x)}dx \tag{7.2}$$

where $d_{FN}(x)$ is the distance from the nerve at a given distance along the path ($\overline{d_{FN}}$ is the mean distance for all points considered) and K is the weighting base. In both equations, if the value is higher, more heat will be generated.

Conductivity between Drill Path and Nerve

The second risk metric focuses on the composition of bone between the drill path and the facial nerve. Since the mastoid bone contains irregularly sized and shaped air pockets, the thermal conductance between the drill path and facial nerve varies with bone composition heterogeneity. The conductance is analyzed by considering a simplified case of one-dimensional heat flow from the point at which the drill passes closest to the nerve and the closest point on the nerve. This calculation is performed by considering a series of cylinders extending from the closest points between the drill path and facial nerve (see Figure 7.3). Each cylinder represents a thermal resistance element for one-dimensional conduction between the drill and the nerve. The resistance of each cylindrical element is estimated based on the intensity in the image within that element, which can be correlated with thermal conductivity and resistance. The thermal conductivity of cortical bone and air are 0.55 W/mK [25] and 0.0269 W/mK (at 37°C) [120], respectively. The modified intensity values of cortical bone and air (normalized for CT scanner and shifted such that air has a value of 0 - see Appendix B for more details) are approximately 2500 HU and 0 HU, respectively. Thus, the thermal conductivity of a given voxel or set of voxels in a CT image can be estimated using these values as a reference. Assuming a linear interpolation between the densities of air and bone and their associated thermal conductivities:

$$k_{thermal} = 0.027 + (2.09 \times 10^{-4})h_{image} \tag{7.3}$$

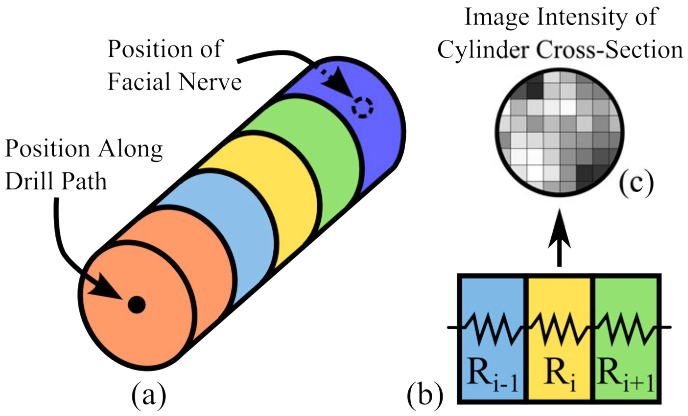

Figure 7.3: Schematic of thermal resistance between closest points along drill path and facial nerve. (a-b) Representation as a stack of cylinders of a given radius between the drill path and the nerve with each cylinder considered as a resistance value in series. (c) The resistance value of each cylinder is determined from the image intensity.

where h_{image} is the image intensity value. The thermal resistance of each cylinder is then computed by:

$$R_{thermal} = \frac{L_{cyl}}{k_{thermal} A_{cyl}} \tag{7.4}$$

where L_{cyl} and A_{cyl} are the cylinder length and area, respectively. The total resistance (R_{total}) between the drill path and facial nerve along the series of cylinders is then given by:

$$R_{total} = R_1 + R_2 + ... + R_N \tag{7.5}$$

where N is the total number of cylinders. The conductance is simply equal to $1/R_{total}$. Several cylinder diameters are considered and compared in this analysis, which helps to account for bone composition in the larger region between the path and the nerve as well as the bone along the shortest path to the nerve.

Using the Two Risk Metrics

After the two thermal metrics are computed for a given patient, the values are compared to the full clinical data set. The values are then ranked and given to the surgeon as a relative ranking (e.g. "This patient ranks in the riskiest 44% for intensity along the drill path and in the riskiest 26% for thermal conductance between the drill path and the nerve"). The surgeon then decides on the appropriate surgical approach for this patient.

7.2.2 Surgical Drilling Protocol for Reduced Heat Generation

The purpose of this section is to analyze the parameters that can easily be controlled and standardized for the manual drilling approach and subsequently propose a drilling strategy to increase the safety and consistency of the procedure. Since the drilling for this surgical approach is performed manually, only a subset of the drilling parameters can be directly controlled. Other parameters, such as feed rate, can be selected in a general sense (e.g. instruct the surgeon to advance the drill at approximately 1 mm/s), but not precisely. Therefore, careful selection of the controllable parameters is critical to minimize the risk of excessive heat generation. This selection is especially important since the feedback felt by the surgeon (force required to advance the drill, stalling of the drill, change in sound, etc.) does not provide enough information to estimate the temperature at the drill tip. As a result, the reduction of heat relies primarily on selection of an appropriate drilling strategy pre-operatively rather than impromptu strategies in the operating room.

The parameters that define the drilling process are as follows: (1) feed rate, a.k.a. linear advancement velocity, (2) spindle speed of the drill, (3) drilling strategy, e.g. continuous drilling versus interval drilling during which individual drilling intervals are followed by a pause for drill retraction and cooling, and (4) irrigation of the bone and drill bit for cooling. These parameters are discussed individually below.

During manual guided drilling, feed rate and axial thrust force are coupled. Surgeons naturally employ a hybrid force-motion control scheme in which they apply a relatively constant force and the feed rate changes as the bone composition changes. In general, higher axial forces and feed rates are recommended for heat reduction [13]. This increases the rate of heat generation but decreases the time of exposure and associated temperature rise. Thus, the surgeon should be instructed to advance the drill quickly but the drilling trajectory must be specified so the total thermal energy generation within a given time period is limited.

The drilling strategy is controlled by employing an interval drilling approach, which is often used in industrial processes for reduced heat and tool wear [6, 63]. In this application, interval drilling is important for limiting the duration of periods during which heat is being generated within the bone and providing time for the bone to cool between these heat generation periods. The interval drilling trajectory is defined by two components: depth of each interval and time between intervals. Along with the feed rate, the depth determines the amount of heat generated during each interval. The work of Feldmann et al. [45] shows that shorter interval length (more intervals) resulted in lower peak temperatures. As such, each drilling interval

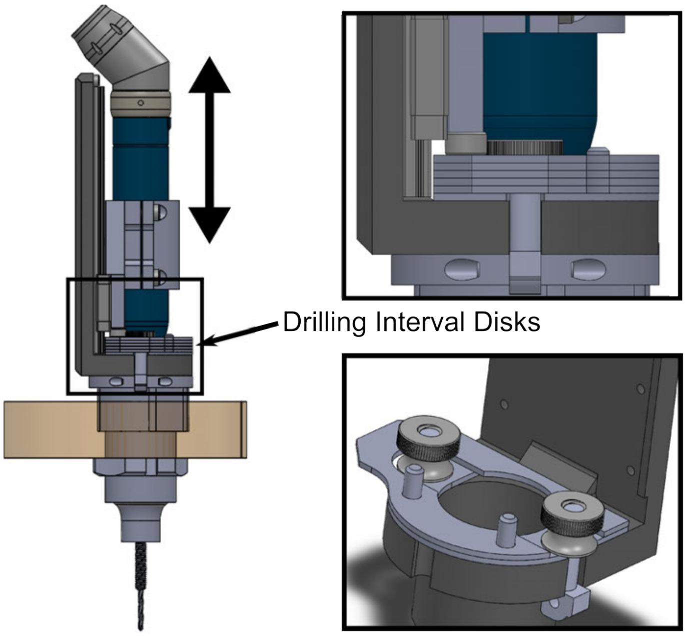

Figure 7.4: Rendering of interval disks for constraining the manually-driven drill press for minimally invasive CI surgery to specified drilling intervals ("pecks").

in the region near the facial nerve is constrained to only advance a depth of 0.75 mm. The depth is restricted by a series of disks that are placed on the base of the drill press (see Figure 7.4). After each interval, the topmost disk is removed, allowing the drill to travel slightly deeper into the temporal bone.

The time between subsequent drilling intervals allows the bone to cool, minimizing the compounding of temperature increases caused by each drilling interval. Longer pauses permit more cooling and enables the bone to return to approximately ambient temperature; however, this benefit must be weighed against extending the duration of the surgical procedure. To determine an appropriate time, which we defined as the minimum time needed for the bone to return to within approximately 3°C of base body temperature, experimental measurements of drilling temporal bones were analyzed. Figure 7.5 shows a schematic of this calculation. Considering a worst-case

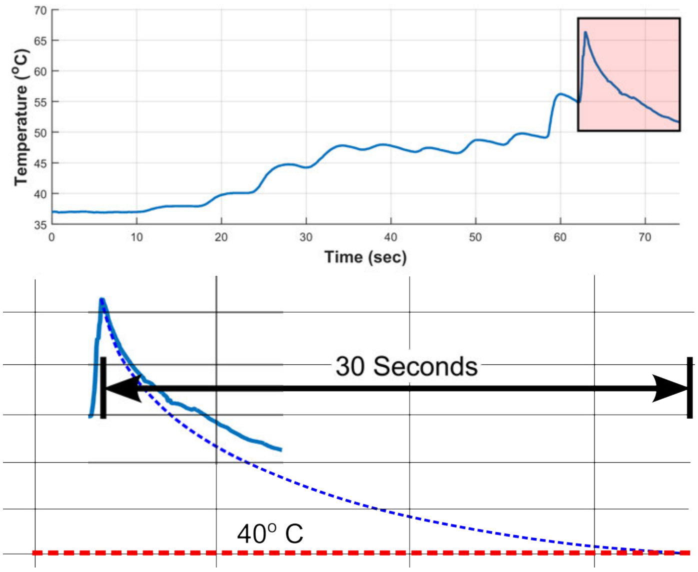

Figure 7.5: Schematic showing estimation of required time between drilling intervals. (Top) Sample data set from [47] showing temperature over time at a distance of 0.5 mm from the facial nerve at the facial recess. (Bottom) The data is cropped around the final drilling interval and overlaid with model data calculated using the model described in [44]. Note that the model decreases faster since the drill was left in the drilled hole after the peak temperature was reached.

scenario, in which temperature rose to over 65°C the cool down phase on the last interval was analyzed. The data was extrapolated using the moving point source thermal model from [44] and setting $\dot{Q}$ equal to zero at the peak temperature time. It was determined that the bone temperature would return to within approximately 3 degrees of body temperature if left to cool for 30 seconds between drilling intervals. In more likely scenarios where the temperature rise is lower, the bone temperature would cool to an even lower temperature.

Recommendations for drill spindle speed vary in the literature; however, it is generally recommended to use lower spindle speeds when possible [13]. Lower spindle speeds help to reduce the amount of friction between the drill bit and the walls of the drilled tunnel and, in turn, the amount of heat generated. Standard otologic drills, however, are designed for high spindle speed, low torque operation. Thus, their performance is limited at lower spindle speeds during which the drill can stall very easily. To balance the performance limitation with the need for lower spindle speeds, the surgeon should use the lowest speed that enables cutting of bone without stalling the drill. In our application, the spindle speed is limited to a maximum of 20,000 rpm (lower values should be used when possible without the drill stalling). As a brief side note, if a higher torque drill was developed and approved for otologic drilling, it could dramatically reduce the heat generated during this procedure since a much lower spindle speed could be used. This would decrease the rubbing of the bit on the sides of the tunnel and lower the risk of sharp temperature increases if the surgeon keeps the bit spinning in the hole for too long.

Finally, the method of irrigation during the drilling process must be considered. Flood irrigation is used while milling a mastoidectomy during traditional CI surgery. In the minimally invasive approach, irrigating the cutting site is more difficult since the drill bit fits snugly within the hole and tends to pump water out of the hole rather than allow it to travel down to the cutting site. Thus, sufficient irrigation must be provided into the drilled hole between drilling intervals while the bit is removed. It is also important to cool the bit directly and remove any material embedded in the flutes with a higher pressure stream. This is accomplished by using a narrow (18 gauge) needle at the end of the irrigation tubing. The surgeon must verify that no material is embedded in the flutes of the drill bit before beginning the next drilling interval.

Table 7.1: Summary of drilling and control mode for manual, guided drilling.

Parameter	**Control Mode**	**Specification**
Feed rate	Manual	Approximately 5 mm/s
Spindle speed	Maximum set; manually controlled	$\leqslant 20,000$ rpm
Drilling intervals	Mechanically constrained	0.75 mm per interval
Interval timing	Fixed (timer used)	$\geqslant 30$ seconds between intervals
Irrigation	Manually administered	Flood hole before/after each interval; cool bit between intervals (18 gauge needle tip)

If material is embedded and cannot be easily removed, the drill bit is exchanged for a new one. A summary of the drilling strategy and associated modes of control is provided in Table 7.1.

7.3 Methods for Evaluation of Temperature Rise Near the Facial Nerve

In this section, an experimental setup to measure temperature rise near the facial nerve on fresh cadaver specimens for validation of the proposed strategy is presented. A key assumption made in the model developed by Feldmann et al. and used to infer the temperature very close to the facial nerve is material homogeneity. The porosity of the mastoid due to various-sized air cells results in a non-homogeneous cumulative material. The varying configuration of air cells may approximate a homogeneous material over a longer distance; however, when measuring the temperature closer to the heat source, small changes in bone porosity can yield large differences in temperature. Thus, it is desired to have a more direct measurement of temperature near the facial nerve during the evaluation of different drilling strategies.

An experimental setup and procedure was developed to evaluate the temperature rise near the facial nerve while drilling through ex vivo temporal bone specimens using Microtable system [75,79]. This was done by cutting the specimens such that the bone near the facial nerve could be viewed with a thermal camera from the medial side. To set up each bone for the experiments, a modified version of the surgical planning protocol was performed as follows. Bone anchors and fiducial markers were fixed to the temporal bones and an image was acquired using a portable CT scanner (xCAT ENT, Xoran Technologies, Ann Arbor, MI, USA). Vital anatomy was automatically segmented [93,95] and the drilling trajectory from the skull surface to the facial recess was planned on the CT scan [94]. Using the location of the fiducial markers and the planned drill path, the Microtable was then designed, manufactured, assembled and mounted to the fiducial markers on the temporal bone.

Then, using the Microtable as guidance, the bone was cut along a plane at the facial recess, perpendicular to the drill path (parallel to Microtable). The facial recess was chosen as the plane at which to measure temperature since the drill path passes close to the facial nerve in this area. Furthermore, since there is an air gap in the facial recess and middle ear, a cut at this location does not affect the boundary conditions of the heat transfer of the bone as much as if the cut was made more laterally. The distance between this cut plane and the Microtable surface was determined in the CT scan (see Figure 7.6).

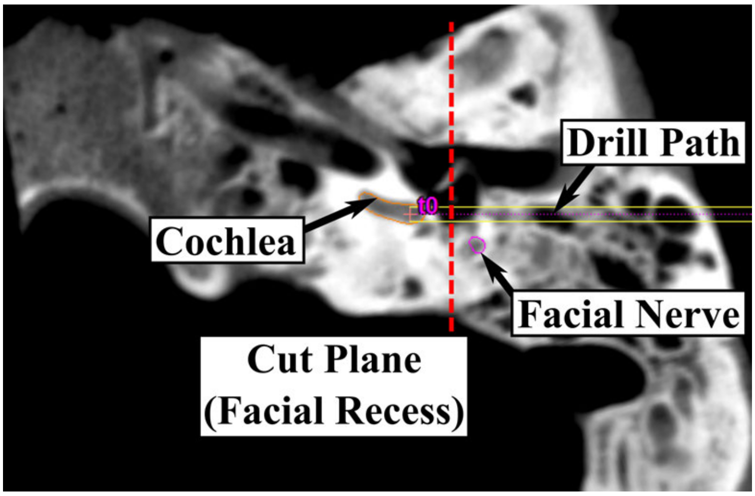

Figure 7.6: CT scan of temporal bone specimen showing planned drill path (yellow), cochlea (purple), and facial recess plane (red) where temperature recordings were made.

The Microtable was then clamped to a lab bench and an infrared thermal camera (Flir A655sc, Flir Systems, Wilsonville, OR, USA) with a 50 μm close-up lens was positioned to record the bone temperature at the cut plane (Figure 7.7) while drilling. A linear transducer was mounted to the manual drill press to measure the position of the drill during the experimental trial. For the first few trials, the temperature was measured during both stages of drilling (lateral and medial); however, there was not a noteworthy temperature rise at the measurement plane while drilling the lateral stage so for the remainder of the experiments, only the medial stage drilling was monitored. The thermal data was exported to MATLAB and the temperature distributions throughout the trajectories were analyzed. Fresh cadaver temporal bones were obtained from Science Care Inc. (Phoenix, AZ, United States) and 3-4 drilling trials per bone were performed. For each bone, the first trial was planned to follow the path that would be used for the surgery (from the skull surface to the cochlea). The subsequent trials were parallel to this first path and offset by several millimeters. All

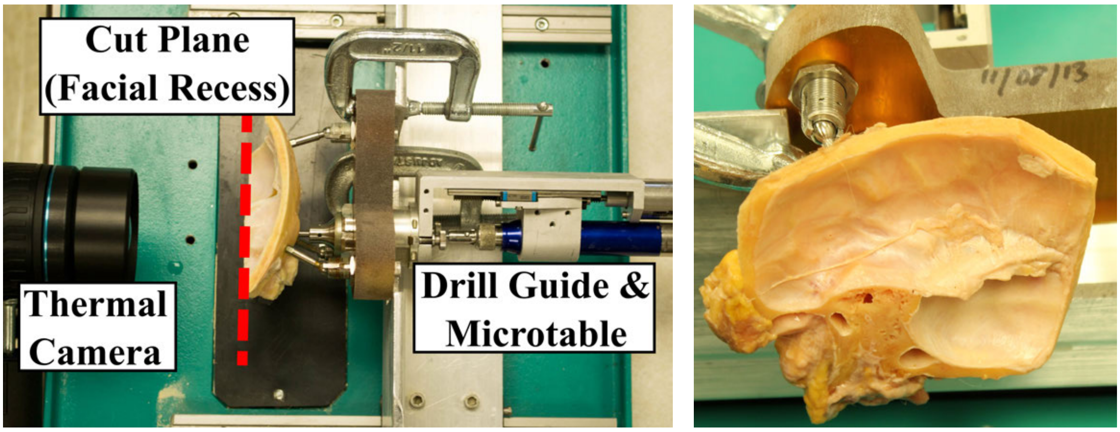

(a) (b)

Figure 7.7: (a) Experimental setup showing device hardware mounted to a temporal bone and thermal camera positioned to record temperature during drilling at a plane located at the facial recess and (b) photograph of medial side of temporal bone specimen at plane of temperature measurement.

trials were performed at room temperature (approximately 20°C) so the temperature data was shifted upwards linearly to account for starting at approximately 37°C in a clinical scenario.

7.4 Ex-Vivo Evaluation of Revised Manual Drilling Strategy

The revised drilling strategy described in Section 7.2 was evaluated using the experimental setup described above. A drill spindle speed of 20,000 rpm was used for all trials. The surgeon was instructed to advance the drill as quickly as he was comfortable with and to start the drill spindle (using a foot peddle) when the drill was approximately 1 cm from the start of the cutting site. An assistant provided the

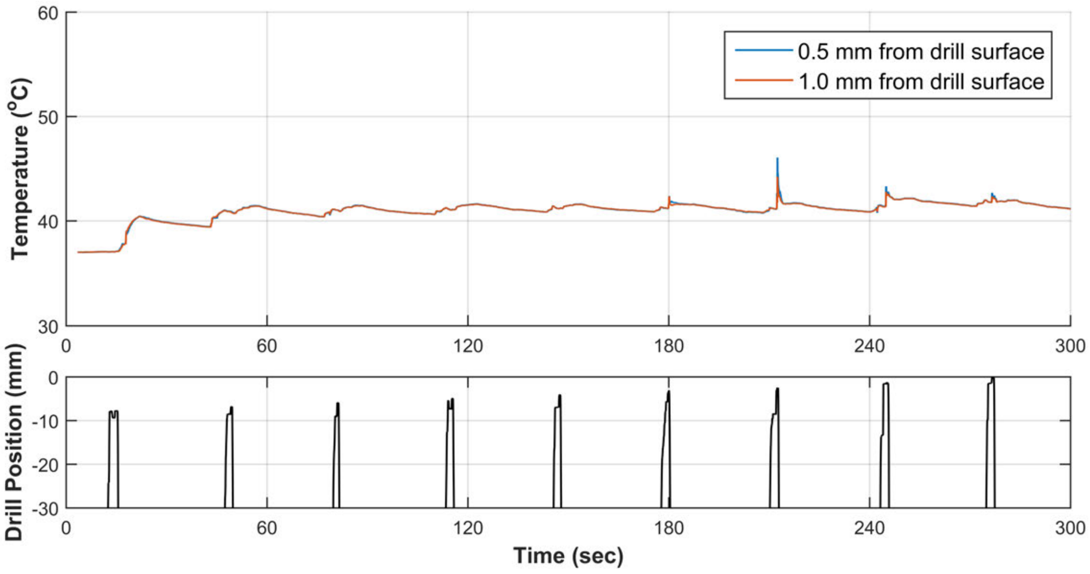

Figure 7.8: Sample data from experimental evaluation showing the temperature over time at 0.5 mm and 1.0 mm from the edge of the drill (top) and drill position over time as controlled by the surgeon (bottom).

irrigation immediately before and after each drilling interval of the medial stage and provided direct irrigation on the drill bit between stages.

Four fresh temporal bones were used and three trials per bone were performed. The thermal camera malfunctioned for one of the trials so only 11 of the 12 trials provided usable data. An example data set showing the temperature versus time and drill position over time is shown in Figure 7.8. Figure 7.9 shows the temperature data over time at the facial recess at distances of 0.5 and 1.0 mm from the edge of the drill for all 11 trials. 0.5 mm represents a worst case scenario for the distance between the drill bit and the facial nerve. This distance is typically between 0.5 and 1.0 mm, depending on patient anatomy.

Of the 11 trials, 9 show temperature profiles that are below 50°C for the entire

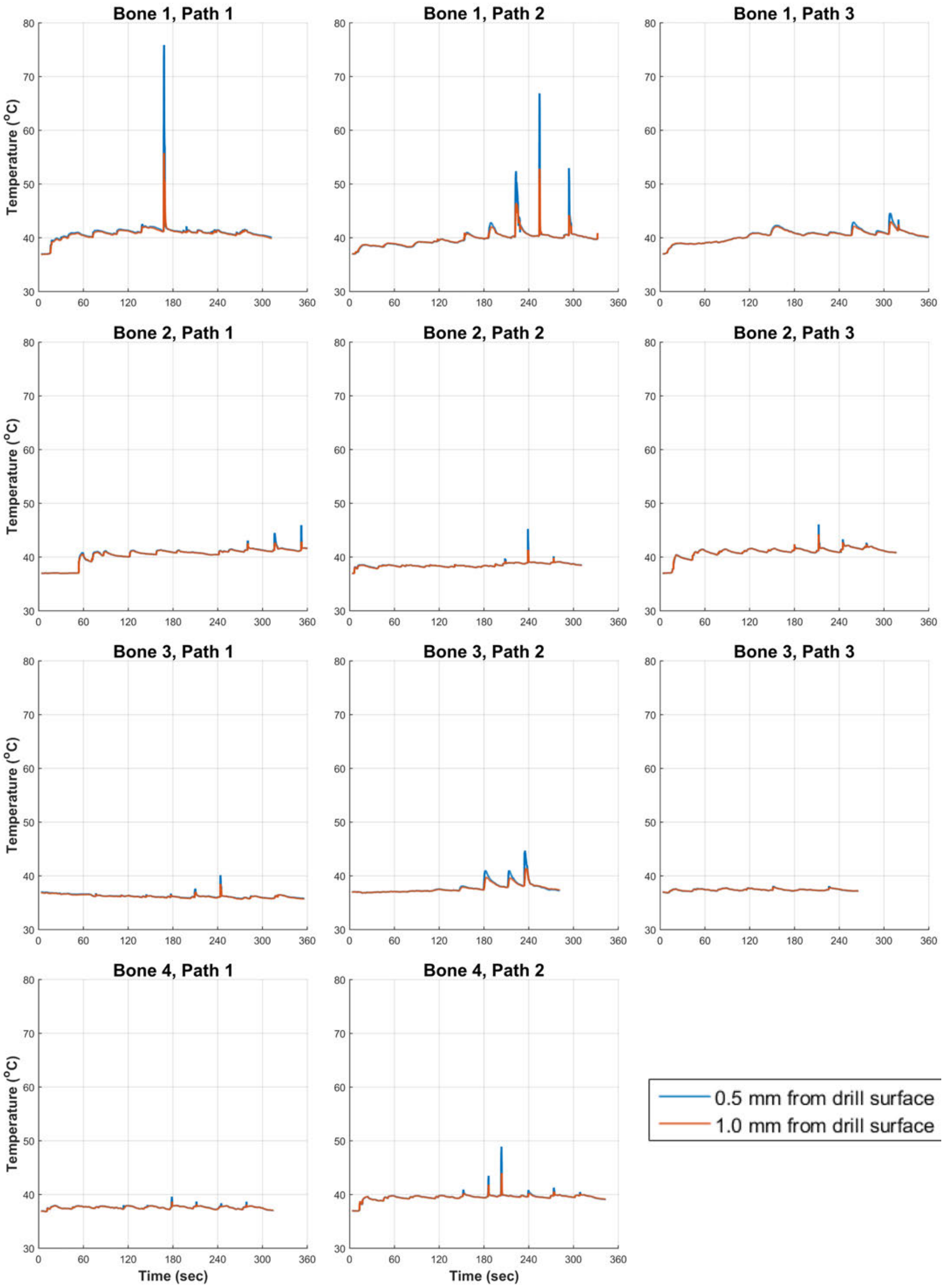

Figure 7.9: Temperature versus time plots for 11 experimental trials using the revised drilling strategy described in Section 7.2. Temperature measurements are at the facial recess, near where the drill passes close to the facial nerve. Note that the thermal camera data acquisition malfunctioned for one trial so only two paths were analyzed for Bone 4.

drilling process at a distance of 0.5 mm from the drill path at the facial recess. Furthermore, the temperature is near 40°C for the majority of the trial durations and the spikes above 45°C are very brief. Two trials (Bone 1, Paths 1 and 2) had spikes in temperature that exceeded 60°C.

The data was also analyzed according to the pre-operative protocol described in Section 7.2.1. The four temporal bone scans were analyzed and compared to each other and the prior clinical data set of nine patients [75] in terms of the two pre-operative risk metrics. The pre-operative scans indicate that Bone 1 was at much higher risk than Bones 3-4 for excessive heat near the facial nerve, which is supported by the experimental results. In fact, when considering the CT images of the 13 specimens/patients in terms of the various patient-specific risk metrics described earlier, Bone 1 stands out as being very high risk. Bone 1 is in the top 11.5% for the integral of the bone intensity along the drilled path in the critical zone passing by the nerve, and the top 11.5% for conductance between the drill path and facial nerve, respectively. For comparison, Bone 2 is in the top 42.3% and 73.1%, Bone 3 is in the top 26.9% and 96.2%, and Bone 4 is in the top 40.4% and 84.6% in those metrics.

7.5 Discussion

To evaluate the results from the various experimental trials and compare the data with estimates of temperature thresholds in the literature, the temperature response must be analyzed in terms of both temperature and exposure time. One common approach for quantifying tissue damage, which was originally used for measuring thermal doses for heat-based cancer therapies, is to calculate the cumulative equivalent minutes at 43°C (CEM43C):

$$\text{CEM43C} = \int_0^{t_{final}} R(T(t))^{43-T(t)} dt \tag{7.6}$$

where $R(T(t)) = 0.5$ if $T(t) > 43$°C and $R(T(t)) = 0.25$ otherwise. The equation is integrated over the time of tissue exposure and provides a metric that enables better comparison between various sets of transient temperature data and evaluation of likely tissue damage. According to this equation, as the temperature is increased by one degree Celsius, the exposure time must be decreased by a factor of two for the same thermal dose.

The temperature thresholds for different tissues vary considerably [130] and the threshold of the facial nerve is unclear. There have been several prior studies evaluating the temperature tolerance neural tissue, which can be used to estimate the tolerance of the facial nerve. Table 7.2 provides a list of some of these studies, along with the model used and their findings. The results vary substantially due to different animal models used (e.g. porcine laryngeal nerve, rat sciatic nerve) and method of applying heat (e.g. heated saline, high-intensity focused ultrasound).

Some studies suggest that nerves can be damaged at fairly low temperatures. For example, the work from De Vrind et al. [26] showed that rat sciatic nerve damage (decrease in function by at least 50%, as measured by electrophysiological examination) occurred in over 50% of the specimens when exposed to temperatures as low as 43°C for 60 to 80 minutes. This temperature threshold is further supported by Haveman et al. [53], who concluded that peripheral nerve temperature should not exceed 44°C

Table 7.2: Prior research investigating temperature thresholds for neural injury.

Paper	**Model / Heating Method**	**Findings**
Lin et al., 2015 [84]	Porcine recurrent laryngeal nerve; Heated saline irrigation	EMG changes after 3 sec exposure at 60°C, partially recoverable after 20 sec, irrecoverable after 60 seconds (no EMG changes after 60 sec at 55°C)
Harnof et al., 2013 [51]	Porcine optic nerve; High-intensity focused ultrasound (HIFU)	Histologic evidence of thermal injury when exposed to 50-60°C for 6-10 sec
Bunch et al., 2005 [15]	Canine phrenic nerve; Radioablation catheter	Diaphragm motion impaired at 47 ± 3°C with first onset at 20 sec
De Vrind et al., 1992 [26]	Rat sciatic nerve; 5 mm segment of nerve heated with thermode	Temporary nerve damage at different exposure times at 43-45°C; motor function recovered after 20 days
James et al., 1964 [59]	Temperature measured in at facial nerve in cadaver temporal bone with HIFU power levels that caused facial nerve paralysis in patients; HIFU for destruction of vestibular organs	46°C determined to be temperature associated with ultrasound intensity of 22 W/cm^2, which caused facial paralysis in 2 out of 40 patients when used clinically (no surgical exposure time given)

for more than 30 minutes (CEM43C = 60 min).

Other studies present higher temperature thresholds for nerves. Lin et al. studied the electromyographic (EMG) response of porcine recurrent laryngeal nerves after exposure to saline solutions at different temperatures/durations. They concluded that 60°C is a critical temperature for recurrent laryngeal nerve thermal injury. In their experiments, no EMG change was measured at 55°C after 60 seconds; however, damage occurred at 60°C. Nerve function was partially recoverable after 20 seconds (CEM43C = 4.37×10^4 min) and irrecoverable after 60 seconds (CEM43C = 1.31×10^5 min).

Perhaps the most relevant report related to estimating the threshold for facial nerve damage was completed by James et al. [59]. While using their high-intensity focused ultrasound (HIFU) in the 1960s for destruction of vestibular organs in patients with Meniere's disease, they reported 2 out of 40 patients had experienced facial nerve paralysis. They then measured the temperature at the facial nerve in cadaver temporal bones while using the HIFU at various power settings. At the power setting that was used in the previous 40 clinical cases (25 W/cm^2), the temperature was approximately 48°C after a brief warm up period. They then lowered the power to 22 W/cm^2 for clinical practice and no subsequent patients experienced facial paralysis (75 cases at the time of publication). This lower power corresponded to a temperature of 46°C in the cadaver trials, which they concluded is the upper bound of facial nerve temperature tolerance. Of course, this conclusion does not incorporate the exposure duration. From their description of the ultrasound approach, it appears that the patient was be exposed to the maximum power HIFU for approximately 10-20 minutes

(CEM43C = 80-160 min).

The experimental results can now be considered in the context of the criteria proposed in the literature discussed above. All trials except for Paths 1 and 2 for Bone 1 have CEM43C values below 1 minute and are considered to be safe according to even the most conservative criteria (e.g. [53]) at distances of 0.5 mm (and greater) from the drill surface. The two trials with higher peak temperatures are considered unsafe by all criteria discussed above if the nerve was 0.5 mm from the drill surface. If the nerve was 0.75 mm from the drill surface, these trials are considered safe by some criteria and unsafe by others; and at a distance of 1.0 mm from the drill surface, these trials are considered safe by all criteria. Table 7.3 summarizes this data and the pre-operative risk assessment for each specimen.

However, it is important to note that the two cases in which temperature rose to potentially unsafe levels would have been excluded using the pre-operative screening protocol described in Section 7.2.1. Thus, for all cases in which the minimally invasive approach would have been performed, the thermal dose was at a safe level. We feel that this represents an important advancement over the prior clinical implementation. Previously, the pre-operative risk to thermal nerve injury did not appear to be related to the patient-specific risk due to inconsistencies with the surgical approach. In fact, when we analyzed the CT scans of the patients that participated in the initial clinical implementation of image-guided, minimally invasive CI surgery (see Appendix B) we found that the patient who experienced facial nerve injury did not rank particularly high in the pre-operative risk metrics (6th and 7th out of 9 patients for the bone density integral and conductivity metrics, respectively). This patient would therefore

Table 7.3: Pre-operative risk metric values/ranks and CEM43 for all trials.

		Pre-Op Risk Metrics (Pct. Rank)[a]		**CEM43 at Dist. from Drill**[b]		
Bone	**Path**	**Path Intensity Integral**	**Thermal Conductance**	**0.5 mm**	**0.75 mm**	**1.0 mm**
1	1	11.5%	11.5%	2.10×10^7	1.12×10^4	34.8
	2			3.91×10^4	256.9	7.37
	3			0.57	0.44	0.35
2	1	42.3%	73.1%	0.52	0.43	0.40
	2			0.02	0.01	0.01
	3			0.50	0.49	0.48
3	1	26.9%	96.2%	< 0.01	< 0.01	< 0.01
	2			0.10	0.03	0.01
	3			< 0.01	< 0.01	< 0.01
4	1	40.4%	84.6%	< 0.01	< 0.01	< 0.01
	2[c]			-	-	-
	3			0.34	0.10	0.06

[a] See Section 7.2.1 for a description of each metric. Risk percentiles based on the scans of the four bones included in this study and the nine patients scans from [75] (lower percentile indicates higher risk).

[b] Value calculated at various distances from the drill surface; mean temperature at each time step at a given distance used in calculation.

[c] No thermal data for this trial due to a malfunction in the thermal camera recording software.

not have been excluded from the approach. The reason for thermal injury is more likely related to how the drilling was carried out for that particular case since it was not standardized across patients. Now, with a standardized drilling strategy, the higher risk patients per the pre-operative evaluation appear to be associated with higher temperatures at the facial recess, enabling an effective criteria for exclusion.

In conclusion, the revised surgical protocol for minimally invasive CI, including the pre-operative scanning step and the improved drilling strategy enables safe implementation of this surgery in cases in which the patient is not pre-disposed to high risk of thermal injury. More testing is necessary to validate these results prior to performing the surgery again clinically; however, the initial results are promising and provide an important advancement towards clinical translation. The exclusion criteria appears to be effective, especially if used conservatively; however, more patient data needs to be considered to provide better estimates of patient risk and subsequently determine the appropriate risk level for exclusion.

Chapter 8

Future Work & Conclusions

This dissertation presents the development and testing of image-guided and robotic systems for otologic and neurotologic surgery. Several analyses are performed and models are developed to inform the design, workflow, and trajectory planning of a compact bone-attached robot for mastoidectomy. Two robot prototypes are developed and tested in phantom material, cadaver temporal bones, and fresh human cadaver heads. Additionally, potential safety issues with the minimally invasive approach to cochlear implantation (CI) surgery - excessive heat generation and drilling accuracy near vital anatomy - are analyzed and experimentally evaluated. The results are used to improve the planning and drilling processes and facilitate safe clinical translation of the surgical approach.

Chapters 2-5 focus on the development of a bone-attached robot for mastoidectomy and associated planning and trajectory generation algorithms, with a particular emphasis on the translabyrinthine approach to vestibular schwannoma. Chapter 2 provides an investigation into some of the technical requirements for robotic mastoidectomy [31, 35]. Experiments were performed to measure the forces required by a robot while milling temporal bone and the workspace requirements for mastoidectomy and translabyrinthine bone milling were evaluated. The data in this chapter can be used as design inputs for any robotic mastoidectomy system. Chapter 3 describes the proposed surgical workflow of such a bone-attached robot and presents two prototypes [31, 33]. Experiments in cadaver temporal bones were first performed to validate the approach, followed by more clinically-relevant experiments in fresh cadaver heads targeting deeper cavities for the translabyrinthine approach to vestibular schwannoma. In all experiments, which represent the first use of a bone-attached robot for temporal bone milling, vital nerves were preserved and the robot achieved sub-millimetric accuracy in terms of planned versus actual resection volumes.

Next, a method for generating patient-specific safety margins around vital anatomic structures using stochastic error modeling is presented in Chapter 4 [38]. Instead of using an arbitrary thickness value, a desired preservation probability specified by the surgeon for a particular structure is used as an input to the algorithm. The margin is then iteratively grown as the surgery is simulated until it is large enough to match the surgeon's desired preservation probability. The algorithm was tested for planning of robotic mastoidectomy but the framework can be applied to other procedures in which a robot is moving in close proximity to vital anatomy. In Chapter 5, an algorithm is presented to improve the safety and efficiency of the robotic bone milling trajectory by incorporating patient-specific bone density data and segmentations of vital anatomy from the pre-operative image [34]. Tool orientation and velocity are selected according to optimization functions that use force modeling and data from prior experiments related to cutting efficiency. This approach, which was evaluated against constant orientation and velocity paths, enables decreased forces near vital anatomy and more aggressive, faster cutting in non-critical regions.

Chapters 6 and 7 describe analyses and experimentation for improving the minimally invasive approach to CI surgery. The system previously developed and tested clinically at Vanderbilt is used in the work and two key safety issues are investigated for the purpose of enabling safe clinical translation: drilling accuracy and heat rise near the facial nerve. Chapter 6 presents a set of drilling accuracy experiments that examine the effect of various anatomic features (e.g. angle of the skull surface at the entry point and bone composition along the drill path) on the deviation of the drill [32]. The data can be used to help plan safer drill paths by minimizing deflections that could cause the drill to deviate away from the target point in the scala tympani or towards the facial nerve. Finally, Chapter 7 presents an experimental evaluation of the heat rise in the bone near the facial nerve while drilling the minimally invasive tunnel for CI electrode insertion [36]. An improved surgical protocol, including a pre-operative risk assessment and revised drilling strategies, is proposed and tested using a novel experimental setup that enables temperature measurement near the facial nerve of fresh cadaver temporal bones. The results show that the revised drilling strategy enables safe and consistent execution of the drilling component of the procedure on patients that are not pre-disposed to high risk of excessive heat near the facial nerve. Patients that are high risk are effectively screened and excluded using the proposed pre-operative screening process that consists of CT image-based thermal modeling and estimates of thermal conductivity between the drill path and the facial nerve.

8.1 Future Work in Robotic Mastoidectomy

Future work in robotic mastoidectomy should focus on further testing of the approach, with an emphasis on improving the integration of the system with the existing clinical workflow. For such a system to be clinically viable, particularly for translabyrinthine vestibular schwannoma surgery, it must save time in the operating room. The experimental trials in full cadaver heads presented in this dissertation are a good start but additional evaluation is needed. A next step, for which we have received institutional review board approval, is to test all steps of the system except for the milling on patients. This will provide valuable insight into the time required for the system setup, robot attachment, intra-operative CT scanning and planning, etc. as well as any practical challenges with these steps.

One of the major barriers for any new device is acceptance by the medical professionals who will be using and interacting with it. A potential issue with clinical acceptance of an autonomous robot for mastoidectomy is that it eliminates much of the feedback the surgeon receives while manually milling bone and makes the surgeon feel that they are not an active participant in this portion of the surgery. This issue also played an important role in robotic bone milling for orthopedic surgery. Initially, a fully autonomous system was developed (ROBODOC Surgical System, Curexo Technology Corp., Fremont, CA, USA, formerly Integrated Surgical Systems, Inc.). Later, a system in which the surgeon cooperatively controls the drill with the robot was developed and has become the leader in robotic bone milling (RIO System by MAKO Surgical Corp., Ft. Lauderdale, FL, USA, subsequently acquired by Stryker Corp.) . A cooperatively-controlled device may also be a more viable option for otologic bone milling; however, given the high accuracy requirements and small surgical workspace, there are additional challenges compared to orthopedic surgery. Instead, an automated system could be made more clinically viable by increasing the intelligent interaction between the surgeon and the robot, which would keep the surgeon “in the loop” and provide additional useful information such as where the drill tip is relative to critical anatomy.

As the robotic system moves closer to clinical translation, an operating room ready version will need to be developed. The major design changes, compared to the second prototype described in this dissertation, should focus on sterilizability. Ideally, the entire robot would be sterilizable, which is not currently the case. To do this, the current motors and sensors must be substituted with sterilizable versions. If this is not possible, or presents additional challenges that outweigh the benefits (e.g. size of available sterilizable actuators, controllability with limited sensing, etc.), alternative means of separating the robot from the patient could be used. For example, the structure of the robot could be bagged with the drill mounted through the bag in the operating room after it is sterilized.

Finally, and most importantly, all future work on this project should emphasize the benefits to the patient. Currently, we have a well-developed robotic system; however, its real clinical benefit is unknown. The approach has the *potential* to improve some aspects of otologic surgery, such as a decrease in procedure time, removal of less bone, and a reduction in complication rates (e.g. reduction in instances of facial nerve damage). These potential benefits need to be better quantified through additional experimental evaluation and comparison with clinical data to determine if translation of this approach would ultimately lead to better clinical outcomes.

8.2 Future Work in Patient-Specific Planning for Robotic Surgery

Future work related to the algorithm for generating patient-specific safety margins using error models of the image-guided system should focus on generalizing and extending the methods to other types of surgeries. The framework in this dissertation is described in a general sense but it has not yet been applied to procedures other than robotic mastoidectomy. Such an extension would show the general applicability of the approach and make it even easier for others to apply it to their own specific work. One type of intervention that could benefit from this algorithm is heat-based procedures (e.g. thermal ablation of cancerous tissue). If the heat spread and the placement position of the tool can be modeled statistically, the power and time can be adjusted by simulating the surgery until the entire target region reaches a high enough probability of receiving the required thermal dose. Additionally, the margins of the desired ablation region could be modeled probabilistically as well and included in the algorithm. Other procedures that could also benefit from this algorithm include the placement of deep brain stimulation electrodes and needle biopsies.

8.3 Future Work in Minimally Invasive Cochlear Implantation Surgery

The next major step in minimally invasive CI surgery is further clinical translation with the improvements made since the first implementation. The Microtable system as well as the associated planning and execution methods are at a mature state and need to be evaluated more thoroughly in patients. The last minor step prior to a clinical study is to complete more thermal monitoring experiments for further validation of the approach presented in this dissertation and determine a better risk threshold for patient exclusion from the minimally invasive approach. The latter also requires more patient data to be incorporated so that a better approximation of patient risk relative to the general population can be made. Then, along with the additional experimental data, a more informed cut-off criteria can be determined.

An Investigational Device Exemption (IDE) has been granted for the Microtable system for a feasibility study of 12 patients (IDE granted on 10/13/2016 to Robert F. Labadie at Vanderbilt University Medical Center). Furthermore, a clinical trial with the robotic system for minimally invasive CI surgery developed at the University of Bern is currently ongoing and a commercial system is being developed as part of a collaboration between MED-EL GmbH (Innsbruck, Austria) and CAScination AG (Bern, Switzerland) [18]. The fact that two research groups are progressing quickly towards clinical translation suggests that minimally invasive CI is going to be an alternative to traditional CI surgery in the near future. This will enable standardization of the surgery and will hopefully bridge the large gap between patients who could benefit from an implant and those that actually receive one. The incorporation of image-guidance and robotics into CI surgery will also facilitate translation of other beneficial techniques, such as automated electrode insertion (e.g. [100–102] and [88, 107, 108]), which could improve patient outcomes through less traumatic insertions.

8.4 Conclusions

In conclusion, the main objective of the work presented in this dissertation is the advancement of otologic and neurotologic surgery by utilizing the benefits of image-guidance and robotic technology. The systems designed and tested in this work are still primarily in the laboratory but are moving closer to clinical translation with the help of the contributions made in this dissertation. The goal of all medical technology research should be improved clinical outcomes and the systems developed and advanced through this work have the potential to further this goal by providing patients with less invasive surgical options, more consistent results, and decreased risk of complications.

Bibliography

[1] Gregory M Abbas and Raleigh O Jones. Measurements of drill-induced temperature change in the facial nerve during mastoid surgery: a cadaveric model using diamond burs. *Annals of Otology, Rhinology & Laryngology*, 110(9):867–870, 2001.

[2] Eberhard Abele, Stefan Rothenbücher, and Matthias Weigold. Cartesian compliance model for industrial robots using virtual joints. *Production Engineering*, 2(3):339–343, 2008.

[3] Juan Ansó, Cilgia Dür, Kate Gavaghan, Helene Rohrbach, Nicolas Gerber, Tom Williamson, Enric M Calvo, Thomas Wyss Balmer, Christina Precht, Damien Ferrario, et al. A neuromonitoring approach to facial nerve preservation during image-guided robotic cochlear implantation. *Otology & Neurotology*, 37(1):89–98, 2016.

[4] Mohammadreza Arbabtafti, Majid Moghaddam, Ali Nahvi, Mohammad Mahvash, Barry Richardson, and Bijan Shirinzadeh. Physics-based haptic simulation of bone machining. *Haptics, IEEE Transactions on*, 4(1):39–50, 2011.

[5] Antje Aschendorff, Jan Kromeier, Thomas Klenzner, and Roland Laszig. Quality control after insertion of the nucleus contour and contour advance electrode in adults. *Ear and hearing*, 28(2):75S–79S, 2007.

[6] Eyup Bağci and Babur Ozcelik. Investigation of the effect of drilling conditions

on the twist drill temperature during step-by-step and continuous dry drilling. *Materials & design*, 27(6):446–454, 2006.

[7] Ramya Balachandran, Jason E Mitchell, Grégoire Blachon, Jack H Noble, Benoit M Dawant, J Michael Fitzpatrick, and Robert F Labadie. Percutaneous cochlear implant drilling via customized frames: an in vitro study. *Otolaryngology–Head and Neck Surgery*, 142(3):421–426, 2010.

[8] Ramya Balachandran, Jason E Mitchell, Benoit M Dawant, and J Michael Fitzpatrick. Accuracy evaluation of microtargeting platforms for deep-brain stimulation using virtual targets. *Biomedical Engineering, IEEE Transactions on*, 56(1):37–44, 2009.

[9] S Baron, H Eilers, B Munske, JL Toennies, R Balachandran, RF Labadie, T Ortmaier, and RJ Webster III. Percutaneous inner-ear access via an image-guided industrial robot system. *Proceedings of the Institution of Mechanical Engineers, Part H: Journal of Engineering in Medicine*, 224(5):633–649, 2010.

[10] Pierre Bast, M Engelhardt, W Lauer, K Schmieder, V Rohde, and K Radermacher. Identification of milling parameters for manual cutting of bicortical bone structures. *Computer Aided Surgery*, 8(5):257–263, 2003.

[11] Brett Bell, Nicolas Gerber, Tom Williamson, Kate Gavaghan, Wilhelm Wimmer, Marco Caversaccio, and Stefan Weber. In vitro accuracy evaluation of image-guided robot system for direct cochlear access. *Otology & Neurotology*, 34(7):1284–1290, 2013.

[12] Brett Bell, Christof Stieger, Nicolas Gerber, Andreas Arnold, Claude Nauer, Volkmar Hamacher, Martin Kompis, Lutz Nolte, Marco Caversaccio, and Stefan Weber. A self-developed and constructed robot for minimally invasive cochlear implantation. *Acta oto-laryngologica*, 132(4):355–360, 2012.

[13] Nicky Bertollo and William Robert Walsh. *Drilling of bone: practicality, limitations and complications associated with surgical drill-bits.* INTECH Open Access Publisher, 2011.

[14] Derald Brackmann, Clough Shelton, and Moses A Arriaga. *Otologic surgery.* Elsevier Health Sciences, 2010.

[15] T Jared Bunch, G Keith Bruce, Srijoy Mahapatra, Susan B Johnson, Dylan V Miller, Alvaro V Sarabanda, Mark A Milton, and Douglas L Packer. Mechanisms of phrenic nerve injury during radiofrequency ablation at the pulmonary vein orifice. *Journal of cardiovascular electrophysiology*, 16(12):1318–1325, 2005.

[16] William H Call. Thermal injury from mastoid bone burrs. *Annals of Otology, Rhinology & Laryngology*, 87(1):43–49, 1978.

[17] Matthew L Carlson, Michael J Link, George B Wanna, and Colin LW Driscoll. Management of sporadic vestibular schwannoma. *Otolaryngologic Clinics of North America*, 48(3):407–422, 2015.

[18] CAScination. Robotic cochlear implantation by med-el and cascination. `http://www.cascination.com/`

`robotic-cochlear-implantation-by-med-el-and-cascination/`, June 2015 (Accessed: 20 November 2016). 15

[19] Jong-Ha Chung, Seong-Young Ko, Dong-Soo Kwon, Jung-Ju Lee, Yong-San Yoon, and Choong-Hee Won. Robot-assisted femoral stem implantation using an intramedulla gauge. *Robotics and Automation, IEEE Transactions on*, 19(5):885–892, 2003.

[20] J Cobb, J Henckel, P Gomes, S Harris, M Jakopec, F Rodriguez, A Barrett, and B Davies. Hands-on robotic unicompartmental knee replacement a prospective, randomised controlled study of the acrobot system. *Journal of Bone & Joint Surgery, British Volume*, 88(2):188–197, 2006.

[21] John D Currey, Kevin Brear, Peter Zioupos, and Gwendolen C Reilly. Effect of formaldehyde fixation on some mechanical properties of bovine bone. *Biomaterials*, 16(16):1267–1271, 1995.

[22] Andrei Danilchenko. *Fiducial-based registration with anisotropic localization error.* PhD thesis, Vanderbilt University, 2011.

[23] Andrei Danilchenko, Ramya Balachandran, Jenna L Toennies, Stephan Baron, Benjamin Munske, J Michael Fitzpatrick, Thomas J Withrow, Robert J Webster III, and Robert F Labadie. Robotic mastoidectomy. *Otology & Neurotology*, 32(1):11, 2011.

[24] Andrei Danilchenko and J Michael Fitzpatrick. General approach to first-order

error prediction in rigid point registration. *Medical Imaging, IEEE Transactions on*, 30(3):679–693, 2011.

[25] Sean RH Davidson and David F James. Measurement of thermal conductivity of bovine cortical bone. *Medical engineering & physics*, 22(10):741–747, 2000.

[26] HH De Vrind, J Wondergem, and J Haveman. Hyperthermia-induced damage to rat sciatic nerve assessed in vivo with functional methods and with electrophysiology. *Journal of neuroscience methods*, 45(3):165–174, 1992.

[27] Kathleen Denis, Geert Van Ham, Jos Vander Sloten, Remi Van Audekercke, Georges Van der Perre, Joris De Schutter, J-P Kruth, Johan Bellemans, and Guy Fabry. Influence of bone milling parameters on the temperature rise, milling forces and surface flatness in view of robot-assisted total knee arthroplasty. In *International congress series*, volume 1230, pages 300–306. Elsevier, 2001.

[28] Dennis P Devito, Leon Kaplan, Rupert Dietl, Michael Pfeiffer, Dale Horne, Boris Silberstein, Mitchell Hardenbrook, George Kiriyanthan, Yair Barzilay, Alexander Bruskin, et al. Clinical acceptance and accuracy assessment of spinal implants guided with spineassist surgical robot: retrospective study. *Spine*, 35(24):2109–2115, 2010.

[29] Sandeep Dhanik and Paul Xirouchakis. Contour parallel milling tool path generation for arbitrary pocket shape using a fast marching method. *The International Journal of Advanced Manufacturing Technology*, 50(9-12):1101–1111, 2010.

[30] Neal P Dillon, Ramya Balachandran, Antoine Motte dit Falisse, George B Wanna, Robert F Labadie, Thomas J Withrow, J Michael Fitzpatrick, and Robert J Webster. Preliminary testing of a compact bone-attached robot for otologic surgery. In *SPIE Medical Imaging*, pages 903614–903614. International Society for Optics and Photonics, 2014.

[31] Neal P Dillon, Ramya Balachandran, J Michael Fitzpatrick, Michael A Siebold, Robert F Labadie, George B Wanna, Thomas J Withrow, and Robert J Webster. A compact, bone-attached robot for mastoidectomy. *Journal of Medical Devices*, 9(3):031003–1–7, 2015.

[32] Neal P Dillon, Ramya Balachandran, and Robert F Labadie. Accuracy of linear drilling in temporal bone using drill press system for minimally invasive cochlear implantation. *International journal of computer assisted radiology and surgery*, 11(3):483–493, 2015.

[33] Neal P Dillon, Ramya Balachandran, Michael A Siebold, Robert J Webster, George B Wanna, and Robert F Labadie. Cadaveric testing of robot-assisted access to the internal auditory canal for vestibular schwannoma removal. *Otology & Neurotology*, In Press.

[34] Neal P Dillon, Loris Fichera, Patrick S Wellborn, Robert F Labadie, and Robert J Webster. Making robots mill bone more like human surgeons: Using bone density and anatomic information to mill safely and efficiently. In *Intelli-*

gent Robots and Systems, 2016 IEEE/RSJ International Conference on. IEEE, 2016.

[35] Neal P Dillon, Louis B Kratchman, Mary S Dietrich, Robert F Labadie, Robert J Webster III, and Thomas J Withrow. An experimental evaluation of the force requirements for robotic mastoidectomy. *Otology & Neurotology*, 34(7):e93, 2013.

[36] Neal P Dillon, Fichera Loris, Kyle Kesler, M Geraldine Zuniga, Jason E Mitchell, and Robert F Labadie. A protocol for reduced heat generation during guided manual drilling for minimally invasive cochlear implantation surgery. In Review.

[37] Neal P Dillon, Jason E Mitchell, M Geraldine Zuniga, Robert J Webster, and Robert F Labadie. Design and thermal testing of an automatic drill guide for less invasive cochlear implantation. *Journal of Medical Devices*, 10(2):020923, 2016.

[38] Neal P Dillon, Michael A Siebold, Jason E Mitchell, Greg S Blachon, Ramya Balchandran, J Michael Fitzpatrick, and Robert J Webster. Increasing safety of a robotic system for inner ear surgery using probabilistic error modeling near vital anatomy. In *SPIE Medical Imaging*, pages 97861G–97861G. International Society for Optics and Photonics, 2016.

[39] Martin Engelhardt, P Bast, Wolfgang Lauer, V Rohde, Kirsten Schmieder, and Klaus Radermacher. Manual vs. robotic milling parameters for development

of a new robotic system in cranial surgery. In *International Congress Series*, volume 1268, pages 533–538. Elsevier, 2004.

[40] D Gareth R Evans, Anthony Moran, Andrew King, S Saeed, Nihal Gurusinghe, and Richard Ramsden. Incidence of vestibular schwannoma and neurofibromatosis 2 in the north west of england over a 10-year period: higher incidence than previously thought. *Otology & Neurotology*, 26(1):93–97, 2005.

[41] Philipp A Federspil, Urban W Geisthoff, Dominik Henrich, and Peter K Plinkert. Development of the first force-controlled robot for otoneurosurgery. *The Laryngoscope*, 113(3):465–471, 2003.

[42] Philipp A Federspil, Beate Plinkert, and Peter K Plinkert. Experimental robotic milling in skull-base surgery. *Computer Aided Surgery*, 8(1):42–48, 2003.

[43] Philipp A Federspil and Peter K Plinkert. Robotic surgery in otorhinolaryngology. *Otolaryngologia polska. The Polish otolaryngology*, 58(1):237–242, 2003.

[44] Arne Feldmann, Juan Anso, Brett Bell, Tom Williamson, Kate Gavaghan, Nicolas Gerber, Helene Rohrbach, Stefan Weber, and Philippe Zysset. Temperature prediction model for bone drilling based on density distribution and in vivo experiments for minimally invasive robotic cochlear implantation. *Annals of Biomedical Engineering*, 44(5):1576–1586, 2016.

[45] Arne Feldmann, Jasmin Wandel, and Philippe Zysset. Reducing temperature elevation of robotic bone drilling. *Medical engineering & physics*, 38(12):1495–1504, 2016.

[46] António JM Ferreira. *MATLAB codes for finite element analysis: solids and structures*, volume 157. Springer Science & Business Media, 2008.

[47] Loris Fichera, Neal P Dillon, Kyle Kesler, M Geraldine Zuniga, Jason E Mitchell, and Robert F Labadie. Thermal monitoring of the facial recess during drilling for minimally invasive cochlear implantation. In *Computer Assisted Radiology and Surgery, 30th International Congress and Exhibition.* CARS, 2016.

[48] Charles C Finley and Margaret W Skinner. Role of electrode placement as a contributor to variability in cochlear implant outcomes. *Otology & Neurotology*, 29(7):920, 2008.

[49] Lesley C French, Mary S Dietrich, and Robert F Labadie. An estimate of the number of mastoidectomy procedures performed annually in the united states. *Ear, Nose & Throat Journal*, 87(5):267, 2008.

[50] Tamás Haidegger, Sándor Győri, Balázs Benyó, and Zoltán Benyó. Stochastic approach to error estimation for image-guided robotic systems. In *Engineering in Medicine and Biology Society (EMBC), 2010 Annual International Conference of the IEEE*, pages 984–987. IEEE, 2010.

[51] Sagi Harnof, Zion Zibly, Zvi Cohen, Andrew Shaw, Cody Schlaff, and Neal F Kassel. Cranial nerve threshold for thermal injury induced by mri-guided high-intensity focused ultrasound (mrghifu): preliminary results on an optic nerve model. *IEEE transactions on ultrasonics, ferroelectrics, and frequency control*, 60(4):702–705, 2013.

[52] R Häusler. Cochlear implantation without mastoidectomy: the pericanal electrode insertion technique. *Acta oto-laryngologica*, 122(7):715–719, 2002.

[53] J Haveman, Jill Van Der Zee, J Wondergem, JF Hoogeveen, and MCCM Hulshof. Effects of hyperthermia on the peripheral nervous system: a review. *International journal of hyperthermia*, 20(4):371–391, 2004.

[54] SC Ho, RD Hibberd, and BL Davies. Robot assisted knee surgery. *Engineering in Medicine and Biology Magazine, IEEE*, 14(3):292–300, 1995.

[55] Ingeborg Hochmair. Cochlear implant facts. `http://www.medel.com/cochlear-implants-facts`, September 2013 (Accessed: 8 August 2016).

[56] Howard P House and William F House. Historical review and problem of acoustic neuroma. *Archives of Otolaryngology*, 80(6):601–604, 1964.

[57] John W House and Derald E Brackmann. Facial nerve grading system. *Otolaryngology–head and neck surgery: official journal of American Academy of Otolaryngology-Head and Neck Surgery*, 93(2):146, 1985.

[58] M Jakopec, SJ Harris, F Rodriguez y Baena, P Gomes, J Cobb, and BL Davies. The first clinical application of a hands-on robotic knee surgery system. *Computer Aided Surgery*, 6(6):329–339, 2001.

[59] J Angell James, GA Dalton, HF Freundlich, MA Bullen, PNT Wells, DA Hughes, and J Chow. Histological, thermal and biochemical effects of ultrasound on the labyrinth and temporal bone. *Acta oto-laryngologica*, 57(3-6):306–312, 1964.

[60] Peter Kazanzides, Brent D Mittelstadt, Bela L Musits, William L Bargar, Joel F Zuhars, Bill Williamson, Phillip W Cain, and Emily J Carbone. An integrated system for cementless hip replacement. *Engineering in Medicine and Biology Magazine, IEEE*, 14(3):307–313, 1995.

[61] Fahd R Khan and Jaimie M Henderson. Deep brain stimulation surgical techniques. *Handb Clin Neurol*, 116:27–37, 2013.

[62] Thomas C Kienzle III, S David Stulberg, Michael Peshkin, Arthur Quaid, Jon Lea, A Goswani, and Chi-hour Wu. Total knee replacement. *Engineering in Medicine and Biology Magazine, IEEE*, 14(3):301–306, 1995.

[63] Duck Whan Kim, Young Soo Lee, Min Soo Park, and Chong Nam Chu. Tool life improvement by peck drilling and thrust force monitoring during deep-micro-hole drilling of steel. *International Journal of Machine Tools and Manufacture*, 49(3):246–255, 2009.

[64] Jan-Philipp Kobler, Jesus Díaz Díaz, J Michael Fitzpatrick, G Jakob Lexow, Omid Majdani, and Tobias Ortmaier. Localization accuracy of sphere fiducials in computed tomography images. In *SPIE Medical Imaging*, pages 90360Z–90360Z. International Society for Optics and Photonics, 2014.

[65] Jan-Philipp Kobler, Jens Kotlarski, Julian Öltjen, Stephan Baron, and Tobias Ortmaier. Design and analysis of a head-mounted parallel kinematic device for skull surgery. *International journal of computer assisted radiology and surgery*, 7(1):137–149, 2012.

[66] Jan-Philipp Kobler, Kathrin Nuelle, G Jakob Lexow, Thomas S Rau, Omid Majdani, Lueder A Kahrs, Jens Kotlarski, and Tobias Ortmaier. Configuration optimization and experimental accuracy evaluation of a bone-attached, parallel robot for skull surgery. *International journal of computer assisted radiology and surgery*, 11(3):421–436, 2015.

[67] Jan-Philipp Kobler, Lenka Prielozny, G Jakob Lexow, Thomas S Rau, Omid Majdani, and Tobias Ortmaier. Mechanical characterization of bone anchors used with a bone-attached, parallel robot for skull surgery. *Medical engineering & physics*, 37(5):460–468, 2015.

[68] Jan-Philipp Kobler, Michael Schoppe, G Jakob Lexow, Thomas S Rau, Omid Majdani, Lüder A Kahrs, and Tobias Ortmaier. Temporal bone borehole accuracy for cochlear implantation influenced by drilling strategy: an in vitro study. *International journal of computer assisted radiology and surgery*, 9(6):1033–1043, 2014.

[69] Jan-Philipp Kobler, Sergej Wall, G Jakob Lexow, Carl Philipp Lang, Omid Majdani, Lüder A Kahrs, and Tobias Ortmaier. An experimental evaluation of loads occurring during guided drilling for cochlear implantation. *International journal of computer assisted radiology and surgery*, 10(10):1625–1637, 2015.

[70] Louis B Kratchman, Grégoire S Blachon, Thomas J Withrow, Ramya Balachandran, Robert F Labadie, and Robert J Webster. Design of a bone-attached

parallel robot for percutaneous cochlear implantation. *Biomedical Engineering, IEEE Transactions on*, 58(10):2904–2910, 2011.

[71] Jona Kronenberg, Wolfgang Baumgartner, Lela Migirov, Tal Dagan, and Minka Hildesheimer. The suprameatal approach: an alternative surgical approach to cochlear implantation. *Otology & Neurotology*, 25(1):41–45, 2004.

[72] Jona Kronenberg, Lela Migirov, and Tal Dagan. Suprameatal approach: new surgical approach for cochlear implantation. *The Journal of Laryngology & Otology*, 115(04):283–285, 2001.

[73] Yik San Kwoh, Joahin Hou, Edmond Jonckheere, Samad Hayati, et al. A robot with improved absolute positioning accuracy for ct guided stereotactic brain surgery. *Biomedical Engineering, IEEE Transactions on*, 35(2):153–160, 1988.

[74] Robert F Labadie, Ramya Balachandran, Jason Mitchell, Jack H Noble, Omid Majdani, David Haynes, Marc Bennett, Benoit M Dawant, and J Michael Fitzpatrick. Clinical validation study of percutaneous cochlear access using patient customized micro-stereotactic frames. *Otology & Neurotology*, 31(1):94, 2010.

[75] Robert F Labadie, Ramya Balachandran, Jack H Noble, Grégoire S Blachon, Jason E Mitchell, Fitsum A Reda, Benoit M Dawant, and J Michael Fitzpatrick. Minimally invasive image-guided cochlear implantation surgery: First report of clinical implementation. *The Laryngoscope*, 124(8):1915–1922, 2014.

[76] Robert F Labadie, Pallavi Chodhury, Ebru Cetinkaya, Ramya Balachandran, David S Haynes, Micahel R Fenlon, Andrzej S Jusczyzck, and J Michael Fitz-

patrick. Minimally invasive, image-guided, facial-recess approach to the middle ear: demonstration of the concept of percutaneous cochlear access in vitro. *Otology & Neurotology*, 26(4):557–562, 2005.

[77] Robert F Labadie, Michael Fenlon, H Cevikalp, S Harris, Robert Galloway, and J Michael Fitzpatrick. Image-guided otologic surgery. In *International Congress Series*, volume 1256, pages 627–632. Elsevier, 2003.

[78] Robert F Labadie, Omid Majdani, and J Michael Fitzpatrick. Image-guided technique in neurotology. *Otolaryngologic Clinics of North America*, 40(3):611–624, 2007.

[79] Robert F Labadie, Jason Mitchell, Ramya Balachandran, and J Michael Fitzpatrick. Customized, rapid-production microstereotactic table for surgical targeting: description of concept and in vitro validation. *International journal of computer assisted radiology and surgery*, 4(3):273–280, 2009.

[80] Robert F Labadie, Jack H Noble, Benoit M Dawant, Ramya Balachandran, Omid Majdani, and J Michael Fitzpatrick. Clinical validation of percutaneous cochlear implant surgery: initial report. *The Laryngoscope*, 118(6):1031–1039, 2008.

[81] Robert F Labadie, Rohan J Shah, Steve S Harris, Ebru Cetinkaya, David S Haynes, Michael R Fenlon, Andrzej S Juscyzk, Robert L Galloway, and J Michael Fitzpatrick. Submillimetric target-registration error using a novel,

non-invasive fiducial system for image-guided otologic surgery. *Computer Aided Surgery*, 9(4):145–153, 2004.

[82] SJ Lee, KF Eman, and SM Wu. An analysis of the drill wandering motion. *Journal of Manufacturing Science and Engineering*, 109(4):297–305, 1987.

[83] Hoon Lim, Jung-Min Han, Jaesung Hong, Byung-Ju Yi, Seung Hwan Lee, Jin Hyeok Jeong, Nozomu Matsumoto, Masamichi Oka, Shizuo Komune, and Makoto Hashizume. Image-guided robotic mastoidectomy using human-robot collaboration control. In *Mechatronics and Automation (ICMA), 2011 International Conference on*, pages 549–554. IEEE, 2011.

[84] Yi-Chu Lin, Gianlorenzo Dionigi, Gregory W Randolph, I Lu, Pi-Ying Chang, Shan-Yin Tsai, Hoon Yub Kim, Hye Yoon Lee, Ralph P Tufano, Hui Sun, et al. Electrophysiologic monitoring correlates of recurrent laryngeal nerve heat thermal injury in a porcine model. *The Laryngoscope*, 2015.

[85] Xiaofeng Liu, Hakan Cevikalp, and J Michael Fitzpatrick. Marker orientation in fiducial registration. In *Medical Imaging 2003*, pages 1176–1185. International Society for Optics and Photonics, 2003.

[86] Frederik Maes, Andre Collignon, Dirk Vandermeulen, Guy Marchal, and Paul Suetens. Multimodality image registration by maximization of mutual information. *Medical Imaging, IEEE Transactions on*, 16(2):187–198, 1997.

[87] Omid Majdani, Thomas S Rau, Stephan Baron, Hubertus Eilers, Claas Baier, Bodo Heimann, Tobias Ortmaier, Sönke Bartling, Thomas Lenarz, and Martin

Leinung. A robot-guided minimally invasive approach for cochlear implant surgery: preliminary results of a temporal bone study. *International journal of computer assisted radiology and surgery*, 4(5):475–486, 2009.

[88] Omid Majdani, Daniel Schurzig, Andreas Hussong, Thomas Rau, Justin Wittkopf, Thomas Lenarz, and Robert F Labadie. Force measurement of insertion of cochlear implant electrode arrays in vitro: comparison of surgeon to automated insertion tool. *Acta oto-laryngologica*, 130(1):31–36, 2010.

[89] Colin D Mathers and Dejan Loncar. Projections of global mortality and burden of disease from 2002 to 2030. *Plos med*, 3(11):e442, 2006.

[90] Constantinos Mavroidis, Steven Dubowsky, Ph Drouet, J Hintersteiner, and J Flanz. A systematic error analysis of robotic manipulators: application to a high performance medical robot. In *Robotics and Automation, 1997. Proceedings., 1997 IEEE International Conference on*, volume 2, pages 980–985. IEEE, 1997.

[91] Kepra L McBrayer, George B Wanna, Benoit M Dawant, Ramya Balachandran, Robert F Labadie, and Jack H Noble. Resection planning for robotic acoustic neuroma surgery. In *SPIE Medical Imaging*, pages 978608–978608. International Society for Optics and Photonics, 2016.

[92] Marco A Meggiolaro, Steven Dubowsky, and Constantinos Mavroidis. Geometric and elastic error calibration of a high accuracy patient positioning system. *Mechanism and Machine Theory*, 40(4):415–427, 2005.

[93] Jack H Noble, Benoit M Dawant, Frank M Warren, and Robert F Labadie. Automatic identification and 3-d rendering of temporal bone anatomy. *Otology & Neurotology*, 30(4):436, 2009.

[94] Jack H Noble, Omid Majdani, Robert F Labadie, Benoit Dawant, and J Michael Fitzpatrick. Automatic determination of optimal linear drilling trajectories for cochlear access accounting for drill-positioning error. *The International Journal of Medical Robotics and Computer Assisted Surgery*, 6(3):281–290, 2010.

[95] Jack H Noble, Frank M Warren, Robert F Labadie, and Benoit M Dawant. Automatic segmentation of the facial nerve and chorda tympani in ct images using spatially dependent feature values. *Medical physics*, 35(12):5375–5384, 2008.

[96] Kevin C Olds, Preetham Chalasani, Paulette Pacheco-Lopez, Iulian Iordachita, Lee M Akst, and Russell H Taylor. Preliminary evaluation of a new microsurgical robotic system for head and neck surgery. In *Intelligent Robots and Systems (IROS 2014), 2014 IEEE/RSJ International Conference on*, pages 1276–1281. IEEE, 2014.

[97] National Institute on Deafness and Other Communication Disorders. Cochlear implants. nih publication no. 00-4798. `https://www.nidcd.nih.gov/health/cochlear-implants`, February 2016 (Accessed: 20 August 2016).

[98] Rupesh Kumar Pandey and SS Panda. Drilling of bone: A comprehensive review. *Journal of clinical Orthopaedics and Trauma*, 4(1):15–30, 2013.

[99] Howard A Paul, William L Bargar, Brent Mittlestadt, Bela Musits, Russell H Taylor, Peter Kazanzides, Joel Zuhars, Bill Williamson, and William Hanson. Development of a surgical robot for cementless total hip arthroplasty. *Clinical Orthopaedics and related research*, 285:57–66, 1992.

[100] Jason Pile, Mei Yi Cheung, Jian Zhang, and Nabil Simaan. Algorithms and design considerations for robot assisted insertion of perimodiolar electrode arrays. In *Robotics and Automation (ICRA), 2011 IEEE International Conference on*, pages 2898–2904. IEEE, 2011.

[101] Jason Pile and Nabil Simaan. Characterization of friction and speed effects and methods for detection of cochlear implant electrode tip fold-over. In *Robotics and Automation (ICRA), 2013 IEEE International Conference on*, pages 4409–4414. IEEE, 2013.

[102] Jason Pile and Nabil Simaan. Modeling, design, and evaluation of a parallel robot for cochlear implant surgery. *IEEE/ASME Transactions on Mechatronics*, 19(6):1746–1755, 2014.

[103] C Plaskos, P Cinquin, S Lavallée, and AJ Hodgson. Praxiteles: a miniature bone-mounted robot for minimal access total knee arthroplasty. *The International Journal of Medical Robotics and Computer Assisted Surgery*, 1(4):67–79, 2005.

[104] Christopher Plaskos, Antony J Hodgson, and Philippe Cinquin. Modelling and optimization of bone-cutting forces in orthopaedic surgery. In *Medical Image*

Computing and Computer-Assisted Intervention-MICCAI 2003, pages 254–261. Springer, 2003.

[105] Pooyan Rohani, Jason Pile, Lueder Kahrs, Ramya Balachandran, Gregoire Blachon, Nabil Simaan, and Robert F Labadie. Forces and trauma associated with minimally-invasive, image-guided cochlear implantation. *Otolaryngology–Head and Neck Surgery*, 149(2 suppl):P99–P100, 2013.

[106] Stephen A Sapareto and William C Dewey. Thermal dose determination in cancer therapy. *International Journal of Radiation Oncology* Biology* Physics*, 10(6):787–800, 1984.

[107] Daniel Schurzig, Robert F Labadie, Andreas Hussong, Thomas S Rau, and Robert J Webster III. Design of a tool integrating force sensing with automated insertion in cochlear implantation. *IEEE/ASME Transactions on mechatronics*, 17(2):381–389, 2012.

[108] Daniel Schurzig, Robert J Webster III, Mary S Dietrich, and Robert F Labadie. Force of cochlear implant electrode insertion performed by a robotic insertion tool: comparison of traditional versus advance off-stylet techniques. *Otology & Neurotology*, 31(8):1207, 2010.

[109] Moshe Shoham, Michael Burman, Eli Zehavi, Leo Joskowicz, Eduard Batkilin, and Yigal Kunicher. Bone-mounted miniature robot for surgical procedures: concept and clinical applications. *Robotics and Automation, IEEE Transactions on*, 19(5):893–901, 2003.

[110] Michael A Siebold, Neal P Dillon, Loris Fichera, Robert F Labadie, Robert J Webster, and J Michael Fitzpatrick. Safety margins in robotic bone milling: from registration uncertainty to statistically safe surgeries. *The International Journal of Medical Robotics and Computer Assisted Surgery*, 2016.

[111] Michael A Siebold, Neal P Dillon, Robert J Webster, and J Michael Fitzpatrick. Incorporating target registration error into robotic bone milling. In *SPIE Medical Imaging*, pages 94150R–94150R. International Society for Optics and Photonics, 2015.

[112] Milan Sonka and J Michael Fitzpatrick. Handbook of medical imaging, vol. 2: Medical image processing and analysis. *SPIE-International Society for Optical Engine*, 2000.

[113] Milan Sonka, J Michael Fitzpatrick, and Barry R Masters. Handbook of medical imaging, volume 2: Medical image processing and analysis. *Optics & Photonics News*, 13:50–51, 2002.

[114] Milan Sonka, Vaclav Hlavac, and Roger Boyle. *Image processing, analysis, and machine vision.* Cengage Learning, 2014.

[115] Sven-Eric Stangerup, Mirko Tos, Jens Thomsen, and Per Caye-Thomasen. True incidence of vestibular schwannoma? *Neurosurgery*, 67(5):1335–1340, 2010.

[116] Naohiko Sugita, Taiga Nakano, Yoshikazu Nakajima, Kazuo Fujiwara, Nobuhiro Abe, Toshifumi Ozaki, Masahiko Suzuki, and Mamoru Mitsuishi. Dynamic

controlled milling process for bone machining. *Journal of Materials Processing Technology*, 209(17):5777–5784, 2009.

[117] Jan Taler and Piotr Duda. *Solving direct and inverse heat conduction problems.* Springer Science & Business Media, 2010.

[118] Russell H Taylor, Brent D Mittelstadt, Howard A Paul, William Hanson, Peter Kazanzides, Joel F Zuhars, Bill Williamson, Bela L Musits, Edward Glassman, and William L Bargar. An image-directed robotic system for precise orthopaedic surgery. *Robotics and Automation, IEEE Transactions on*, 10(3):261–275, 1994.

[119] Russell H Taylor and Dan Stoianovici. Medical robotics in computer-integrated surgery. *Robotics and Automation, IEEE Transactions on*, 19(5):765–781, 2003.

[120] Engineering Toolbox. Air properties. `http://www.engineeringtoolbox.com/air-properties-d_156.html`, (Accessed: 21 September 2016).

[121] Tobias Topp, Thorben Müller, Sebastian Huss, Peter Herbert Kann, Eberhard Weihe, Steffen Ruchholtz, and Ralph Peter Zettl. Embalmed and fresh frozen human bones in orthopedic cadaveric studies: which bone is authentic and feasible? a mechanical study. *Acta orthopaedica*, 83(5):543–547, 2012.

[122] Lung-Wen Tsai. *Robot analysis: the mechanics of serial and parallel manipulators.* John Wiley & Sons, 1999.

[123] Emil H van Haaren, Babette C van der Zwaard, Albert J van der Veen, Ide C Heyligers, Paul IJM Wuisman, and Theo H Smit. Effect of long-term preserva-

tion on the mechanical properties of cortical bone in goats. *Acta orthopaedica*, 79(5):708–716, 2008.

[124] William K Veitschegger and Chi-Haur Wu. Robot accuracy analysis based on kinematics. *Robotics and Automation, IEEE Journal of*, 2(3):171–179, 1986.

[125] Tianmiao Wang, Sheng Luan, Lei Hu, Zhongjun Liu, Weishi Li, and Liang Jiang. Force-based control of a compact spinal milling robot. *The International Journal of Medical Robotics and Computer Assisted Surgery*, 6(2):178–185, 2010.

[126] Frank M Warren, Ramya Balachandran, J Michael Fitzpatrick, and Robert F Labadie. Percutaneous cochlear access using bone-mounted, customized drill guides: demonstration of concept in vitro. *Otology & Neurotology*, 28(3):325–329, 2007.

[127] Tom M Williamson, Brett J Bell, Nicolas Gerber, Lilibeth Salas, Philippe Zysset, Marco Caversaccio, and Simon Weber. Estimation of tool pose based on force–density correlation during robotic drilling. *Biomedical Engineering, IEEE Transactions on*, 60(4):969–976, 2013.

[128] Alon Wolf, Branislav Jaramaz, B Lisien, and AM DiGioia. Mbars: mini bone-attached robotic system for joint arthroplasty. *The International Journal of Medical Robotics and Computer Assisted Surgery*, 1(2):101–121, 2005.

[129] Tian Xia, Clint Baird, George Jallo, Kathryn Hayes, Nobuyuki Nakajima, Nobuhiko Hata, and Peter Kazanzides. An integrated system for planning, nav-

igation and robotic assistance for skull base surgery. *The International Journal of Medical Robotics and Computer Assisted Surgery*, 4(4):321–330, 2008.

[130] Pavel S Yarmolenko, Eui Jung Moon, Chelsea Landon, Ashley Manzoor, Daryl W Hochman, Benjamin L Viglianti, and Mark W Dewhirst. Thresholds for thermal damage to normal tissues: an update. *International Journal of Hyperthermia*, 27(4):320–343, 2011.

[131] Stefan Zech, Thomas Goesling, Stefan Hankemeier, Karsten Knobloch, Jens Geerling, Kristof Schultz-Brunn, Christian Krettek, and Martinus Richter. Differences in the mechanical properties of calcaneal artificial specimens, fresh frozen specimens, and embalmed specimens in experimental testing. *Foot & ankle international*, 27(12):1126–1136, 2006.

Appendices

Appendix A

Robot Joint Compliance Testing

As described in Chapter 4.3.4, the compliance matrix of the robot was determined by experimentally evaluating the stiffness/compliance of each joint in both the direction of joint motion and the off-axis directions. The stiffness of the rotational joint was determined from the harmonic gearbox manufacturer's specifications. The stiffness of the linear joints were determined through experimental measurement. The stiffness values were then used in Equation 4.17, which applied the method of "virtual joints" described by Abele et al. [2] to calculate a more accurate compliance matrix for the robot. This appendix describes the method of determining the individual stiffness values and provides the experimental results for linear joints with various bearing combinations.

A.1 Experimental Methods

The stiffness of the linear ball bearings used in the prismatic joints of the robot were tested by applying force and moments in three orthogonal directions (see Figure A.1). Moments were applied by placing known weights at known distances from the bearing locations. The corresponding linear deflection at the end of the moment arm was measured using a dial indicator and converted to an angular deflection. This process was repeated for several applied moments and the torsional stiffness value

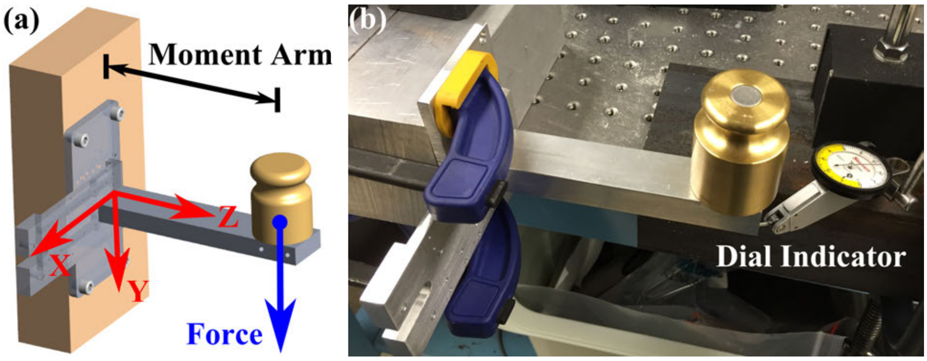

Figure A.1: (a) Rendering of stiffness measurement setup showing coordinate frame of the linear joint and applied load. A similar setup was used for each axis direction. (b) Photo from experimental stiffness testing.

was determined by fitting a line to the experimental data. The linear stiffness values were determined through a similar set of measurements and data analysis

Several bearing sizes and configurations (number of bearings and distance between the two parallel rails) were tested. The bearing carriage and rail sizes ranged from 5 mm to 7 mm. Figure A.2 shows the various combinations of bearings tested in this analysis.

A.2 Results

An example plot of the applied moment versus angular displacement is shown in Figure A.3. Table A.1 shows the calculated torsional stiffness values in each direction for each of the bearing configurations. The bearing configuration of double 5 mm carriages with 24 mm rail separation was used for the robot. The linear stiffness was determined to be 3.23 kN/mm in along the axis of joint motion (X-axis in Figure A.1) and was negligible in the other two directions.

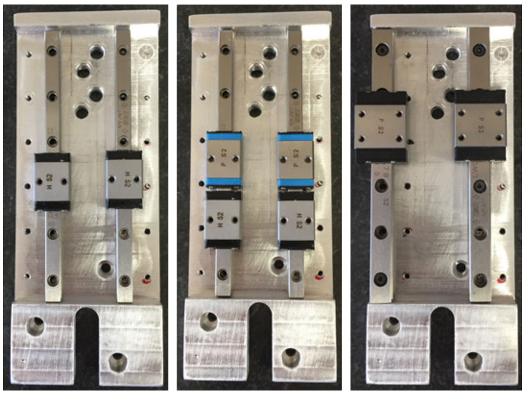

Figure A.2: Carriage and rail combinations tested. (Left) Single set of 5 mm carriages with 24 mm rail separation. (Center) Double set of 5 mm carriages with 24 mm rail separation. (Right) Single set of 7 mm carriages with 32 mm rail separation.

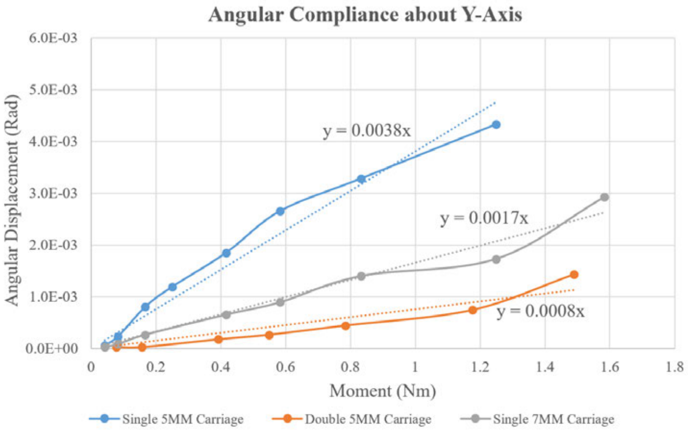

Figure A.3: Example plot of angular displacement versus applied moment. This plot shows the data for a moment applied about the Y-axis.

Table A.1: Experimentally evaluated angular compliances for various bearing configurations.

	Stiffness Values (Nm/rad)		
Direction	Single 5 mm Carriages	Double 5 mm Carriages	Single 7 mm Carriages
X	2000	2000	2500
Y	263	1250	588
Z[a]	384	1429	-

[a] 7 mm carriages not tested in Z-direction.

Appendix B

Analysis of Prior Minimally Invasive Cochlear Implantation Patient Data

Given that one of the nine patients in the initial clinical implementation of minimally invasive CI experienced heat-related facial nerve damage, we hypothesized that this patient may have been predisposed to risk of such damage. To evaluate this hypothesis, the image data from the nine patients in the prior clinical trial was analyzed according to the pre-operative screening protocol developed in Chapter 7.2.1.

B.1 Thermal Modeling Using CT Data

The two risk metrics described in Section 7.2.1 were calculated for each patient using their pre-operative CT scan. Additionally, the patient-specific, CT image-based thermal model proposed by Feldmann et al. [44] was used in the analysis. This model assumes that the drill is a moving point heat source passing through a homogeneous, semi-infinite solid material. Detailed derivation of the moving point heat source model can be found in [117]. Using this approach, the temperature at any position (x, y, z) and time (t) is calculated by numerically integrating the following equation:

$$T(x,y,z,t) = T_0 + \int_0^{\tau} \frac{\dot{Q}(t)}{c_p\rho[4\pi\alpha(t-\tau)]^{3/2}} \exp\left(\frac{r(x,y,z,\tau)^2}{4\alpha(t-\tau)}\right) d\tau \tag{B.1}$$

where T_0 is the initial temperature of the bone (body temperature, 37°C), c_p is the specific heat of bone, ρ is the density of bone, and α is the thermal diffusivity of bone ($\alpha = k_{thermal}/\rho c_p$, where $k_{thermal}$ is the thermal conductivity). r is the time-dependent distance between the moving heat source and the point at which the temperature is being calculated. Finally, $\dot{Q}$ is the heat generation rate, which is varied based on the bone intensity and drilling parameters according to:

$$\dot{Q} = vAD(t)^b \tag{B.2}$$

where v is the linear velocity of the drill (heat source), $D(t)$ is the bone intensity at a given time, and A and b are calibration coefficients. The calibration coefficients are system-specific and reflect a particular CT scanner and set of drilling parameters (e.g. linear velocity, rotational speed, drill bit design, etc.). Since we do not have temperature measurements or data related to the drill trajectories used in the prior clinical cases, it is not possible to calibrate the model for those cases. However, we can test the model with many different sets of calibration coefficients and drilling trajectories to provide a relative comparison of temperature rise based on the bone composition of each individual patient.

The pre-operative clinical CT scans used in this analysis were acquired by several conventional CT scanners (Philips iCT 128, Philips Brilliance 64, and General Electric BrightSpeed). To compensate for the difference between the mapping between tissue density and image intensity (Hounsfield Units or HU) for the three scanners, the scans were normalized. This was done by comparing the intensity values of the labyrinth bone (a hard solid region of bone containing the semicircular canals) across

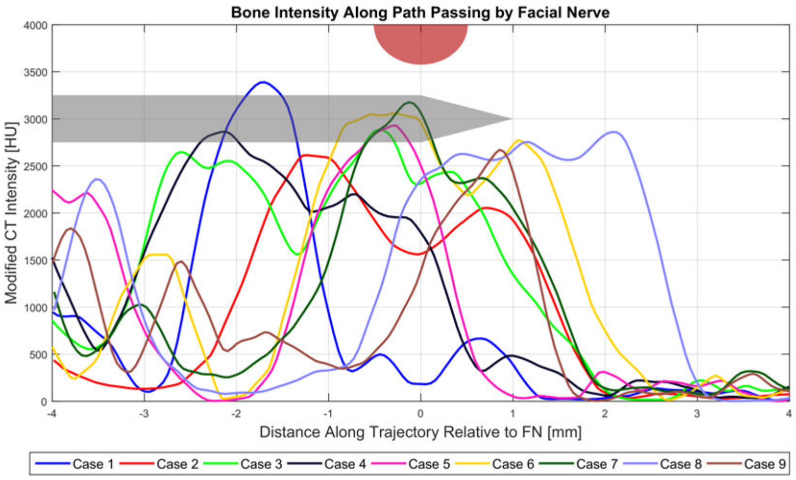

Figure B.1: Normalized image intensity along the planned drill trajectory of the pre-operative CT scan for the nine clinical cases of minimally invasive CI surgery. Intensity is shown for the region near the facial nerve (±4 mm from the point where the drill passes closest to the nerve). A schematic of the facial nerve and drill are shown to provide context regarding the direction of the drill path and position of the nerve. Case 8 represents the patient who experienced facial nerve paralysis.

different scans. Since all cases also involved an intra-operative CT scan with either a Xoran xCAT ENT or a Philips Allura, the inter-scanner variability in bone density (also accounting for inter-patient variability) could be determined by segmenting the labyrinth in each scan and comparing the intensity histograms. The pre-operative CT images were then normalized to adjust for the different intensity ranges of the scanners (the maximum adjustment to the intensity was 7%) and shifted so that air corresponds to a value of 0. The normalized intensity for each clinical case is shown in Figure B.1.

Pre-operative segmentations of the facial nerve were also used in the analysis to determine the point at which to analyze the temperature. The closest point on the facial nerve to the planned drill path was selected as the measurement point (x, y, z) in the thermal model.

B.2 Simulation Results and Discussion

B.2.1 Pre-Operative Risk Assessment Metrics

Table B.1 lists the pre-operative risk assessment metrics for the nine prior cases of minimally invasive CI surgery. *Case 3* and *Case 6* have the highest bone density integral values as well as the highest bone conductance values. These are likely the only cases that may have been excluded in the initial clinical trial using the revised approach. *Case 8*, the patient who had thermal nerve would have been considered low risk according to these metrics; however, it is again important to consider the fact that the drilling approach was neither optimized nor carried out in a consistent manner in these cases so pre-operative risk does not necessarily correlated with actual temperature rise.

B.2.2 Moving Point Heat Source Model

Ten simulations using the moving point source model for each patient were performed. The patient who experienced facial nerve paralysis is *Case 8* in all tables and plots. Table B.2 provides a list of the model coefficients and drilling trajectory parameters used in the simulations. The image-based heat generation rate and associated temperature response for one set of calibration coefficients and drilling trajectory for each

Table B.1: Pre-operative risk metrics for prior clinical data.

	Pre-Op Risk Metrics (Pct. Rank)[a]	
Case No.	**Path Intensity Integral**	**Thermal Conductance**
1	69.2%	96.2%
2	65.4%	53.8%
3	34.6%	23.1%
4	48.1%	30.8%
5	82.7%	38.5%
6	44.2%	11.5%
7	69.2%	73.1%
8	69.2%	61.5%
9	88.5%	46.2%

[a] See Section 7.2.1 for a description of each metric. Risk percentiles based on the scans of the four bones included in the experiments presented in Chapter 7 and the nine patients scans from the prior clinical trial [75] (lower percentile indicates higher risk).

patient is shown in Figure B.2.

Table B.3 shows the relative peak temperatures for each of the ten temperature response simulations for each patient. As described above, actual temperatures are unknown since the calibration coefficients are unknown but relative peak temperatures in simulation can be compared for each set of coefficients. The results are fairly consistent across calibration coefficient sets. *Case 6* had the highest peak temperature in all trials, followed by *Case 3* and *Case 7*. *Case 8*, the patient who had thermal nerve only had a relative temperature rise of 42-48% of the *Case 6* temperature rise. Furthermore, *Case 8* ranked 69.2% and 61.5% in terms of the pre-operative risk metrics, indicating that this patient's bone composition did not yield an especially high rate of heat generation or an especially conductive path between the drill and the nerve.

Table B.2: Parameters used in moving point heat source simulation using prior clinical data.

	Calibration Coeff.[a]		
Simulation	**A**	**b**	**Drilling Vel. (mm/s)**
1	2.0×10^{-4}	2.0	0.25
2	2.0×10^{-4}	2.0	0.50
3	2.0×10^{-4}	2.0	1.00
4	2.0×10^{-4}	2.0	2.00
5	2.0×10^{-4}	1.8	1.00
6	2.0×10^{-4}	2.2	1.00
7	2.0×10^{-5}	2.4	1.00
8	5.0×10^{-4}	1.8	1.00
9	1.0×10^{-3}	1.6	1.00
10	1.0×10^{-2}	1.5	1.00

[a] From Equation B.2. Values selected using the data from [44] as a baseline and were adjusted to span a range of possible calibrations.

Table B.3: Moving point heat source simulation results: comparison of relative peak temperatures.

	Case Number								
Simulation	**1**	**2**	**3**	**4**	**5**	**6**	**7**	**8**	**9**
1	0.34	0.44	0.85	0.63	0.72	1.00	0.81	0.48	0.36
2	0.27	0.47	0.86	0.61	0.66	1.00	0.79	0.47	0.33
3	0.23	0.46	0.80	0.53	0.56	1.00	0.76	0.44	0.30
4	0.20	0.44	0.73	0.46	0.50	1.00	0.73	0.43	0.27
5	0.24	0.49	0.81	0.56	0.57	1.00	0.77	0.45	0.32
6	0.23	0.43	0.78	0.50	0.55	1.00	0.75	0.43	0.28
7	0.22	0.41	0.76	0.47	0.54	1.00	0.75	0.42	0.26
8	0.24	0.49	0.82	0.56	0.57	1.00	0.77	0.45	0.32
9	0.25	0.52	0.83	0.59	0.58	1.00	0.77	0.46	0.34
10	0.25	0.53	0.84	0.60	0.58	1.00	0.78	0.47	0.35

[a] Value given is the peak temperature for each patient divided by the highest peak temperature (of all patients) for that set of simulation parameters.

[b] Values are highlighted based on relative temperature to easily compare results.

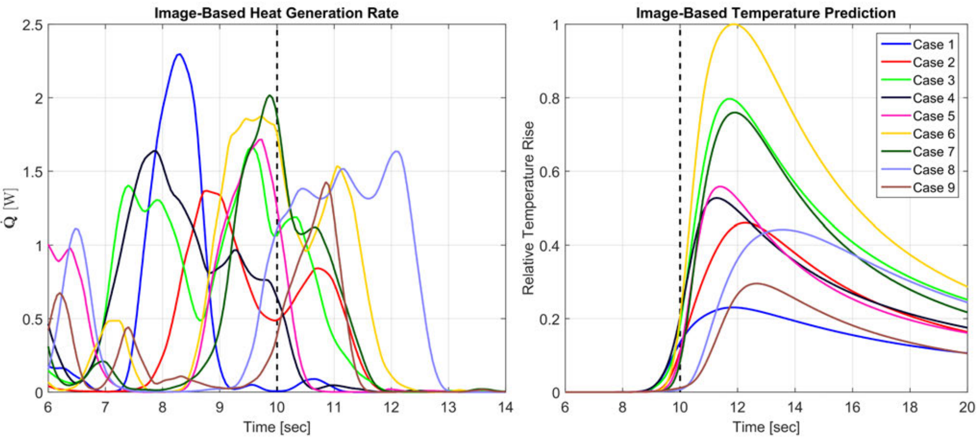

Figure B.2: Sample set of simulation results for calibration coefficients of $A = 2.0 \times 10^{-4}$ and $b = 2.0$ and a linear velocity of 1.0 mm/s. (Left) CT-based heat generation rates for each of the CT scans from the prior clinical cases of minimally invasive CI. (Right) Temperature response associated with each heat generation rate. Note that the magnitude of the simulated temperature response is dependent on selection of the calibration coefficients so these simulations only provide a *relative* comparison between patients.

The results indicate that the patient who experienced temporary facial paralysis during the initial clinical implementation of minimally invasive CI [75] was not predisposed to higher risk of thermal injury compared to the other eight patients. Since the drilling was not standardized across these initial cases, it is likely that the drilling for this particular patient was performed in a way that resulted in higher rates of heat generation, independent of the bone composition. This may have been caused by the kinematics of the drill advancement or the amount of irrigation that reached the drill tip while it was in close proximity to the facial nerve. Thus, the lack of a consistent drilling protocol was likely the reason for inconsistent patient outcomes rather than the differences in patient anatomy. This further strengthens the motivation for developing a standardized drilling protocol, which is the focus of Chapter 7.